Radiation and Polarization Diversities of Compact Archimedean Spiral Antennas

By

Ali Momen Mehrabani

A Thesis submitted to the Faculty of Graduate Studies of

The University of Manitoba

in partial fulfilment of the requirements of the degree of

DOCTOR OF PHILOSOPHY

Department of Electrical and Computer Engineering
University of Manitoba
Winnipeg, Manitoba, Canada

Abstract

In this thesis, four-arm Archimedean spiral antennas are investigated, which are low profile and have compact structure. The operating frequency bands can be designed for any microwave and millimeter frequency ranges and the antenna may be utilized in any desired applications such as Global Positioning Systems, radars, navigation systems, modern satellite communications, adaptive nulling, beam shaping, and direction finding. The concept of cavity backed absorber-filled structure along with a small ground plane embedded inside, as an inexpensive and wideband balun, is employed to reduce the axial size of the antenna. The antenna can generate broadside and boresight-null radiation patterns at the dominant and higher order modes, respectively. The study demonstrates that the proposed compact structure successfully supports the excitation of higher order modes.

Polarization diversity of spiral antennas is mathematically described for an N-arm spiral antenna along with the required feeding networks. Realization of circularly-polarized broadside radiation patterns, with both senses of polarization, is then elaborated for a center-fed low-profile four-arm Archimedean spiral antenna. The radiation active zones, for generating both right- and left-handed circular polarization waves, are determined and the antenna performance in a frequency band, shared by both senses of polarization, is investigated.

The developed antennas can be utilized in frequency reuse applications to enhance the wireless channel capacity and as primary feeds in high gain reflector antennas. Their performance in small front-fed parabolic reflector antennas is

numerically investigated. It is shown that excellent circular polarization performance, with a remarkable radiation pattern symmetry and axial ratios below 0.5dB, low cross polarization components, and reflector total efficiencies, as high as 77.8% can be attained. Moreover, backward radiation properties of center-fed four-arm Archimedean spiral antennas are also explored, and their possible applications in reflector antennas are presented.

Finally, the proposed dual-polarized spiral antennas are further investigated by dielectric loading, for size reduction purposes and frequency tuning applications. Both full and partial dielectric loadings are considered and investigated for the spiral antenna performance. A grooved dielectric substrate is also utilized to enable generating low-contrast dielectric permittivities. The spiral antenna performance, etched on such a grooved substrate, is similarly investigated.

Acknowledgements

Table of Contents

List of Tables

List of Figures

Chapter 1

Introduction

1.1 Preface

Spiral antennas have been used in a variety of applications such as direction finding, radars, navigation systems, and satellite communications [1]. Inherently, they are wide band antennas, and generate circularly polarized (CP) radiation. They can take different shapes. The most popular forms of the spiral antennas are equiangular and Archimedean shaped spirals [2]. Due to the superior circularly polarized performance of Archimedean spiral antennas [3], [4], this type of antennas are investigated in this thesis. They are normally wound over a dielectric support to help maintain their shape. This supporting material can have any shape, but the most popular ones are the conical and planar shapes, although spherical shapes are also used, especially for miniaturized spiral antennas. The planar spirals are low profiles, and result in compact antennas. However, the cone geometry, being a more general shape, provides a more flexible antenna configuration, where the cone angle can be used to shape the antenna radiation patterns [2]. But, it results in a three-dimensional antenna structure, which is not compact any more. This thesis is concerned with low profile circularly polarized antennas, and thus the planar spiral geometry is selected for the study. In particular, low profile planar spirals with diverse polarization and radiation properties are thoroughly studied.

Generally, planar spiral antennas, without a reflecting ground plane, radiate into both upper- and lower-half spaces. However, antennas with unidirectional patterns are required in most applications. To this end, the spiral antenna is normally placed above a reflecting surface, such as a conducting ground plane, to direct the radiation towards the upper-half space only. This solution, however, leads to an enlarged antenna structure, with ground plane sizes larger than spiral arms, to maintain a good CP performance. Moreover, very close proximity of the ground plane to the spiral arms, due to the image effect, normally causes undesired interactions between the antenna and the ground plane, which limits the antenna frequency bandwidth. However, with ever-increasing demand for portable and small handheld devices, wireless communication systems require more compact antenna structures, which are integrated with radio frequency and microwave devices. Therefore, a compact spiral antenna has the most desirable configuration and a great market demand, as it significantly reduces the device size, cost, volume, feed blockage, and mutual interferences between the antenna and the connected electronic circuits and other close by wireless devices.

The present work investigates radiation and polarization properties of compact planar four-arm Archimedean spiral antennas. First, radiation characteristics of these antennas are fully addressed at both fundamental and higher order modes; particularly in low profile structures, partially-filled with microwave absorbers, and with an inexpensive embedded wideband balun, to generate balanced spiral modes. The low-profile multimode spiral antenna is investigated over frequency bands of the Global Positioning Systems (GPS). Then, the polarization diversity of N-arm spiral antennas is mathematically described and extended to low-profile four-arm Archimedean spiral

2

antennas that are capable of simultaneously generating both senses of circular polarization. These dual-polarized antennas are extremely attractive in frequency reuse wireless applications, where two orthogonal signals share the same frequency range; thereby increasing the channel capacity of the wireless link. They are also of special interest in high gain reflector antenna applications as an illuminating source, also known as the primary feed. Thus, their performance in symmetric parabolic reflector antennas is studied. In addition, unique backward radiation properties of compact four-arm Archimedean spiral antennas, and their applications in small front-fed parabolic reflector antennas, are explored and investigated in this thesis. They can considerably relax the mechanical constraints on the feed assembly that simplify the feed support structure, minimize the reflector aperture blockage, and improve its aperture efficiency. Finally, the performance of the proposed dual-polarized spiral antennas, loaded with full, partial, and grooved dielectric substrates, is studied, and the possibility of frequency tuning and size reduction are investigated.

1.2 Structure of the Thesis

This thesis consists of seven chapters. Chapter one covers a brief introduction on the topic and describes its overall goals in implementing compact and low-profile spiral antennas with multimode, dual-polarized, and rear radiation capabilities, as well as their applications in symmetric reflector antennas. Chapter two provides a literature review and background theory on spiral antennas, conventional capacitive and inductive loading techniques used for compact antennas, polarization diversity, and backward radiation properties of Archimedean spiral antennas. Recent works on compact and low profile

spiral antennas are also reviewed in chapter two. Moreover, the proposed study is outlined in this chapter. The measurement results for the electrical properties of the proposed low profile four-arm Archimedean spiral antenna are addressed in chapter three, for both first and second order modes, which can be easily extended to multi-arm spiral antennas. Chapter four presents the polarization diversity properties of low-profile spiral antennas, generating both senses of circular polarization over a respectable frequency band. The dual-polarized radiation zones are determined and their dependency on the ground plane size is addressed. Prototype antennas are fabricated and tested in the University of Manitoba's Antenna Laboratory, resulting in a successful validation of the proposed concept in practice, with excellent agreement between the measured and computed results. Applications of the proposed dual-polarized four-arm Archimedean spiral antennas as primary feeds in symmetric front-fed paraboloids are studied in chapter five. Backward radiation characteristics of single-polarized four-arm Archimedean spiral antennas are also explored and their performances in small parabolic reflectors are presented in chapter five. The dielectric loading technique is applied to the proposed dual-polarized four-arm Archimedean spiral antenna in chapter six, to address the antenna size reduction and frequency tuning capabilities. The results for electrical properties of the antennas, loaded with full, partial, and grooved substrates are presented. Finally, the discussion of the results and conclusions reached are covered in chapter seven. Potential topics for future studies are also provided in this chapter.

1.3 Contributions

A summary of my accomplishments in this thesis is listed below.

- Radiation properties of dual-mode four-arm Archimedean spiral antennas are investigated at the first and second order modes. A compact antenna structure partially filled with microwave absorber, along with a small conducting disk as a balun, is studied to produce unidirectional radiation patterns. The developed low-profile antenna generates both broadside and conical radiation patterns. The measured and numerical results are in good agreement.

- Dielectric properties of undulated transmission lines are extracted from the scattering parameters of their corresponding two-port networks. It is shown that the effective dielectric constant of the line can be significantly increased, at least by a factor of 6; even when the supporting material is air. This becomes particularly beneficial in antenna miniaturization, without using high-contrast dielectric substrates. Other than size reduction, this also eliminates the associated dielectric loss.

- Unidirectional four-arm Archimedean spiral antennas are proposed for polarization diversity applications, when the spiral arms are center fed. In particular, the radiation mechanism to generate broadside radiation patterns with both senses of circular polarization is fully explained. The required feeding excitation networks are mathematically described for a general case of N-arm spiral antenna. The condition to generate circular polarization diversity is then addressed and applied to four-arm Archimedean spiral antennas, whose circumference is less than three wavelengths. Low-profile antennas backed by conducting ground plane are designed and extensively investigated to study different antenna parameters such as gain, cross polarization, pattern symmetry,

and axial ratio. Proposed antennas with two ground plane sizes are studied. It is shown that both senses of circular polarization are produced, sharing a respectable frequency bandwidth, controlled by the supporting ground plane sizes. The required radiation zones, including the effect of the ground plane size, are approximately formulated. The CP gains of the antenna are also expressed in terms of its half-power beamwidths.

- The performance of the proposed dual-polarized spiral antenna as an illuminating source in parabolic reflector antennas is investigated. Efficiencies as high as 77.8% are achieved with excellent cross-polarization discriminations.

- Unique backward radiation properties of a compact and center-fed four-arm Archimedean spiral antenna are explored and its applications in symmetric front-fed parabolic reflector antennas are studied. It is shown that the spiral antenna generates broadside CP backward radiation patterns with an opposite sense of polarization to the spiral winding direction.

- The proposed dual-polarized spiral antennas, loaded with dielectric materials, are studied for both frequency-tuning applications and realizing compact structures. Both fully and partially loaded structures are investigated. Moreover, to realize a specific dielectric constant, antennas loaded with grooved substrates are numerically studied.

Chapter 2

Literature Review and Background Theory

2.1   Introduction

Spiral antennas are in the class of broadband antennas. They generate circularly polarized radiation patterns, which make them excellent candidates for most modern applications such as radars, direction finding, navigation systems, electronic countermeasures, mobile and satellite communications [1]. The concept of spiral antennas was first introduced by Edwin Turner in the mid-1950s [2]. Later, Turner's results provided an insight into the development of mathematical analysis for the frequency independent antennas by Victor Rumsey in 1957 [5]. In principle, spiral antennas can have any volumetric shape. However, the most popular shapes are the conical and planar spiral antennas, although spherical spiral antennas have also been used to enable the size miniaturization. This thesis is concerned with low profile spiral antennas, and thus the planar spiral antennas are subject of the investigation.

A free-standing planar spiral antenna has a bidirectional radiation pattern. However, in most applications a unidirectional radiation is required. This can be accomplished by using a ground plane, such as a planar metal sheet, to efficiently suppress the radiation directed in the unwanted half-space region, and make the planar spiral antenna a unidirectional antenna. However, this simple approach imposes some limitations on the antenna frequency bandwidth, due to the fixed distance between the antenna and the ground plane, which becomes a variable electrical length, as the frequency of operation

7

changes. For example, to constructively add the far-field radiations from the antenna and its image in the boresight direction, i.e. $\theta=0^o$, the above distance should be at least a quarter wavelength long, which happens in a limited frequency band. Furthermore, by moving the ground plane close to the antenna, the electromagnetic interaction between them becomes stronger. This may, in turn, result in considerable degradation in the antenna radiation pattern and axial ratio performances [6].

It should be noted here that the wide frequency bandwidth of a spiral antenna is due to the angular dependence of its geometry, which for an infinite number of turns become infinite. Such a configuration has no finite electrical length, and its operation becomes frequency independent. Thus, this class of antennas is generally known as the *"frequency independent antennas"*. However, placing a planar spiral over a ground plane introduces a variable, i.e. the distance of the spiral from the ground plane, which is a finite electrical length. This fixed distance from the ground plane becomes a variable electrical length for the spiral antenna and destroys the frequency independency of the spiral configuration, thus limiting its frequency bandwidth. Such a unidirectional planar spiral antenna is no longer a frequency independent antenna, a price that one pays for controlling the directionality of the spiral antenna radiation patterns. To remedy, in practice spiral antennas are placed over excessively lossy substrates to absorb most of the radiation towards the ground plane, and thus partially remove the effect of the finite distance between the spiral and the ground plane, making them *"quasi-frequency independent antennas"*. The cost of this remedy, however, is the excessive loss (nearly 50%) of the radiation efficiency of the planar spiral antenna. Thus, in applications where the bandwidth need not be too large, or the antenna efficiency is the main concern, the

8

substrate between the planar spiral and the ground plane can be made low loss, which increases the influence of the ground plane, i.e. reduces the antenna bandwidth. The bandwidth analysis thus becomes a critical parameter of study in unidirectional planar spiral antennas.

With the rapid growth of wireless communications and proliferation of peripheral technologies that use wireless technology for data transmission, the demand for multi-functional compact antennas has increased explosively. Particularly, compact antennas with reconfigurable polarization functionality are significantly beneficial for improved system design and performance, as they reduce the cost, volume, and mutual interferences, and increase the wireless communication channel capacity. Spiral antennas, being inherently circularly polarized, offer advantages in certain applications, and thus low profile unidirectional spiral antennas need to be investigated for bandwidth and efficiency, or gain. However, in such applications, the efficiency dominates over other antenna requirements, and a careful investigation of the relationship between the antenna bandwidth and other characteristics becomes essential. Such a study helps in tradeoffs between different electrical parameters of the antennas, and enables achieving design with superior performance.

In this chapter, first, spiral antennas and their radiation properties are briefly reviewed. Then, some basic methods used for design of compact spiral antennas are discussed. Later, the polarization properties of Archimedean spiral antennas are explained, with an emphasis on their dual-polarization capabilities over a shared frequency bandwidth.

2.2 Spiral Antennas

Based on Rumsey's principle [5], the geometry of any frequency independent antenna is defined only by angles rather than lengths. To attain a constant input impedance independent of frequency, such antennas must also have self-complementary structures [7]. This requires an infinitely extended geometry with an infinitely thin planar and perfectly conducing shape of the antenna [8]. The idea of infinite geometry is a theoretical one, which cannot be implemented in practical applications. However, to implement the frequency independent antenna using a finite structure, one can truncate the structure at the point where the current attenuates and goes to zero. The penalty of doing so is the limitation of the lower bound frequency end. Nonetheless, the radiation properties of the truncated antenna will still remain unchanged over a broad frequency range. As such, in practice spiral antennas exhibit a broad frequency bandwidth of about 10:1 or more [6], [9]. It is worth mentioning that most of the radiation, in the first mode, occurs where the circumference of the spiral, is around one wavelength. This portion of the spiral is usually known as the active region [9].

The most popular form of the planar spiral antennas are the equiangular and Archimedean curved spirals, among which Archimedean spiral has received much more attention in practice, because of their superior circularly polarized performance [3], [4]. As such, the Archimedean planar spiral antennas are selected to conduct our study in this thesis. For this reason, the term spiral antenna in the remaining part of this thesis refers to "planar spiral antenna".

A typical geometry of a single-arm Archimedean spiral curve is depicted in Fig. 2.1. The curve is defined by the following equation in polar coordinates,

$$r = a\alpha + r_o \qquad\qquad\qquad (2.1)$$
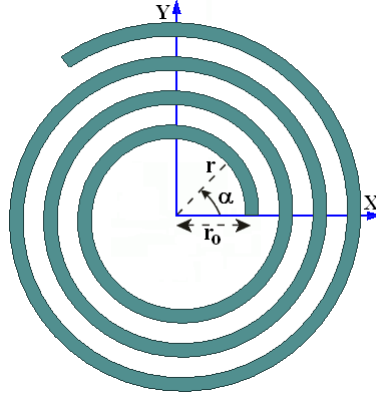
Fig. 2.1. Geometry of single-arm Archimedean spiral and its parameters.

where r_o and r are the radial distances from the origin at angles of α=0 and α (both in radian), respectively. The spiral growth factor is represented by "a"(mm/rad), showing the flare rate of the spiral. The turning direction of the spiral is right-handed or left-handed, if "a" is positive or negative, respectively. A planar antenna, defined by Eq. 2.1, can be easily fabricated using printed circuit board (PCB) techniques.

The free space medium can be imagined as a waveguide with spherical waves of index m. In order for a particular mode of order m to be effectively excited, the minimum cut-off waveguide radius of R_c, the radial distance in spherical coordinates, is required, such that the corresponding wavelength of the mode is governed by [10],

$$\lambda = \frac{2\pi R_c}{m} \qquad\qquad\qquad (2.2)$$

where λ is the wavelength in the free space. Therefore, for the finite structure of the spiral antenna operating at its dominant mode (m=1), the lower- and upper-bound frequencies are limited by the outer and inner radii of the spiral, respectively, as follows:

11

$$\lambda_{lower-bound} \cong 2\pi\, r_{out} \Rightarrow f_{lower-bound} = \frac{c}{2\pi\, r_{out}} \qquad (2.3a)$$

$$\lambda_{upper-bound} \cong 2\pi\, r_{in} \Rightarrow f_{upper-bound} = \frac{c}{2\pi\, r_{in}} \qquad (2.3b)$$

where r_{in} and r_{out} are the inner and outer radii, $\lambda_{lower-bound}$ and $\lambda_{upper-bound}$ are the lowest and highest operating wavelengths, and c is the speed of light in free space. Equations (2.3) are valid when the space between the neighboring wires is much smaller than r, the spiral radius [11].

To understand the circularly polarized nature of the waves generated by the spiral antennas, the dominant mode is considered with $m=1$. In the active region, whose circumference is around one wavelength, currents of the points that are a quarter-wavelength apart along the arm of the spiral have a 90 degree phase difference electrically but have equal amplitudes. Furthermore, the current of these points are perpendicular in space. These conditions make the spiral antenna to radiate circular polarization, with the sense of polarization corresponding to the sense of spiral winding. That is, the polarization sense of the radiated wave is right-handed if the spiral winding direction is counter clockwise and vice versa [9], when the observer looks toward the spiral antenna along the propagation direction.

The generation of the higher order modes using multimode spirals, was first introduced by Deschamps and Dyson [12]. In order for higher order modes to be radiated, a larger active region is required corresponding to at least a circumference of $m\lambda$, for mode m, provided an appropriate excitation network is utilized. These antennas generate broadside radiation patterns with a peak at the boresight angle, when operating at their fundamental mode $m=1$. On the other hand, the higher order modes of $m>1$, when

excited, radiate with a beam peak away from the boresight direction and a null at the boresight angle. The nature of such radiation patterns will be explained shortly. These radiation properties will also be addressed in the next chapter for a four-arm Archimedean spiral antenna, illustrating the corresponding radiation patterns of the higher order modes.

The *N*-arm spiral antenna having *N* distinct terminals may be considered as an *(N-1)*-port antenna. It may be operated simultaneously in *(N-1)* independent balanced modes. By varying the relative excitation of these modes, it is possible to produce a variety of patterns that have applications in communications, pattern shaping, direction finding, adaptive nulling, tracking, and homing over a broad range of frequencies. It is particularly easy to obtain useful directional properties because of some unique properties of the spiral. The basic relations between the mode excitation and the related fields of these multi-arm antennas are reviewed in [12]. They can produce axial beam, or tilted beams that can be conically scanned about the axis of the antenna by a simple phase shift within the excitation matrix [12]. To shed light on the radiation nature of the multi-arm spiral antennas, they can be modeled as antenna arrays where each arm of the spiral forms an element of the array [13]. For simplicity, let each arm be represented by azimuthal or Fourier modes of circular microstrip patch antennas. This type of antenna has a distinct advantage in that its radiation function is a product of two separate functions of angular spaces, i.e. θ and ϕ. Therefore, their far-field circularly polarized radiation patterns, due to the TM_{n1} modes, may be expressed by [13],

$$\left\{ \begin{array}{l} E_\theta = \sum_{n=1}^{N} f_n(\theta) e^{jn\phi} \\ E_\phi = \sum_{n=1}^{N} g_n(\theta) e^{jn\phi} \end{array} \right\} \qquad (2.4)$$

where f and g are the θ-dependent radiation functions, mainly governed by the Bessel functions of order n. Now, consider the voltage excitation of each element with a phase shift of δ_n for each mode such that $\delta_n = n \, \delta_1$. Therefore, Eq. 2.4 can be written as [13],

$$\left\{ \begin{array}{l} E_\theta = \sum_{n=1}^{N} f_n(\theta) e^{jn(\phi-\delta_1)} \\ E_\phi = \sum_{n=1}^{N} g_n(\theta) e^{jn(\phi-\delta_1)} \end{array} \right\} \qquad (2.5)$$

This implies that the beam peak can be rotated in space by changing δ_1. Essentially, the multimode operation will bring significant advantages for beam shaping applications such as direction finding. On the other hand, multi-arm spiral antennas are capable of producing different modes of operation when their arms are properly excited as mentioned before. As an example, consider the four-arm Archimedean spiral antenna shown in Fig. 2.2 [14]. It has four input excitation ports, denoted by A, B, C, and D. The corresponding feed excitation networks for the first four modes of the spiral are given in Table 2.1. For example, to generate a broadside CP radiation pattern at the dominant mode, $m=1$, the amplitude of all ports must be equal with a 90° progressively decreased phase shifts. Since the first mode occurs for the circumference of 1λ, the points that are half-wavelength apart on this circle are electrically out of phase. Taking into account this electrical length and the feeding excitation based on Table 2.1, these points will be in phase generating a broadside pattern at the far-field zone. Similarly, for the second mode,

where the circumference is 2λ, the above mentioned points will be eventually out of phase and generate conical beams with a null at the boresight direction.
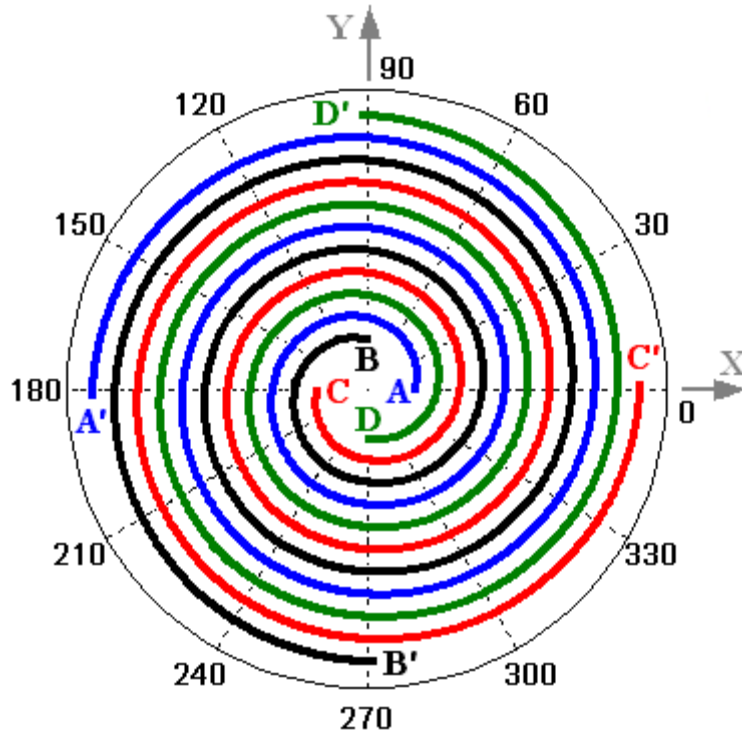
Fig. 2.2. Configuration of the four-arm Archimedean spiral antenna placed in the x-y plane, with its input terminal feeds labeling as A, B, C, and D and end points as A′, B′, C′, and D′.

Table 2.1. The feed excitations for the first four modes of four-arm spiral antenna.

	A	B	C	D
Mode 1	1 < 0°	1 < -90°	1 < -180°	1 < -270°
Mode 2	1 < 0°	1 < -180°	1 < 0°	1 < -180°
Mode 3	1 < 0°	1 < -270°	1 < -180°	1 < -90°
Mode 4	1 < 0°	1 < 0°	1 < 0°	1 < 0°

The analytical solution of the spiral antenna is very complex due to its complicated geometry. Thus, it must be treated using numerical computational methods. Method of moment based numerical approach has been extensively used to study the spiral antennas [15]-[17]. More recently, Finite-Difference-Time-Domain (FDTD) method has been used

for printed spiral antennas backed by a grounded dielectric material [18]-[20]. However, a few publications are available for analytical treatment of the radiation properties of such complex antennas. In [21], the radiation field of the spiral antenna was treated as a linear combination of the wave equation basis functions in spherical coordinates. This requires the knowledge of radial components of both electric and magnetic vector potentials, denoted by F and A, respectively, which can be expressed as a double summation in the following form [21],

$$\begin{cases} A_r = \sum_m \sum_n C_{mn} J_n(kr) P_n^m(\cos\theta) e^{jm\phi} \\ F_r = \sum_m \sum_n D_{mn} J_n(kr) P_n^m(\cos\theta) e^{jm\phi} \end{cases} \qquad (2.6)$$

wherein C and D are the expansion coefficients and J_n and $P_n{}^m$ are the Bessel and associated Legendre functions, respectively. The above unknown expansion factors can be determined by applying appropriate boundary conditions using tangential electric field components on the spiral arms. Once Eq. 2.6 is solved, all electric and magnetic field components can be determined as [22],

$$\begin{cases} E_r = \dfrac{1}{j\omega\varepsilon} \left(\dfrac{\partial^2}{\partial r^2} + k^2 \right) A_r \\[2mm] E_\theta = \dfrac{-1}{r\sin\theta} \dfrac{\partial F_r}{\partial\phi} + \dfrac{1}{j\omega\varepsilon\, r} \dfrac{\partial^2 A_r}{\partial r\,\partial\theta} \\[2mm] E_\phi = \dfrac{1}{r} \dfrac{\partial F_r}{\partial\theta} + \dfrac{1}{j\omega\varepsilon\, r\sin\theta} \dfrac{\partial^2 A_r}{\partial r\,\partial\phi} \end{cases} \qquad (2.7)$$

$$\begin{cases} H_r = \dfrac{1}{j\omega\mu}(\dfrac{\partial^2}{\partial r^2} + k^2)F_r \\[4mm] H_\theta = \dfrac{1}{r\sin\theta}\dfrac{\partial A_r}{\partial \phi} + \dfrac{1}{j\omega\mu r}\dfrac{\partial^2 F_r}{\partial r\,\partial\theta} \\[4mm] H_\phi = -\dfrac{1}{r}\dfrac{\partial A_r}{\partial\theta} + \dfrac{1}{j\omega\mu r\sin\theta}\dfrac{\partial^2 F_r}{\partial r\,\partial\phi} \end{cases} \qquad (2.8)$$

In this thesis, spiral antenna properties are numerically studied using the commercial software packages such as NEC2 [23], which is based on the method of moment, FEKO [24] an EM solver based on the method of moment /finite-element, and finite-element based full-wave EM solver HFSS V.15 [25].

Since circularly polarized (CP) waves are of main interest in our study, it is instructive to briefly explain their radiated fields. Essentially, CP waves are expressed by the left-handed and right-handed polarization components, E_L and E_R, respectively, and they are calculated by [26]

$$\begin{cases} E_L = (E_\theta - jE_\phi)/\sqrt{2} \\[2mm] E_R = (E_\theta + jE_\phi)/\sqrt{2} \end{cases} \qquad (2.9)$$

The far-zone electric field is specified by θ and ϕ components in spherical coordinates as follows:

$$\vec{E} = E_\theta\,\hat{a}_\theta + E_\phi\,\hat{a}_\phi \qquad (2.10)$$

where E_θ and E_ϕ are phasor components in the directions of the unit vectors $\hat{a}_\theta$ and $\hat{a}_\phi$.

Axial ratio is the quality of circular polarization of the wave and it is expressed by the following equation for the left-handed and right-handed circularly polarized waves, i.e. LHCP and RHCP, respectively [26]:

17

LHCP: $$AR(dB) = 20\log\frac{\left|E_L\right| + \left|E_R\right|}{\left|E_L\right| - \left|E_R\right|}$$ (2.11)

RHCP: $$AR(dB) = 20\log\frac{\left|E_R\right| + \left|E_L\right|}{\left|E_R\right| - \left|E_L\right|}$$ (2.12)

As already mentioned, planar spiral antennas radiate bidirectionally. To obtain a unidirectional pattern, one may use a reflector plane of perfect electric conductor. Studies of using a conducting planar reflector have been performed in [27-28]. It has been indicated that when a conducting planar reflector is located in a close proximity to the spiral antenna, it causes an undesired interference with the desired radiation [28-29]. As a result, the operating frequency bandwidth of the antenna is adversely affected and becomes limited. In practical applications, however, compact unidirectional antenna structures with reduced heights and small lateral dimensions are much preferred. In the following section, some well-known techniques will be reviewed for spiral antennas for both miniaturization and low profile applications.

2.3 Compact Spiral Antennas

Nowadays, compact antennas are in great demand in many wireless communication systems. The compactness of an antenna structure depends on its axial and lateral dimensions. The former determines the antenna profile and the latter becomes important in integrating antennas with other radio frequency and electronic devices as well as reducing its EM shadowing effects in reflector antenna applications. In antenna engineering, different techniques are utilized to effectively reduce each of these dimensions, which are discussed separately in the following sections.

2.3.1 Miniaturization Techniques for Spiral Antennas

The main requirement in the antenna miniaturization is to increase the electrical path length and thus slow the phase velocity [30]. This will, in turn, shift down the lower operating frequency. To clarify this, using the analogy of a center-fed infinite bi-conical antenna to a uniform transmission line extended to infinity [22], the phase velocity of the line is described by [6], [31],

$$v_p = \frac{1}{\sqrt{LC}} = \frac{1}{\sqrt{\mu\varepsilon}} \qquad (2.13)$$

wherein L and C are the series inductance and shunt capacitance per unit length, respectively. Therefore, the phase delay can be controlled by changing the above mentioned reactive parts. There are several ways to do this, such as material loading, inserting lumped elements, and shaping the antenna structure itself. In the material loading method, the miniaturization is achieved using the materials with permittivity and or permeability of greater than unity to slow down the phase velocity based on Eq. 2.13 [30]. Although dielectric materials with large permittivity values significantly contribute to reduction of the antenna size, they also limit the impedance bandwidth. Furthermore, high-contrast dielectrics deteriorate antenna efficiency due to the dielectric loss. As such, loading the antenna with materials with almost equal values of ε_r and μ_r [30] may be a better alternative for both antenna miniaturization and retaining the impedance bandwidth. Of course, such materials must be low loss [30]. As mentioned earlier, another miniaturization method to effectively enlarge the electrical length is to shape the antenna geometry itself. This can be readily done using several techniques namely meandering, zigzagging [32], slot loading, and bending [30]. All these techniques lead to

increase the effective electrical length of the antenna and subsequently lower the operating frequency. As an example, an undulated transmission line with a square shape unit cell is illustrated in Fig. 2.3.

(a)   **(b)**
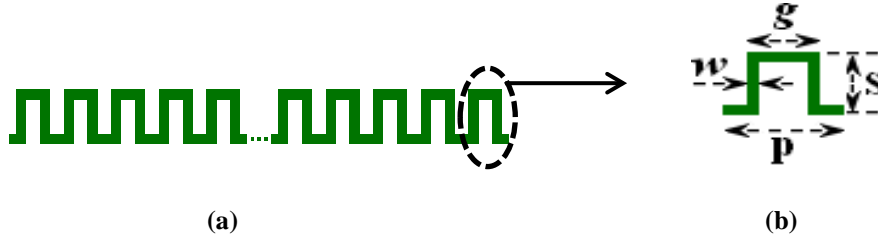
Fig. 2.3. (a) Meandered transmission line with (b) a square pulse unit cell. The line is 720mm long consisting of 60 unit cells, *w*=3mm, *g*=11mm, S=11mm, and p=15mm.

In fact, meandered transmission lines increase the effective dielectric constants. This can be easily proved by treating the transmission lines as an equivalent dielectric medium in the form of a two-port network, in which the effective dielectric constants of the lines are extracted from the scattering parameters of the network [33]. In particular, the S_{21} of a transmission line of length l is [34],

$$S_{21} = e^{-(\alpha + j\beta)l} \qquad (2.14)$$

wherein α and β are the attenuation and propagation constants, respectively. From Eq. 2.14, it is clear that the phase of the S_{21} depends only on β, from which the dielectric wavelength, λ_d, is obtained as,

$$\lambda_d = \frac{-\angle S_{21}}{2\pi l} \qquad (2.15)$$

Therefore, the effective dielectric constant of the undulated line can be determined from the following equation:

$$\varepsilon_{eff} = \left(\frac{\lambda_0}{\lambda_d}\right)^2 \qquad (2.16)$$

20

As an example, the undulated transmission line shown in Fig. 2.3 is investigated, when it is suspended in air and backed by an infinite ground plane at a distance of 1.6mm. The resulting effective dielectric constant is plotted in Fig. 2.4a. It is shown that the meandered line, even with a supporting material such as air, behaves like dielectric materials with effective dielectric constants of considerably much larger than that of air, in the order of 6. If high-contrast dielectric material, e.g. ε_r=9.8, is replaced with air, i.e. the undulated line is etched over a grounded substrate with ε_r=9.8, the effective dielectric constant of the undulated line under study remarkably increases to ε_{eff}=50, as depicted in Fig. 2.4b, resulting in a considerable size reduction of the antenna structure. Therefore, such meandered lines can be effectively used for antenna miniaturization applications, instead of using high contrast dielectric materials, thus eliminating the associated dielectric loss.
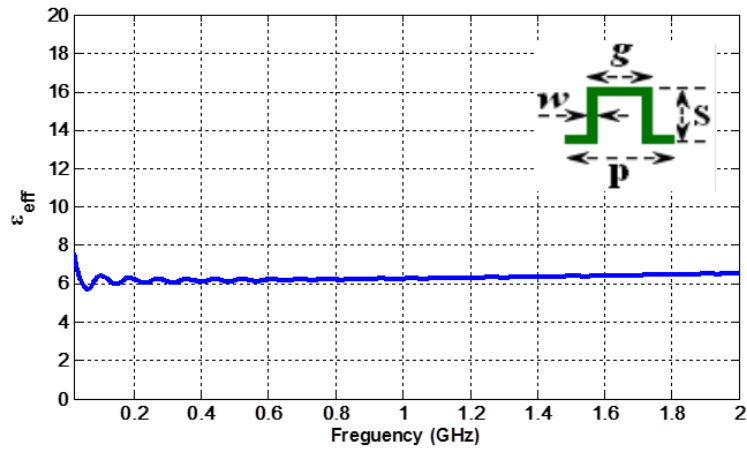
(a)
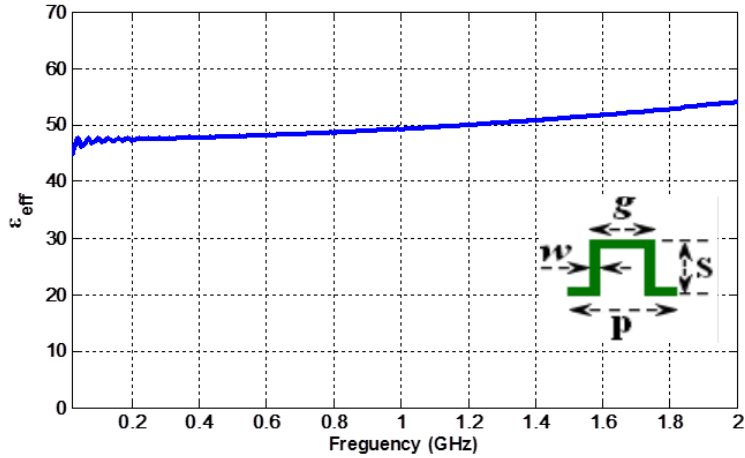
(b)

Fig. 2.4. Effective dielectric constant of the meandered transmission line shown in Fig. 2.3, extracted from the phase of the S_{21} using Eqs. 2.15 and 2.16. The line is 720mm long consisting of 60 unit cells with w=3mm, g=11mm, S=11mm, and p=15mm. The line is placed at a distance of 1.6mm from ground plane. The substrate is (a) ε_r=1.0 and (b) ε_r=9.8.

A few examples of the miniaturized and low profile spiral antennas are briefly reviewed herein, which have been recently reported in the literature.

A miniaturized two-arm spiral antenna was developed using inductive and capacitive loadings in [35]. The inductive loading was performed by meandering and coiling each arm of the spiral, especially near the outer ends, to improve the low frequency band performance. The capacitive loading was implemented by utilizing a dielectric material. A conducting ground plane covered by a thin layer of ferrite was also used to achieve low profile structures. It was shown that the lower frequency of the miniaturized inductively loaded antenna shifted down, when compared with the unloaded antenna. When it was backed by the ferrite coated ground plane to obtain unidirectional patterns, the performance remained almost unchanged. This work was later studied to improve the CP performance of the miniaturized antenna at lower frequencies. To do so, the resistive loading was employed to the spiral arm ends in order to attenuate the

22

unwanted reflections. Zigzag miniaturized spiral antenna was employed over the same ferrite coated ground plane [36]. However, the 14-inch zigzag antenna [36] failed to generate CP waves at the low frequency bands after miniaturization. Although the operating frequency bands have been lowered to miniaturize the antennas in [35], [36], the CP performances of the antennas were degraded. In particular, the antennas become almost linearly polarized at the low frequencies.

2.3.2   Cavity Backed Low Profile Spiral Antennas

As already mentioned, a free-standing spiral antenna radiates circularly polarized waves in both upper- and lower-half space. That is, it is a bidirectional antenna. However, in most practical applications, unidirectional antenna patterns are desired. One of the simple approaches to make a unidirectional spiral antenna is to use a perfectly conducting plane to suppress the back radiation. However, as the ground plane moves to the close proximity of the antenna, the spiral antenna performance degrades.

In this section, attention is drawn to low profile techniques using cavity backed absorber-filled materials introduced in [37], [38]. The goal is to reduce the axial size of the antenna as small as possible without causing remarkable changes to the antenna characteristics such as gain, axial ratio, and impedance bandwidth.

A shallow cavity backed two-arm Archimedean spiral antenna was proposed by Nakano [37]. It was shown that when the antenna was supported by a conventional cavity of 0.047λ height, the antenna impedance behavior is adversely affected, especially at the lower operating frequencies. This is due to the fact that strong reflections of the electromagnetic fields exist at the bottom of the cavity. The antenna axial ratios were drastically degraded, turning it to a linear polarized antenna at low frequencies. To

23

circumvent the problem, insertion of a thin strip of absorber was proposed in [37], a typical geometry of which is shown in Fig. 2.5. The unwanted reflections from the cavity are effectively suppressed by inserting the ring-shaped absorber inside the cavity near its wall, which facilitates reducing the antenna height.
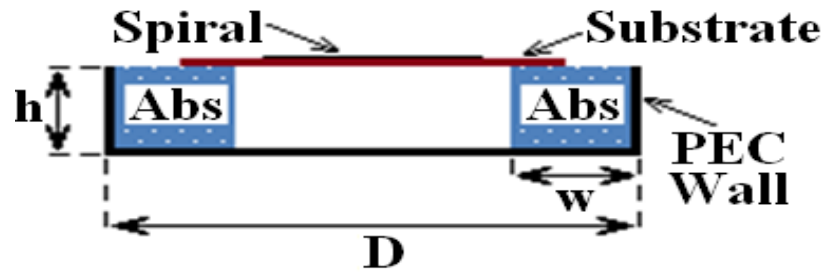
Fig. 2.5. Side-view of a spiral antenna with supporting cavity filled by a thin strip absorber.

In practice, the above two-arm Archimedean spiral antenna requires a balun circuit to generate the balanced spiral modes. The idea of utilizing a small disk as a balun was introduced by Kaiser in 1960 [4] and it was later revisited in [38-40]. In particular, the possibility of exciting balanced modes in single-arm Archimedean spiral antennas was investigated in [38] without using the balun. The spiral is supported by a cavity. A small disk, as a ground plane, is embedded inside the cavity. To reduce the reflections from the spiral arm end a ring shaped absorber was placed inside the cavity near its wall, similar to the previous case. The diameter of the cavity was slightly larger than the spiral aperture. A representative structure of this type of antenna is shown in Fig. 2.6.
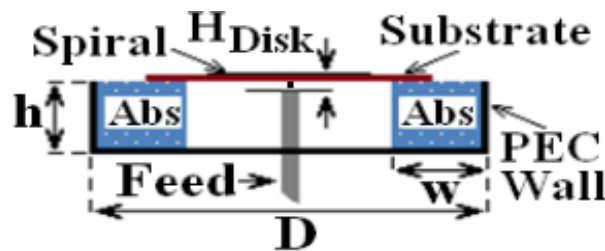
Fig. 2.6. Cross-section view of the proposed low profile single-arm Archimedean spiral antenna with a small ground disk supported by a cavity.

24

The important parameters in designing the above low profile antenna are the disk radius and its distance from the spiral antenna. In particular, when the disk size is larger than the active region of the antenna, it acts as a conventional ground plane, which fails in low profile antenna implementation.

A compact curl antenna, i.e. a single-arm nearly single-turn spiral antenna, was investigated in [41], etched on a grounded dielectric slab of 1.6mm height and backed by a cavity-filled absorbing material of 7mm thickness at the frequency of 4GHz. A curved slot was placed underneath the active region of the antenna under study, which increased the back radiation. A thin cavity filled absorber was placed under the slotted ground plane to suppress the undesired radiation in the lower-half space. A low profile four-arm Archimedean spiral antenna was also investigated in [42], [43], backed by a partially filled absorber cavity with a 7mm height. The antenna exhibited excellent CP performance with broadside radiation patterns over the frequency range of 1.0 - 7.0 GHz, with axial ratios well below the 3dB level.

In the aforementioned works, the emphasis was placed on implementation of low profile single-, dual-, and four-arm Archimedean spiral antennas, with broadside radiation patterns using a cavity filled with a ring-shape absorber. However, higher order modes of the antenna have not been investigated. Complete studies of the higher order modes in four-arm Archimedean spiral antennas will be addressed in chapter 3 of this thesis.

2.4   Spiral Antennas with Polarization Diversity

Over the last decades, frequency reuse antennas with higher bit-rate capabilities and enhanced channel capacities have become extremely popular in a variety of applications, such as multimode Global Positioning Systems (GPS), modern satellite navigation, and radar systems. Two orthogonally polarized waves are employed for each transmit and or receive terminals, which increase the link capacity. The orthogonality is normally realized by using two perpendicularly linearly polarized signals or two circularly polarized ones with different senses of polarization. In particular, the utilization of both clockwise and counter clockwise CP signals is necessary in some radio-astronomical applications, studying the surrounding atmosphere of planets [44], as well as in direction finding, tracking, and homing. Implementing both such orthogonally polarized waves in a single aperture antenna is highly desirable with the ever-growing technology progress in compact, reconfigurable, and multifunctional antennas. Therefore, the antennas for transmit and receive terminals can be integrated into one, which significantly reduces the system volume and complexity.

The possible polarization diversity scenarios include vertical-horizontal linear polarization and right-hand and left-hand circular polarizations. The latter is of our interest in this thesis. For such polarization selectivity, frequency independent antennas, such as helices and spirals, are best candidates. Since the polarization of these antennas is predominantly dependent on the winding direction of their arms, an opposite sense of polarization can be obtained, when they are fed at outer ends of their arms in helical [45] and spiral [46-47] antennas. However, a simultaneous excitation of both senses of polarization requires complex and bulky feeding networks, which are not easy to

26

incorporate in practice at both terminals. The possibility of generating both senses of CP, with a central feeding method in conical logarithmic spiral antennas, was introduced and experimented in [48-50], and later the radiation mechanism was briefly explained and patented in [51], for bidirectional and planar logarithmic spiral antennas in free space. In the open literature, the polarization diversity has not been explained for low profile and planar Archimedean spiral antennas with unidirectional radiation patterns. Moreover, the frequency responses have not been elucidated in the above works.

In this thesis, low-profile, unidirectional, planar and quasi self-complementary four-arm Archimedean spiral antennas are investigated to be used for polarization diversity applications generating both right- and left-hand circularly polarized waves [52], [53]. It is fully addressed in chapter 4 and its performance as a primary feed in reflector antennas will be discussed in chapter 5.

2.5 Backward Spiral Antennas

Antennas with backward radiation patterns are significantly advantageous in small front-fed reflector antennas, as they can be mounted directly from the apex of the reflector through a single rod. As such, the need for supporting struts is eliminated, resulting in lesser blockage on the reflector illumination aperture. The very first designs of such interesting feeds were introduced by Silver [54] and Clavin [55] for dipole feeds, in which a disk and cylindrical cavity were utilized to direct the dipole radiation in a half-space region, respectively. Other well-known rear-radiating feeds are the splash-plate feeds [56-57], cup feed [58-59], hat feed [60], dipole-disk with beam-forming ring [61], backward printed dipole feeds [62-63], and dipole-conical reflector [64]. The aforementioned antennas were designed for linear polarization and possibility of utilizing

cross-dipole feeds have also been reported for circularly polarized (CP) applications. These radiating elements are resonant structures and provide backward radiation patterns with a very narrow frequency bandwidth.

Among frequency independent antennas, helical antennas, as rear-radiating feeds, have also been the subject of interest among antenna engineers and their backward radiation properties are reported in [65-69] for circularly polarized applications. In particular, a monofilar helical antenna was investigated over a finite ground plane in [68]. It was shown that the size of the ground plane played a key role to determine the direction of the radiation. That is, the radiation is forward for a ground plane size larger than the helix diameter and it becomes backward when the ground plane size reduces to the order of helix diameter [68]. Another excellent CP candidate is the spiral antenna, which is a bidirectional radiator in its free-standing form. To obtain unidirectional radiation patterns, the spiral antenna is usually backed by a ground plane, resulting in a forward radiating antenna, well studied in the literature. However, to the best of my knowledge, the backward radiating properties of spiral antennas have not been investigated in the open literature so far.

In this thesis, unique backward radiation properties of compact four-arm Archimedean spiral antennas are explored and investigated. Conventionally, an active zone in the order of one wavelength is required to have the spiral antenna operate in its first mode, producing broadside radiation patterns. It will be demonstrated that a reflector backed four-arm spiral antenna with a diameter of much less than the conventional active zone is capable of effectively directing the same broadside radiation into the backward region with an opposite sense of polarization. The antenna such developed is well suited

as a primary feed in small front-fed parabolic reflector antennas. The circular polarization performance of the proposed rear-radiating spiral antenna along with its performance as a primary feed in parabolic reflector antennas will be investigated in chapter 5.

2.6   Proposed Study

A four-arm Archimedean spiral antenna is selected to study its radiation properties at different operating modes, which generate broadside and conical radiation patterns. The concept of absorber-filled cavity along with a small conducting disk is employed to reduce the axial size of the antenna operating at both dominant and higher order modes. It will be shown that the small disk inside the cavity attributes to generate balanced spiral modes without using extra balun circuits. In particular, the effectiveness of the above methods is proved at the higher order modes in chapter 3.

Unidirectional spiral antennas with polarization diversity are fully addressed in chapter 4. Radiation mechanism of a center-fed four-arm Archimedean spiral antenna, capable of generating broadside radiation patterns with both senses of circular polarization, is explained in this work. The required feeding excitation networks are mathematically described for a general case of N-arm spiral antenna, using incident and reflected travelling waves. The condition to generate circular polarization diversity is then addressed and applied to four-arm Archimedean spiral antennas, whose circumference is less than three wavelengths. Low-profile antennas backed by conducting ground planes are designed and extensively investigated to study different antenna parameters such as gain, cross-polarization, pattern symmetry, and axial ratios. Proposed antennas with two ground plane sizes are studied. It is shown that both senses of circular

polarization are produced, sharing a respectable frequency bandwidth, controlled by the supporting ground plane sizes.

The performance of the proposed dual-polarized spiral antenna as an illuminating source in parabolic reflector antennas is presented in chapter 5, which could be used in frequency reuse applications and standard CP antennas, to determine the sense of polarization of an antenna under test in practice. In addition, backward radiation properties of a compact and center-fed four-arm Archimedean spiral antenna are investigated and its applications in symmetric front-fed parabolic reflector antennas are studied. It is shown that the spiral antenna generates broadside CP backward radiation patterns with an opposite sense of polarization to the spiral winding direction, when its circumference is well below the conventional active zone of the first mode, which is in the order of one wavelength.

Finally, the proposed dual-polarized spiral antennas are loaded with dielectric material for both frequency-tuning applications and realizing compact structures, which are presented in chapter 6. Three different dielectric structures are studied, namely full, partial, and grooved substrates.

2.6 Summary

In this chapter, a brief background theory of the spiral antennas and their circularly polarized radiation properties were provided. In particular, the emphasis was placed on Archimedean type spiral antennas. A short review of the analysis of spiral antennas was given. Some miniaturizing techniques, based on slowing down the phase velocity, were explained. It was demonstrated that the effective dielectric constant could

be increased, when meandered transmission lines were etched on even low-contrast substrates. In addition, transformation techniques from bidirectional to unidirectional radiation patterns for the spiral antennas were addressed. In particular, cavity backed methods were discussed to develop low-profile single, dual, and four-arm spiral antennas. The higher order spiral modes have not been investigated in literature, in none of the reported works to the best of my knowledge, which will be addressed in this thesis. Polarization diversity was reviewed for both right and left-handed CP waves for a center-fed Archimedean spiral antenna. Finally, the proposed concept was introduced, investigating radiation and dual-polarization properties of four-arm Archimedean spiral antennas.

Chapter 3

Radiation Properties of Conventional and Low-Profile Four-Arm Archimedean Spiral Antennas

3.1 Introduction

N-arm spiral antennas can produce broadside and tilted beams that can be conically scanned about the axis of the antenna by appropriate phase shifts within the excitation matrix [12]. These intriguing properties are of special interest in communications, adaptive nulling, beam shaping, direction finding, and GPS applications. As known, they generate CP patterns with the sense of polarization according to the spiral winding direction as explained in the previous chapter.

In this chapter, multi-mode four-arm Archimedean spiral antennas are investigated. To better understand the nature of spiral antenna radiation, first a conventional four-arm Archimedean spiral antenna is presented. Both free standing and reflector backed antennas are considered. Their axial ratios, co-, and cross-polarization radiation patterns are studied, for their dominant and second order modes. These results are carried out using the Numerical Electromagnetic Code, NEC2 [23], which is based on the method of moments. To reduce the height of a conventional spiral antenna over a ground plane, a partially-absorber filled cavity backed spiral antenna is proposed. To generate balanced spiral modes, a small conducting disk in embedded inside the cavity, to act as the ground plane for the feeding coaxial cables. This feeding technique greatly simplifies the feed network, and eliminates the need for a complex

balun. This is due to the fact that, for balanced feedings, the sum of input excitation currents of four spiral terminals adds up to zero, for the first three modes of the spiral. Thus, there will be no reflected current on the external walls of the input coaxial cables, which eliminated the need for a complex balun to do the same. The proposed antenna is fabricated and tested. The results will be shown later, along with the simulated results of the antenna. The latter are obtained by a commercial method of moment based software FEKO [24].

3.2   Conventional Four-Arm Spiral Antennas [14, 70]

In this section, the performance of a four-arm Archimedean spiral antenna is investigated using NEC2 operating at the first and second modes. The dominant mode generates broadside radiation patterns with a peak at $\theta = 0^o$, whereas the higher order modes radiate conical beams with the beam peak moving towards the spiral plane. Initially, an extensive study was performed to determine the most appropriate spiral parameters, i.e. the spiral constant a, and the spiral conductor widths w to yield the best radiation characteristics in gain and axial ratio, in the upper half space, with small number of turns. For the sake of brevity, here only the final results are provided, which are $a = 3.8197 \text{ mm/rad}$ and $w = 3 \text{ mm}$, for the antennas designed to operate in the GPS bands. The spiral constant is obtained for self-complementary spiral geometry and it depends on w, as governed by Eq. A.3 in Appendix A. The geometry of the antenna is shown in Fig. 3.1. From the spiral winding direction, it is clear that the antenna dominantly generates right-handed CP waves. Two different cases are investigated, namely the spiral antennas in free space and over an infinite ground plane. Four different spiral sizes are studied for each case, having different number of spiral turns, i.e. N, as:

33

- N = 2.5 turns,

- N = 3 turns,

- N = 3.5 turns, and

- N = 4.5 turns.

The feed excitations are the same as those given in Table 2.1, chapter 2.
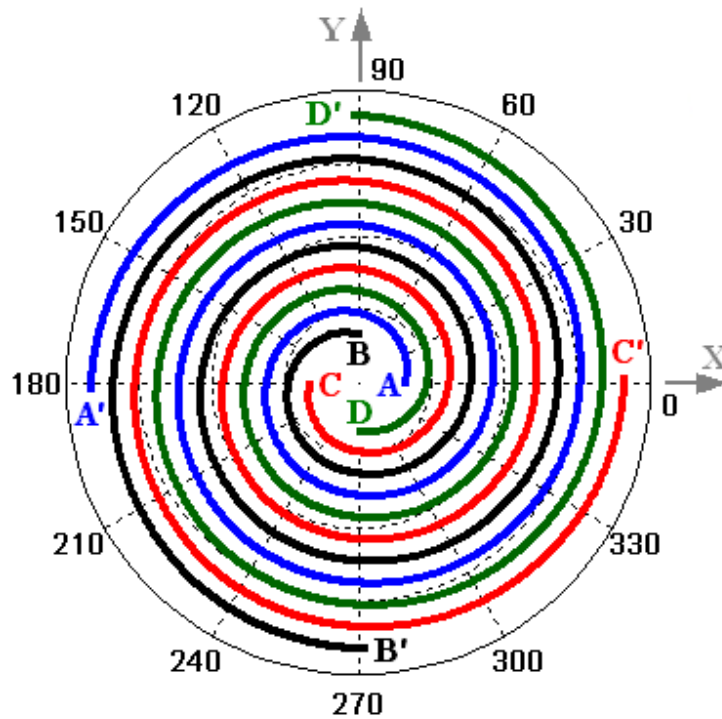
Fig. 3.1. Top view of the four-arm Archimedean spiral antenna generating right-handed CP, when fed at its central terminal ABCD.

3.2.1 Four-Arm Spiral Antenna in Free Space

The CP radiation patterns of the free standing four-arm Archimedean spiral antenna at its first mode are shown in Fig. 3.2 for different N. The maximum gain occurs at the boresight angle, as expected, and it increases slightly as the number of turn increases. It is worth mentioning that the radiation pattern cuts, in the azimuth direction, are identical at both principal

planes, i.e. $\phi = 0^o$ and 90° planes, due to the symmetrical structure of the antenna under investigation.
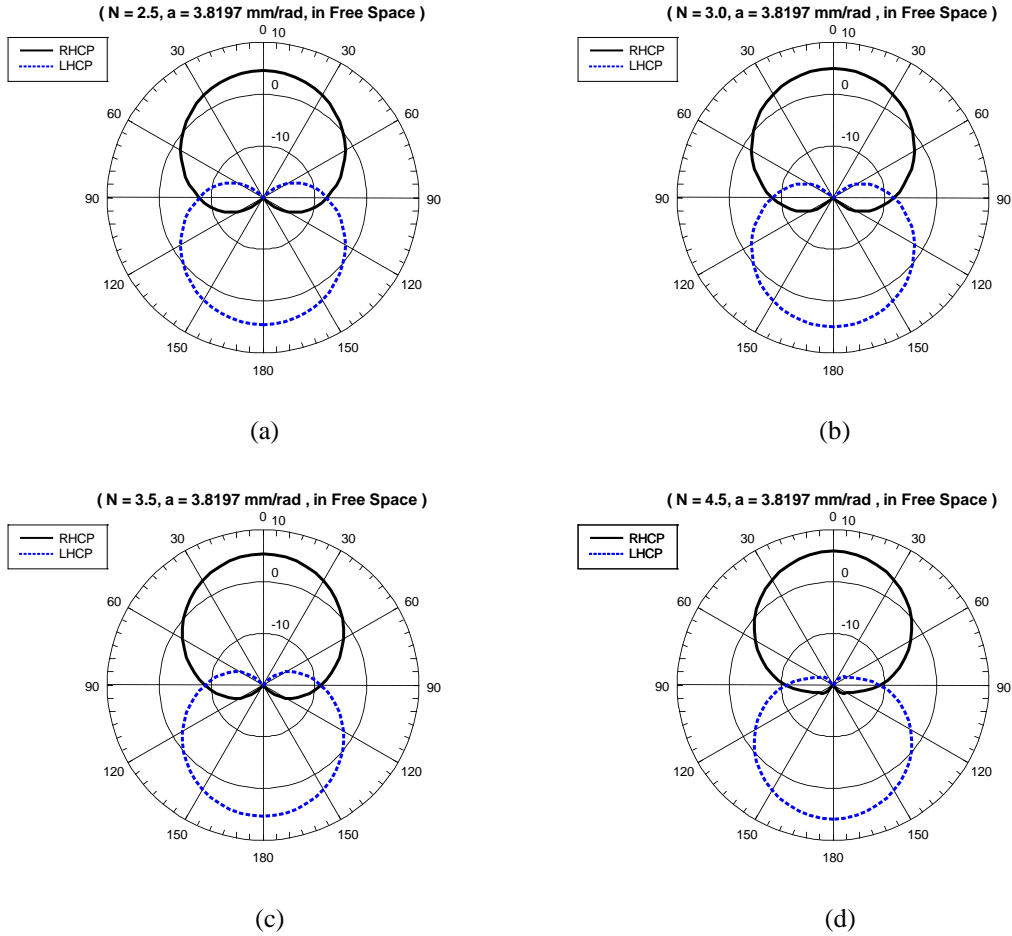
Fig. 3.2. Principal plane CP radiation patterns of the 4-arm spiral antenna in free space for the first mode, with a = 3.8197mm/rad, (a) N=2.5, (b) N=3.0, (c) N=3.5, and (d) N=4.5.

The corresponding axial ratios are illustrated in Fig. 3.3. The 3dB axial ratio beamwidth covers a wide angular range of at least $\pm 50^o$ for all values of N. As shown, the 3dB axial ratio beamwidth reaches to about $\pm 60^o$, as N grows to 4.5. This is because the reflections from the spiral end arms become more negligible as N increases.
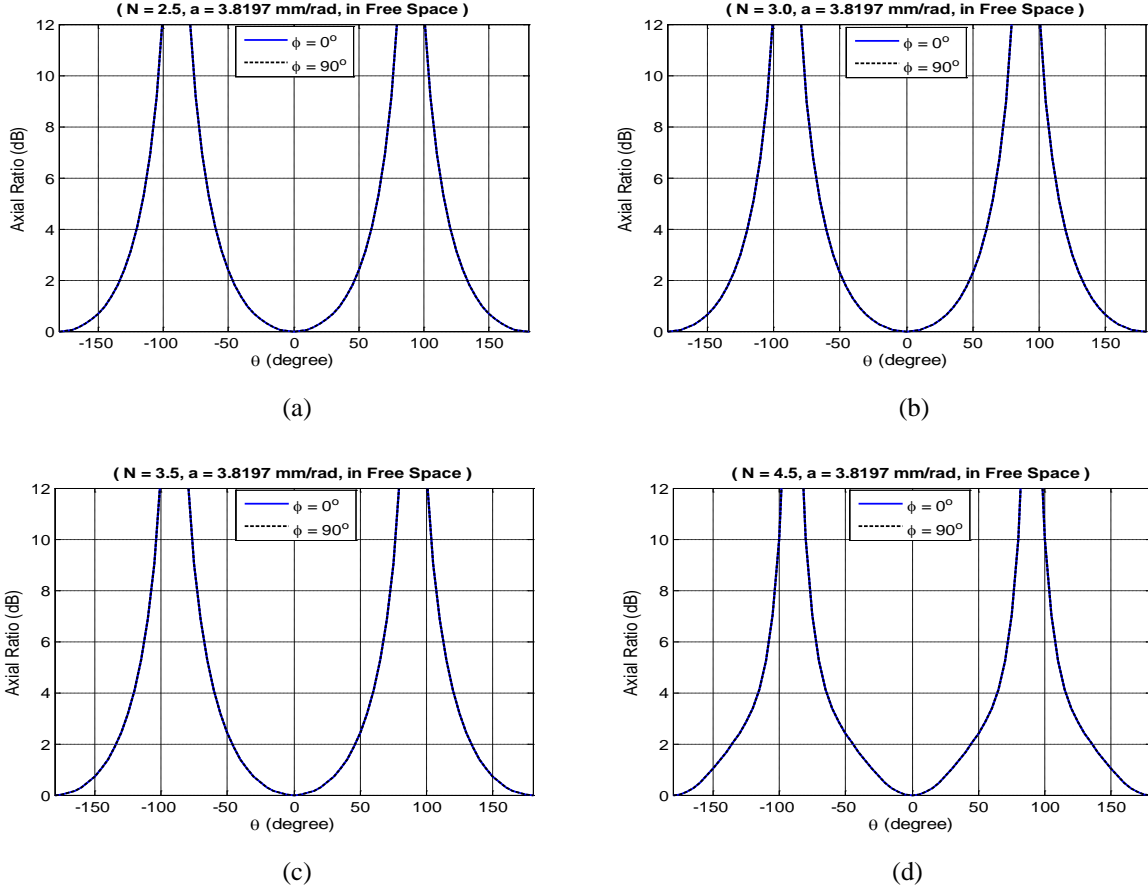
Fig. 3.3. Principal plane axial ratios of 4-arm spiral antenna in free space for the first mode, with a=**3.8197mm/rad, (a) N=2.5, (b) N=3.0, (c) N=3.5, and (d) N=4.5.**

The boresight power gain of the antenna increases from 4.59 dBic to 5.91 dBic, as N varies from 2.5 to 4.5, as given in Table 3.1. It is also interesting to note that the forward radiation is right handed circularly polarized (RHCP), while the back radiation is left handed circularly polarized (LHCP). These results clearly exhibit the excellent performance of the designed four-arm Archimedean spiral antenna, with small number of turns, as small as N = 2.5. The radiation patterns are symmetric with 3dB axial ratio beamwidth of ±50°, and no side lobe levels, which will guarantee a well-defined and unique phase center location for the antenna.

Table 3.1. Power gain of the 4-arm spiral antenna in free space operating at the first mode

# of turns	Mode 1	
	Gain(dBic)	Beam Peak
N= 2.5	4.59	0°
N= 3.0	5.01	0°
N= 3.5	5.36	0°
N= 4.5	5.91	0°

For the second mode, the main beam is split with a null at the boresight angle of θ= 0° as plotted in Fig. 3.4, showing the CP radiation patterns. The gain of the antenna operating at its second mode increases as N grows, as shown in Table 3.2. Also, the radiation patterns are conical in shape, with the peak of the main beam direction scanned to around 40° angle.

(a)

(b)

(c)

(d)
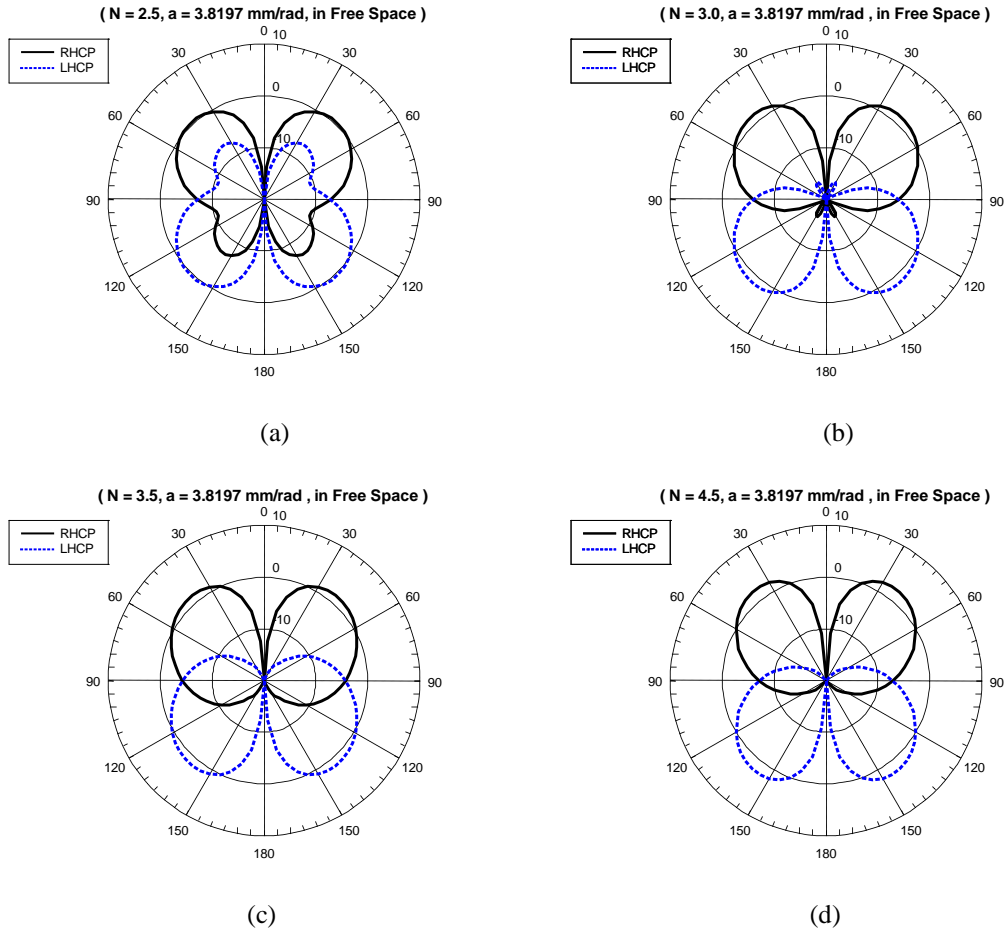
Fig. 3.4. Principal plane CP radiation patterns of 4-arm spiral antenna in free space for the second mode with *a*=3.8197mm/rad, (a) N=2.5, (b) N=3.0, (c) N=3.5, and (d) N=4.5.

37

Table 3.2. Power gain of the 4-arm spiral antenna in free space operating at the second mode

# of turns	Mode 2	
	Gain(dBic)	Beam peak
N= 2.5	1.14	40°
N= 3.0	1.57	40°
N= 3.5	1.66	40°
N= 4.5	2.21	40°

The axial ratios of the antenna are plotted in Fig. 3.5 for all values of N equal to 2.5, 3.0, 3.5, and 4.5, for the second mode. It is shown that for N larger than 3 a good axial ratio less than 3 dB is obtained, and it improves as N increases from 4 to 4.5. Similar to any multimode antenna, the effective aperture size of the antenna should be large enough to support the desired higher order mode. This is also the case for the spiral antenna, which has active radiation zones, i.e. circles, corresponding to each mode, and having circumferences equal to $m\lambda$, when m denotes the mode order. This is illustrated well in Table 3.2, where the radiation gain increases with the number of spiral turns, i.e. the spiral diameter.

(a)

(b)

(N = 3.5, a = 3.8197 mm/rad, in Free Space)

(N = 4.5, a = 3.8197 mm/rad, in Free Space)

(c)

(d)
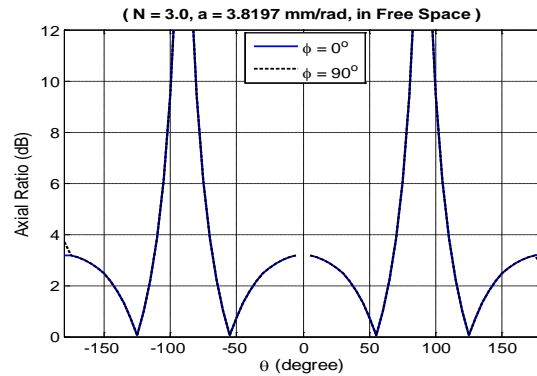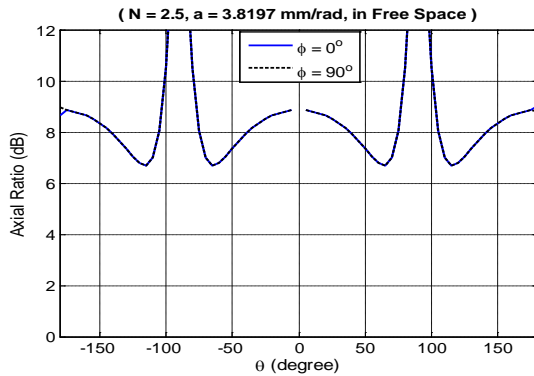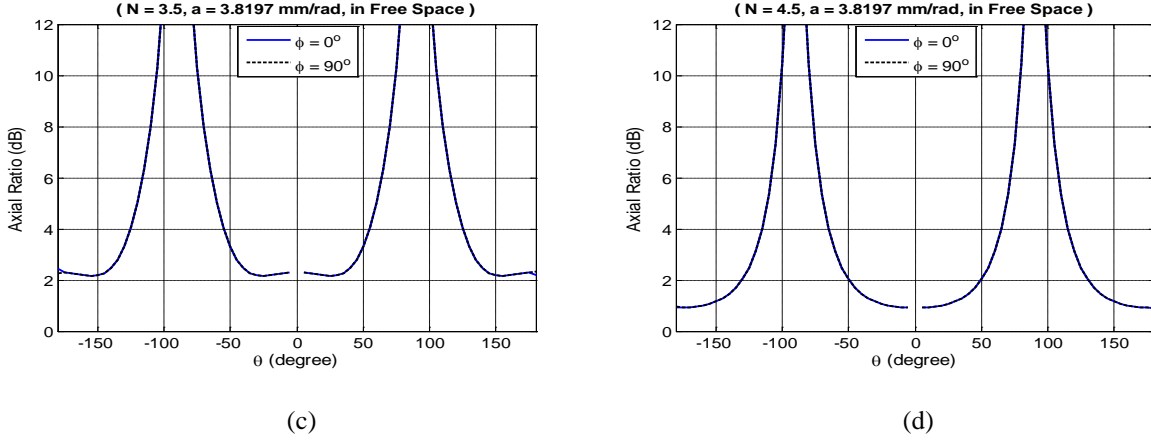
Fig. 3.5. Principal plane axial ratios of 4-arm spiral antenna in free space for the second mode with
***a*=3.8197mm/rad, (a) N=2.5, (b) N=3.0, (c) N=3.5, and (d) N=4.5.**

3.2.2 Four-Arm Spiral Antenna over an Infinite Ground Plane

In this section, the four-arm Archimedean spiral antenna under study is placed over an infinite ground plane to generate unidirectional radiation patterns. The surrounding medium is air and the ground plane is a perfect electric conductor (PEC). As known, when a planar antenna is backed by a PEC ground plane, the distance between the antenna and PEC plays an important role in the antenna performance. For instance, for a quarter wavelength distance, the radiations from the antenna and its image will only add in-phase at the $\theta=0^o$ direction. This distance is selected to conduct our studies over an infinite ground plane.

The CP radiation patterns of the first mode are shown in Fig. 3.6. Similar to the free space case, the antenna generates broadside radiation patterns with the right-handed polarization sense; except the patterns are now unidirectional with the presence of the infinite ground plane. Particularly, the cross-polarization level, i.e. the left-handed CP component, is -15dB below its corresponding co-polar component, when N is equal to 2.5 and 3.0.

The peak gain, in the main beam direction, and the sense of polarization are given in Table 3.3. As can be seen, the peak gain decreases and then increases with N, and they are around 8dBic. The sense of polarization is right-handed for all values of N.

Table 3.3. Power gain of 4-arm spiral antenna over an infinite ground plane operating at the first mode

# of turns	Mode 1 (h=λ/4)		
	Gain (dBic)	Main beam	Polarization sense
N= 2.5	8.85	0°	Right
N= 3.0	8.20	0°	Right
N= 3.5	7.60	0°	Right
N= 4.5	9.35	0°	Right

(a)

(b)

(c)

(d)
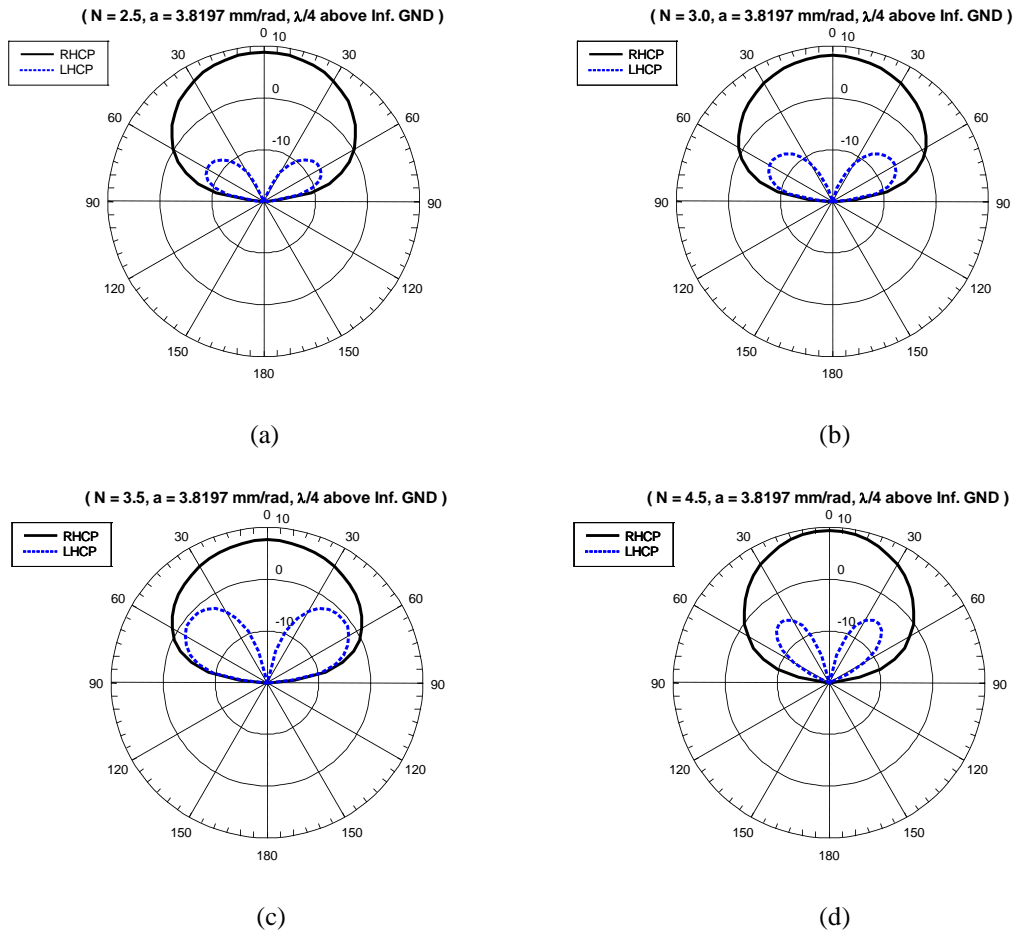
Fig. 3.6. Principal plane CP radiation patterns of 4-arm spiral antenna λ/4 above infinite GND plane for the first mode with *a*=3.8197mm/rad, (a) N=2.5, (b) N=3.0, (c) N=3.5, and (d) N=4.5.

The corresponding axial ratios are plotted in Fig. 3.7. It is observed that the 3dB axial ratio beamwidth gradually narrows as N increases. This is because of the increased contributions from the image currents on the ground plane, which become noticeable as the spiral arms grow.
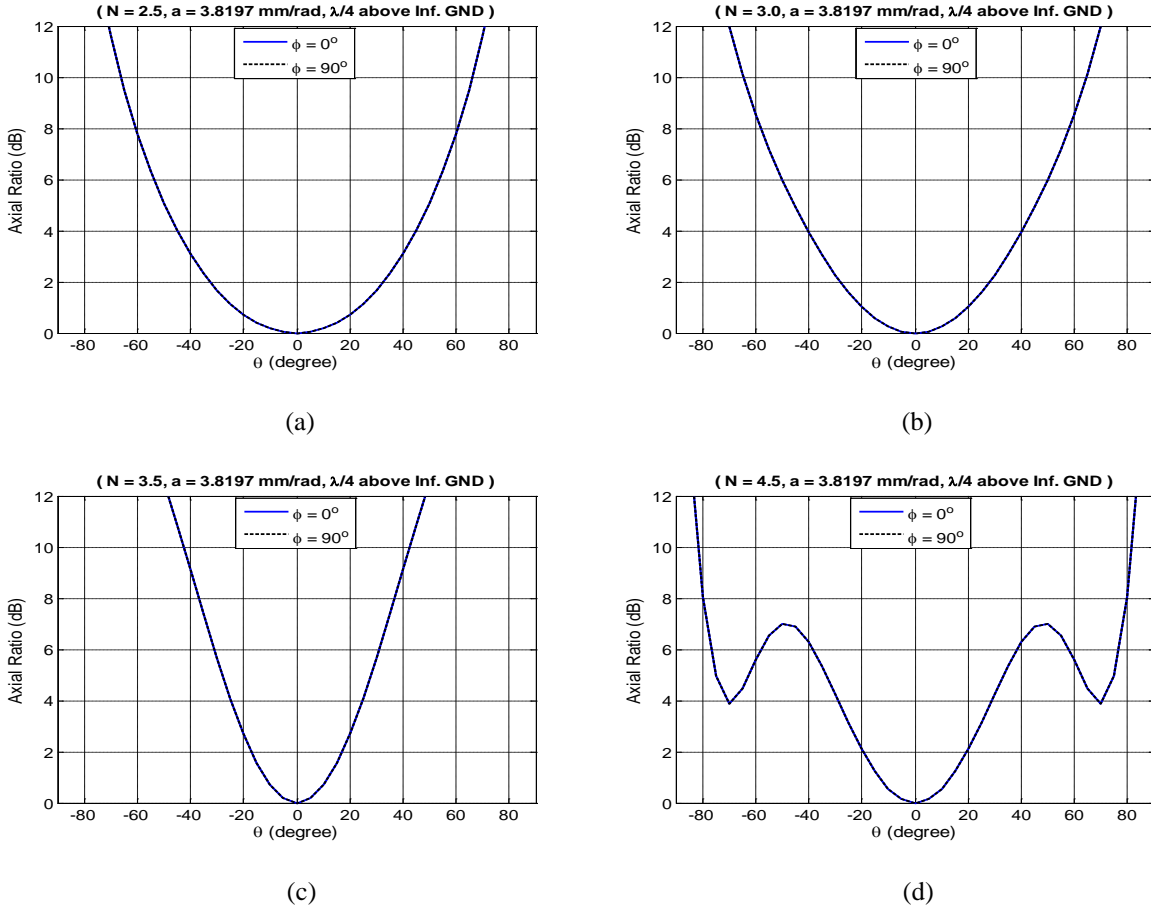
Fig. 3.7. Principal plane axial ratios of 4-arm spiral antenna λ/4 above infinite GND plane for the first mode with *a*=3.8197mm/rad, (a) N=2.5, (b) N=3.0, (c) N=3.5, and (d) N=4.5.

The CP radiation patterns for the second higher order mode are shown in Fig. 3.8, when h=λ/4. The main beam is split and the sense of polarization is right-handed for all cases. The best CP performance is obtained when N=2.5, as illustrated in Fig. 3.8a. The cross-polarization levels tend to increase for all other cases. Table 3.4 summarizes the results for the second mode. As can be seen, the peak gain is around 6 dBic, with the right-handed polarization sense for all cases.

They all have boresight-null patterns, as expected for the second mode. The main beam direction scans toward the end-fire direction, as N varies from 2.5 to 3.5, and it moves 15° back toward the boresight direction when N=4.5.

Table 3.4. Power gain of 4-arm spiral antenna over an infinite ground plane operating at the second mode

# of turns	Mode 2 (h=λ/4)		
	Gain (dBic)	Main beam	Polarization sense
N= 2.5	6.13	40°	Right
N= 3.0	6.26	40°	Right
N= 3.5	6.62	50°	Right
N= 4.5	6.10	35°	Right

(a)

(b)

(c)

(d)
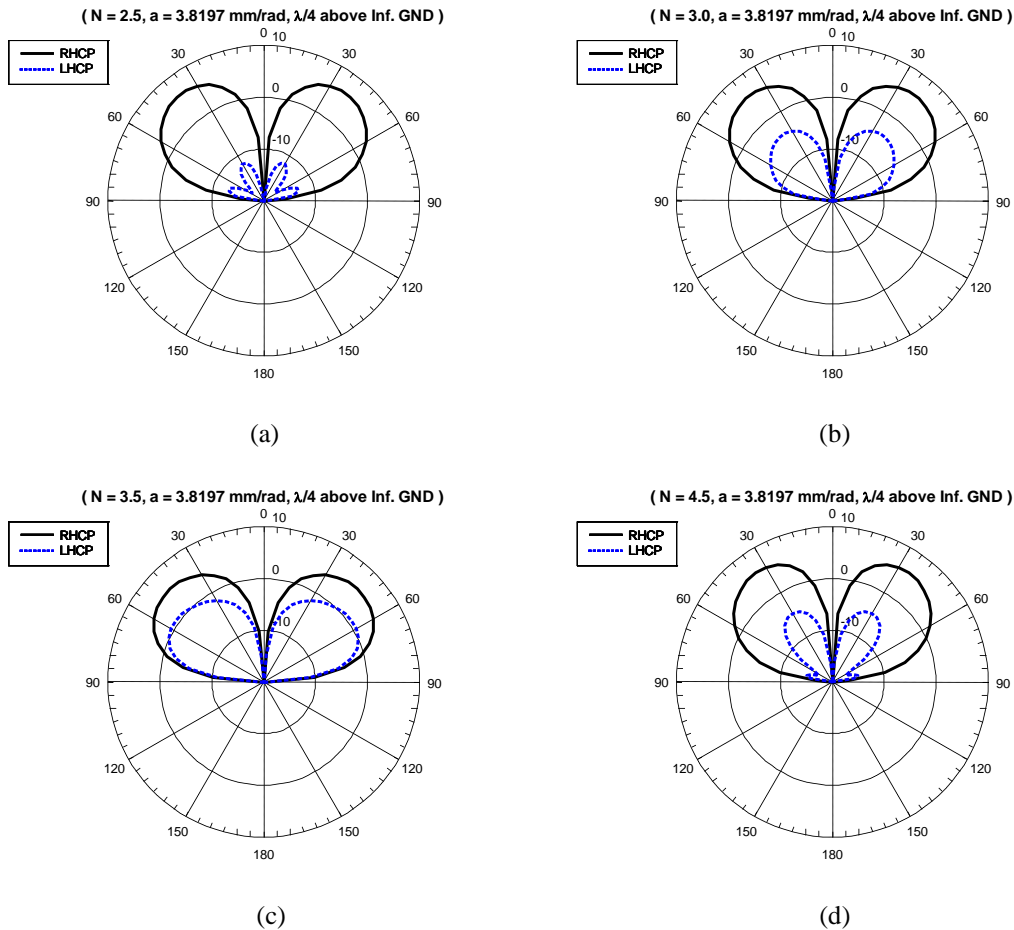
Fig. 3.8. Principal plane CP radiation patterns of the 4-arm spiral antenna λ/4 above infinite GND plane for the second mode with *a*=3.8197mm/rad, (a) N=2.5, (b) N=3.0, (c) N=3.5, and (d) N=4.5.

42

The axial ratios for the second mode are shown in Fig. 3.9. Again, a good axial ratio is observed when N=2.5, as illustrated in Fig. 3.9a. Similar to the first mode, there is less interaction between the antenna and the ground plane for the small value of N.
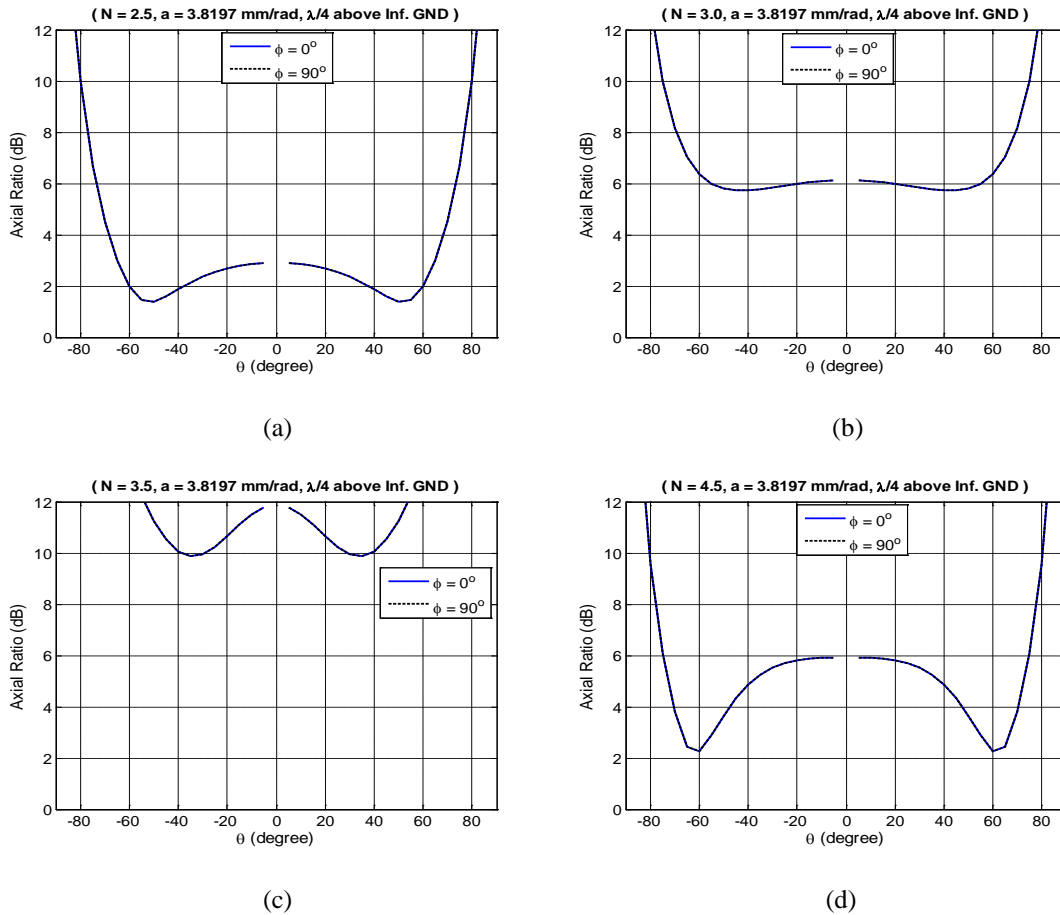
Fig. 3.9. Principal plane axial ratios of the 4-arm spiral antenna λ/4 above infinite GND plane for the second mode with *a*=3.8197mm/rad, (a) N=2.5, (b) N=3.0, (c) N=3.5, and (d) N=4.5.

So far, a four-arm Archimedean spiral antenna placed over an infinite ground plane was studied when the antenna height was λ/4. As shown, even for this distance, which is already large, the spiral mode operation is limited to a specific number of turns. Therefore, an appropriate solution must be found to further reduce the antenna height without deteriorating the axial ratios. This will be discussed in the next section.

43

3.3 Cavity Backed Low Profile Four-Arm Spiral Antenna with Absorber

In this section, a low profile four-arm spiral antenna is proposed. It uses the combination of partially filled absorber material with a small disk as a ground plane. The geometry of the proposed antenna is shown in Figs. 3.10 and 3.11. The novelty of the design is in its simplicity. Conventionally, four-arm spirals have been fed using expensive wideband baluns. This approach is not suitable for the current study. A simpler structure is needed to be fabricated easily. Our design is based on the realization that the sum of all input currents for the first three modes of the four-arm spiral is identical to zero, as shown in Table 2.1, chapter 2. That is, for the first three modes, the four input current phases are out of phase in pairs and the sum adds up to zero. Thus, we can take advantage of the input current cancelation to design an extremely simple balun, with near infinite bandwidth, yet to have a small size. The geometry of the balun is a small disk, much smaller than the wavelength, which can be etched on the opposite side of the dielectric substrate that will support the spiral arms. This disk acts as a ground plane for four coaxial cables that will feed the spiral arms. The size of the disk should be small enough to place it within the central feed region of the spiral, where no spiral conductor is normally etched. Since the sum of the input currents is zero, as long as the disk diameter is very small in wavelength, the currents on its surface and the four connecting feed cables will remain zero. The feed network so designed will not have appreciable effect on the spiral radiation characteristics. In all our designs in this chapter, the inner diameter of the spiral feed region was 21 mm, and the disk diameter was experimentally selected to be 35 mm, to accommodate the connection of four coaxial feed cables.

The purpose of using absorber material is to attenuate unwanted reflections from the spiral arm ends. It is noted that if the cavity is completely filled with absorber, a large percentage of the input power will be absorbed resulting in poor efficiency. To overcome this problem, the partial absorber filled cavity was utilized. As such, placing the absorber only near the outer region of the spiral, with a small overlapping region between the absorbers and the spiral arms, the currents at the spiral arm's end are absorbed, preventing them from reflecting back. The unknown parameters to determine are the width of the overlapping region, and height of the cavity between the spiral and the ground plane. This has been done experimentally over GPS frequency bands. The final parameters are listed in Table 3.5.

Table 3.5. Final parameters of the proposed antenna shown in Fig. 3.10.

AW (Radial size of overlapping region between absorber and spiral)		6.5 mm
h (Absorber height)		29 mm
Spiral constant (*a*)		3.8197 mm/rad
Spiral inner diameter		26 mm
Spiral arm width		3 mm
Dielectric permittivity		2.5
Dielectric thickness		1.58 mm
Number of turns	Ant1	2.5
	Ant2	3.5
	Ant3	4.5
GD (mm^2) (Conducting planar reflector)	Ant1	203.2×203.2
	Ant2	247.65×247.65
	Ant3	298.45×298.45
CD (Diameter of the circular hole in the cavity)	Ant1	133.35 mm
	Ant2	184.15 mm
	Ant3	222.25 mm
BW (Distance between outer edges of spiral and absorber)	Ant1	25.25 mm
	Ant2	18.9 mm
	Ant3	34.775 mm

Three antennas were fabricated with number of turns of:

- N = 2.5 named Ant1,
- N = 3.5 named Ant2,
- N = 4.5 named Ant3,

Their measurement results are given in the next section.
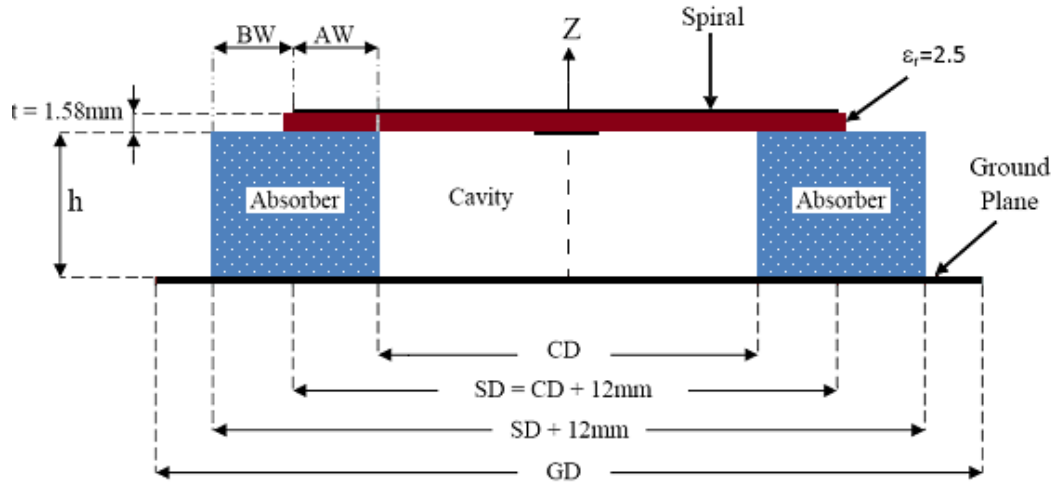
Fig. 3.10. Cross-section view of the proposed four-arm spiral antenna geometry with the details of the spiral substrate, ground plane, and the cavity with its absorbing wall.
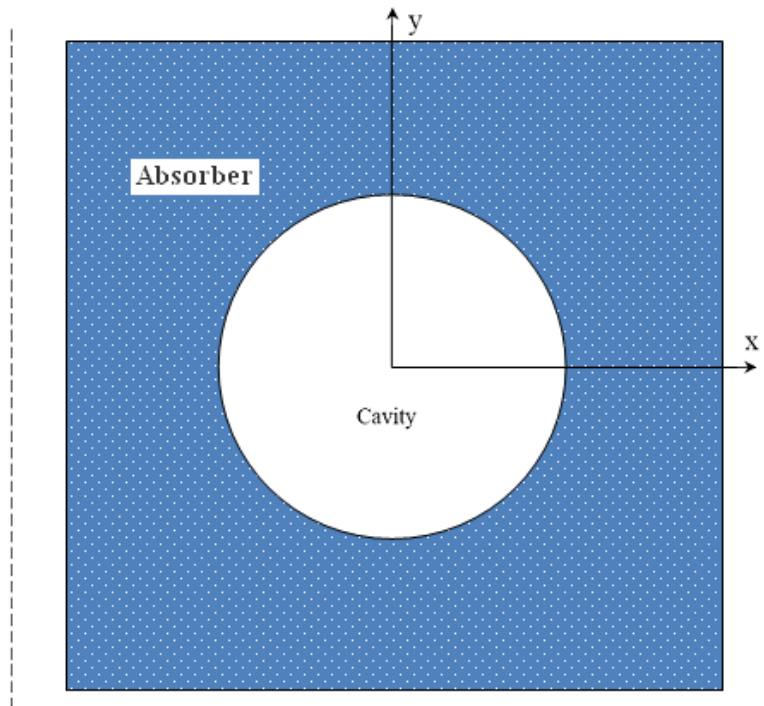
Fig. 3.11. Top view of the absorber ring geometry

3.3.1 Measurement Results [14]

A photograph of the fabricated antennas is shown in Fig. 3.12. All three antenna prototypes, Ant1, Ant2 and Ant3, were experimentally tested using right-handed and left-handed circularly polarized transmitters, for investigating the polarization purity and the gain. The tests were done over all three GPS bands of L1, L2 and L5, covering frequencies from 1.15 GHz to 1.60 GHz. The antennas were tested in the University of Manitoba's 16ft-Compact-Test Range Antenna Laboratory.
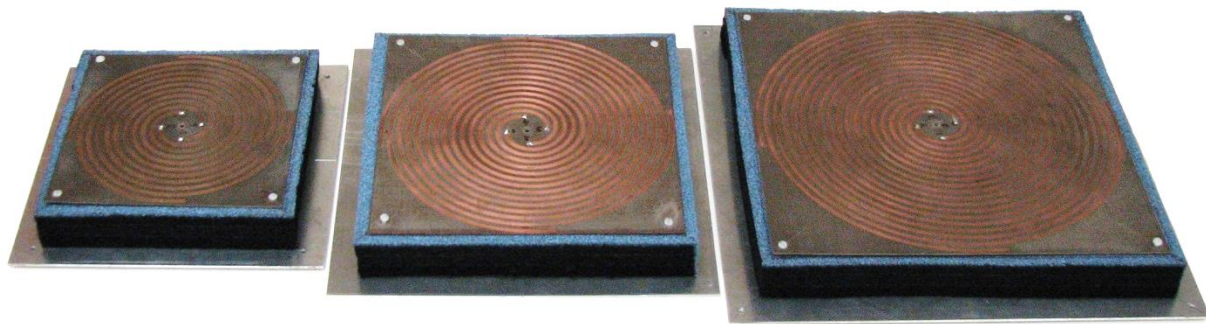
Fig. 3.12. Photograph of three different four-arm spiral antennas. From left to right:
Ant1: 2.5 turns four-arm spiral antenna, diameter = 150 mm.
Ant2: 3.5 turns four-arm spiral antenna, diameter = 200 mm.
Ant3: 4.5 turns four-arm spiral antenna, diameter = 250 mm.

We accumulated large amount of information to enable us assessing the performance of these three antennas under various selected conditions. For brevity, only a summary of the results is provided, which is given in Table 3.6 for both fundamental and second order modes. In this table, the cross-polarization is given as it can be directly measured in practice. However, the cross-polarization of the CP antennas can be easily translated into axial ratios, based on Eqs. 2.11 and 2.12. For instance, a 3dB axial ratio corresponds to -15dB cross-polarization. It is noted that

for the antenna under study, the LHCP represents the cross-polarization. As listed in Table 3.6, the RHCP gain increases as number of turns grows. Better cross-polarization levels, i.e. LHCP components, are obtained in the first mode. To further improve the second mode cross-polarization, a larger antenna is needed.

Table 3.6. Measured co-polar (RHCP) and cross-polar (LHCP) peak gains of modes 1 and 2, *h* = 29 mm, AW = 6.5 mm

	f = 1.17GHz			f = 1.22GHz			f = 1.57GHz		
	Ant1	Ant2	Ant3	Ant1	Ant2	Ant3	Ant1	Ant2	Ant3
Mode 1, Gain(dBic)	3.0	4.64	5.86	5.0	4.5	5.2	4.6	6.4	6.1
Mode 2, Gain(dBic)	-4.4	-1.4	0.8	-3.4	-0.3	1.7	-0.55	2.1	3.8
XP1[*] (dB)	-17.7	-16.54	-13.46	-16.5	-13.3	-14.2	-10	-12.6	-12.5
XP2[**](dB)	-16.4	-10.5	-6.8	-15.4	-8.4	-8.4	-6.15	-8.2	-11.9

[*] XP1(dB) = LHCP(dB)-RHCP(dB) corresponds to mode 1
[**]XP2(dB) = LHCP(dB)-RHCP(dB) corresponds to mode 2

Some examples of the measured RHCP and LHCP patterns of the three antennas, operating at their first and second modes, are provided in Fig. 3.13-3.14, respectively, at the middle GPS frequency band of 1.22 GHz. The corresponding measured results for their second mode operation are also given in Figs. 3.15-3.16, at the same frequency of 1.22GHz. The antenna height is only 29mm, which is about 0.1λ, where λ is the free-space wavelength at f=1.22GHz.
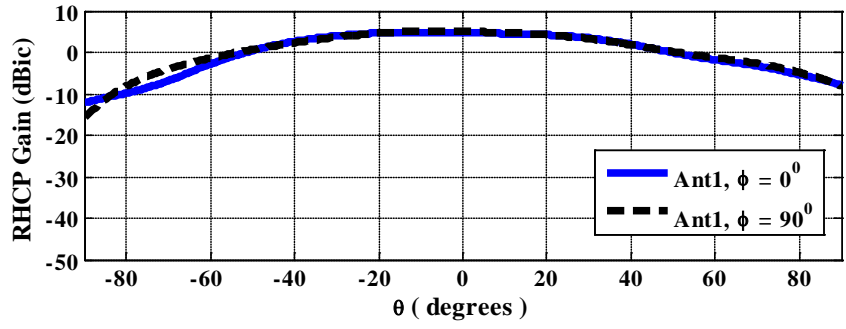
Ant1: N=2.5
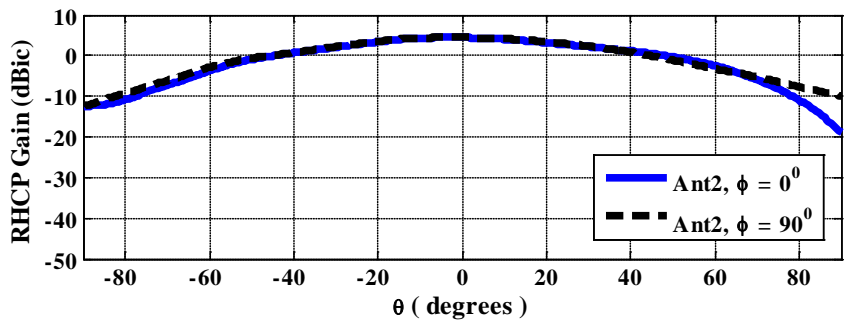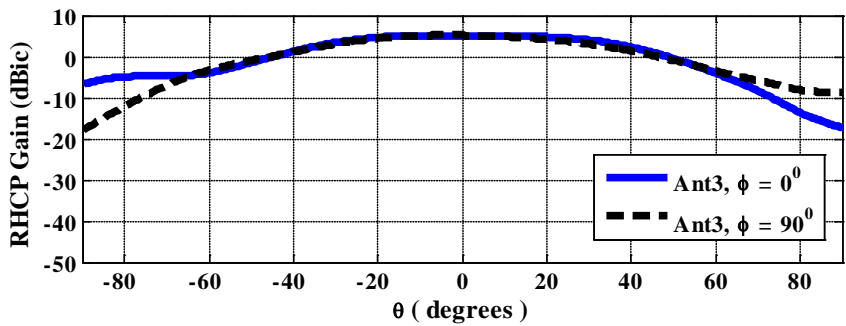
Ant2: N=3.5

Ant3: N=4.5

Fig. 3.13. Mode 1 measured RHCP radiation patterns of small, medium and large four-arm spiral antennas over a cavity with absorbing wall, cavity height 29 mm, at f=1.22GHz.
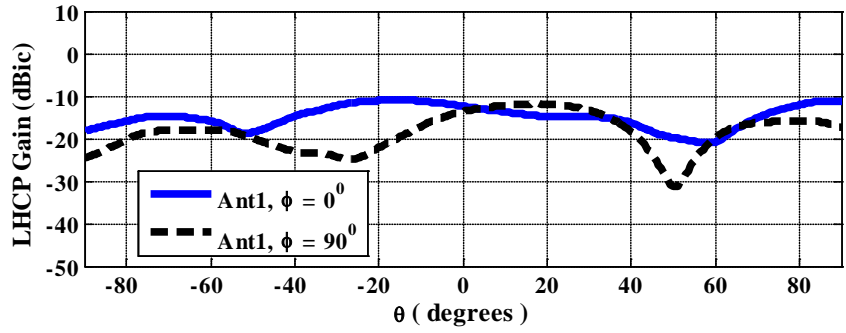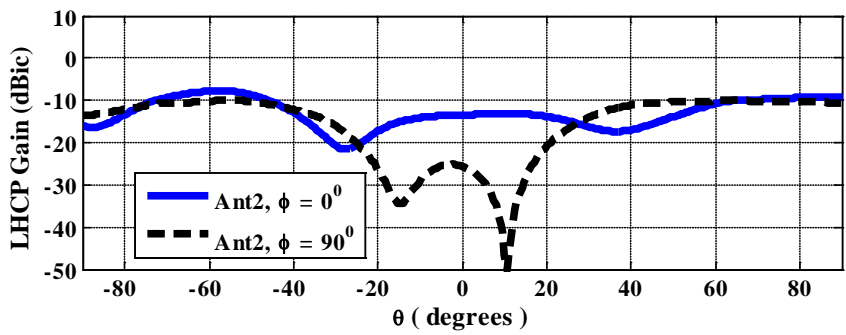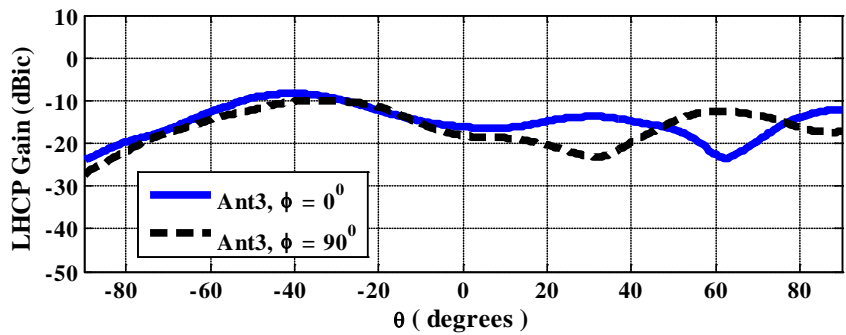
Ant1: N=2.5

Ant2: N=3.5

Ant3: N=4.5

Fig. 3.14. Mode 1 measured LHCP radiation patterns of small, medium and large four-arm spiral antennas over a cavity with absorbing wall, cavity height 29 mm, at f=1.22GHz.
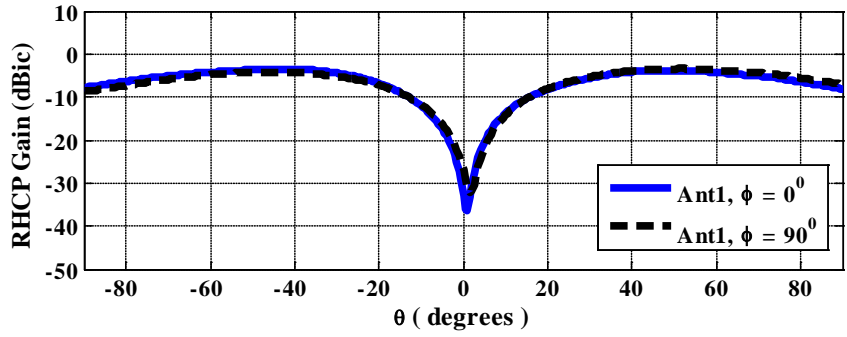
Ant1: N=2.5
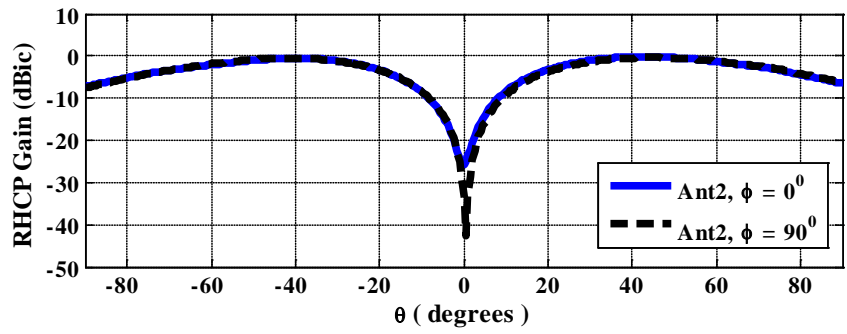
Ant2: N=3.5
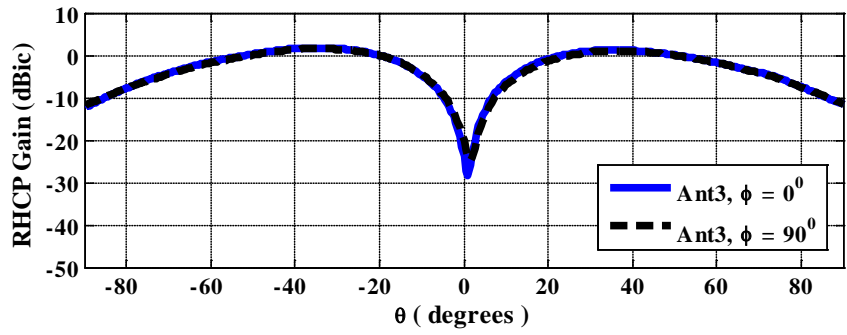
Ant3: N=4.5

Fig. 3.15. Mode 2 measured RHCP radiation patterns of small, medium and large four-arm spiral antennas over a cavity with absorbing wall, cavity height 29 mm, at f=1.22GHz.

Ant1: N=2.5

Ant2: N=3.5

Ant3: N=4.5
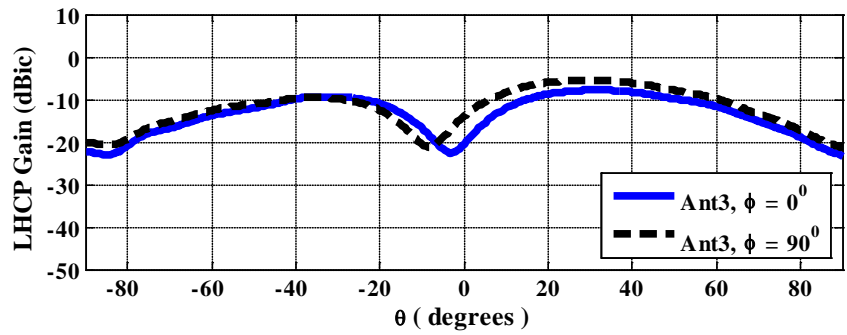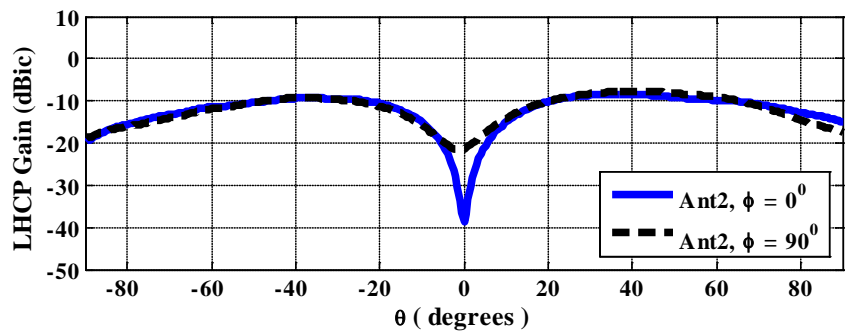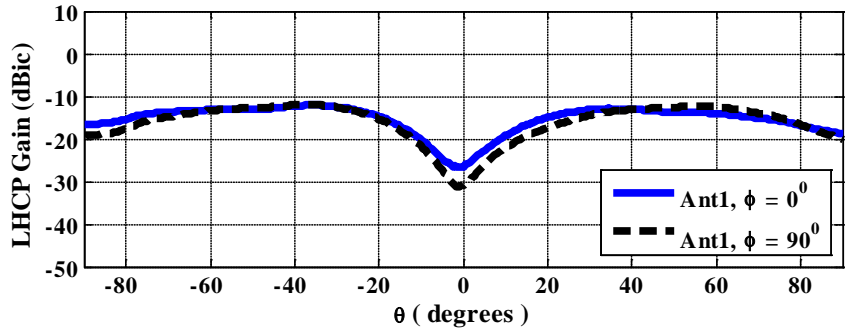
Fig. 3.16. Mode 2 measured LHCP radiation patterns of small, medium and large four-arm spiral antennas over a cavity with absorbing wall, cavity height 29 mm, at f=1.22GHz.

3.3.2 Simulation Results of Cavity Backed Low Profile Four-Arm Spiral Antenna with Absorber

To verify the measurement results, presented in the previous section, we needed to numerically compute the antenna radiation patterns. To do so, precise information of the absorber material used in the experiment is required. Contact was made to Cumming Company, who provides the RF/Microwave absorbing material, to get the closest possible dielectric properties over the GPS frequency bands. Such absorbers have dielectric constant of 1.5 and loss tangent of 0.7. Therefore, we have used Cumming's absorber C-RAM LF-79 layers in the simulation. In this section, the simulated results of the Ant1 with N=2.5 are presented, using the commercial software FEKO [24]. The geometry of the simulated antenna with number of turns equal to 2.5, i.e. Ant1, is illustrated in Fig. 3.17. All geometrical specification accords with the Table 3.5 of the preceding section.
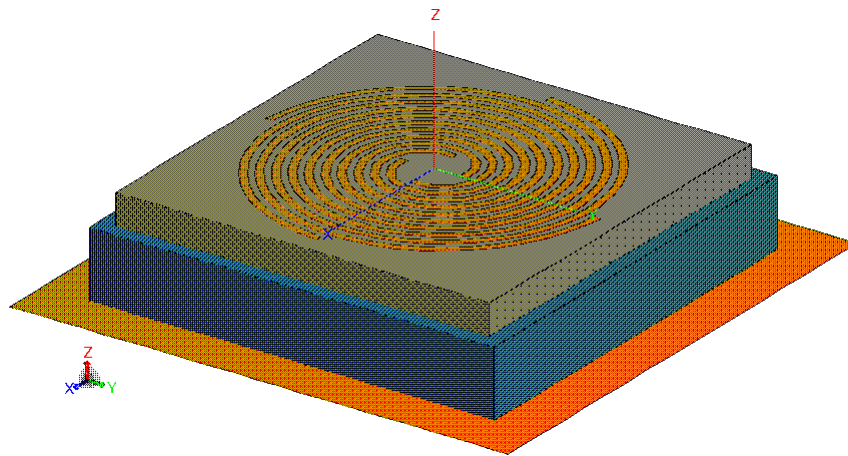
Fig. 3.17. Geometry of the simulated four-arm Archimedean spiral antenna, Ant1 with N=2.5, in FEKO [24]. All parameters match with Table 3.5 for Ant1.

The axial ratios of the antenna shown in Fig. 3.17 are plotted in Fig. 3.18, at both principal planes of $\phi=0^o$ and 90°, at different frequencies ranging from 1.1 to 1.6 GHz, when excited at its first mode. As can be seen, the antenna exhibits excellent CP performance at these frequencies. The corresponding RHCP and LHCP patterns of the antenna are shown in Fig. 3.19, at the frequencies of 1.2GHz and 1.4GHz. The figure shows excellent pattern symmetry with CP performance at both frequencies. At f=1.2GHz, the peak CP gain of the first mode is around 6 dBic, with a cross-polarization level well below -20 dB. Comparing these numbers with the ones given in Table 3.6, at the closest frequency of 1.22 GHz, it is noted that the co-polar components are in excellent agreement. However, there is a slight difference between the measured and simulated cross-polarization levels. This is attributed to several factors; such as the scattering associated with the connecting cables in the measurement setup, different absorber compactness used in practice, as well as the axial ratio of the CP antenna source itself. Nevertheless, both cross-polarization levels are well below -15dB, exhibiting excellent CP performance.

(a)

Far Field

Axial ratio (major/minor) (Phi = 90 deg) - N25_Rogers25
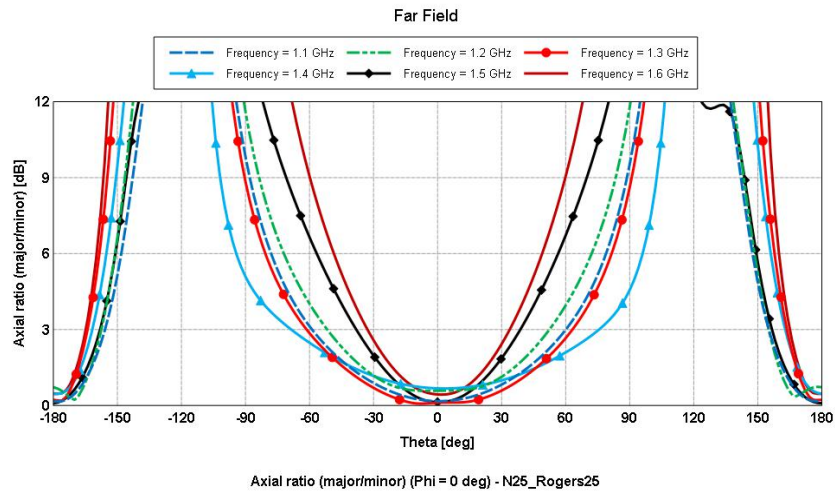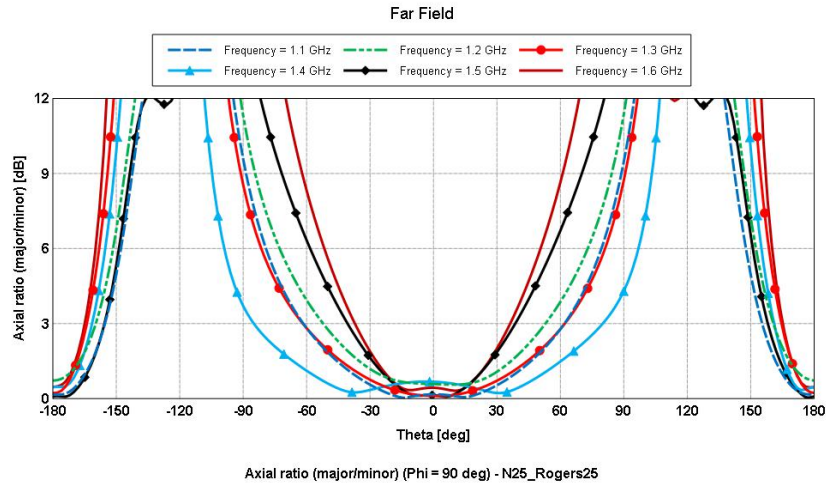
(b)

Fig. 3.18. Simulated axial ratios of the antenna shown in Fig. 3.17 with N=2.5 operating at its first mode in (a) $\phi=0^o$ and (b) $\phi=90^o$ planes.

(a)

(b)

(c)

(d)
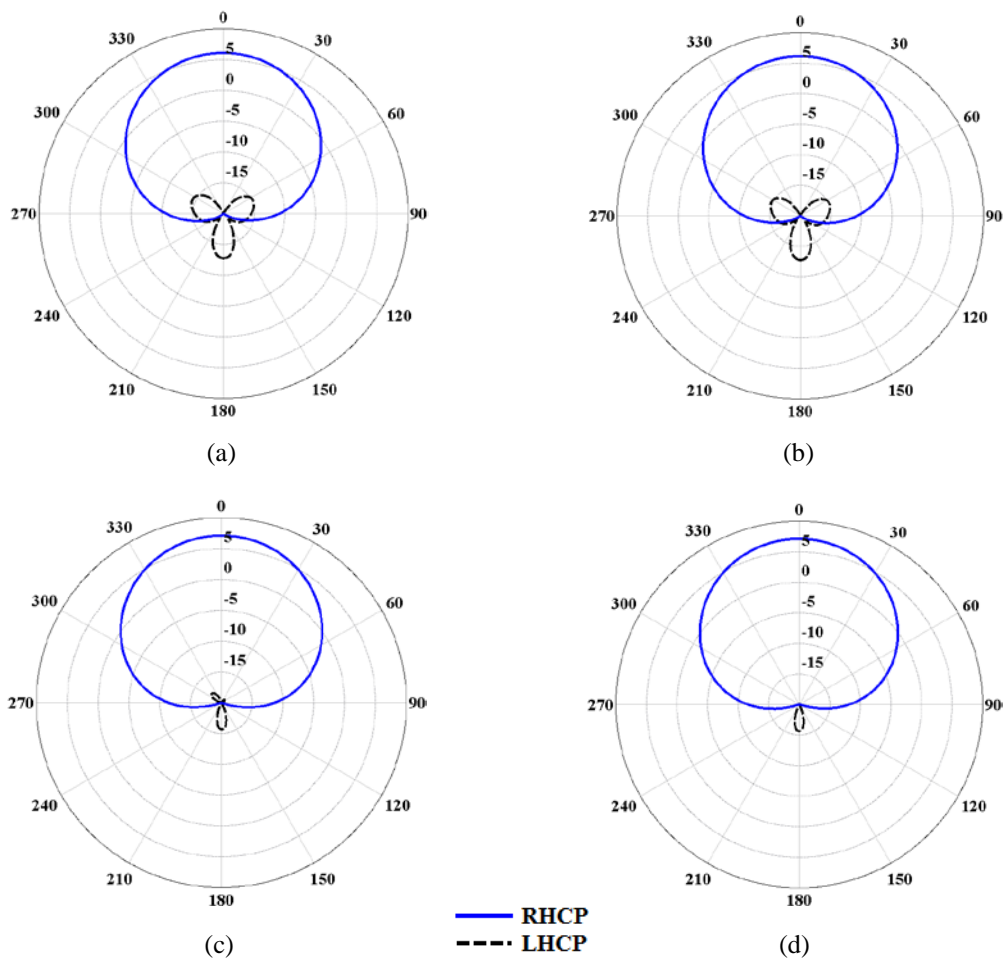
RHCP
LHCP

Fig. 3.19. Simulated RHCP and LHCP patterns of the antenna shown in Fig. 3.17 with N=2.5, operating at the first mode at (a) f=1.2GHz, $\phi=0^o$, (b) f=1.2GHz, $\phi=90^o$ (c) f=1.4GHz, $\phi=0^o$ and (d) f=1.4GHz, $\phi=90^o$ planes.

The corresponding simulated RHCP and LHCP principal patterns of the antenna at the second mode are shown in Fig. 3.20, at the frequencies of 1.2GHz and 1.4GHz. At this mode, the peak gain increases from -3.7 dBic to +0.5 dBic, as frequency changes from 1.2 to 1.4GHz. This is because the spiral active zone at the higher frequency becomes sufficiently large to effectively support the second mode. The cross-polarization level is below -15 dB at the frequency of 1.4GHz. However, it is less than -10dB at f=1.2GHz, which is close to the measured results listed in Table 3.6 at f =1.22 GHz.
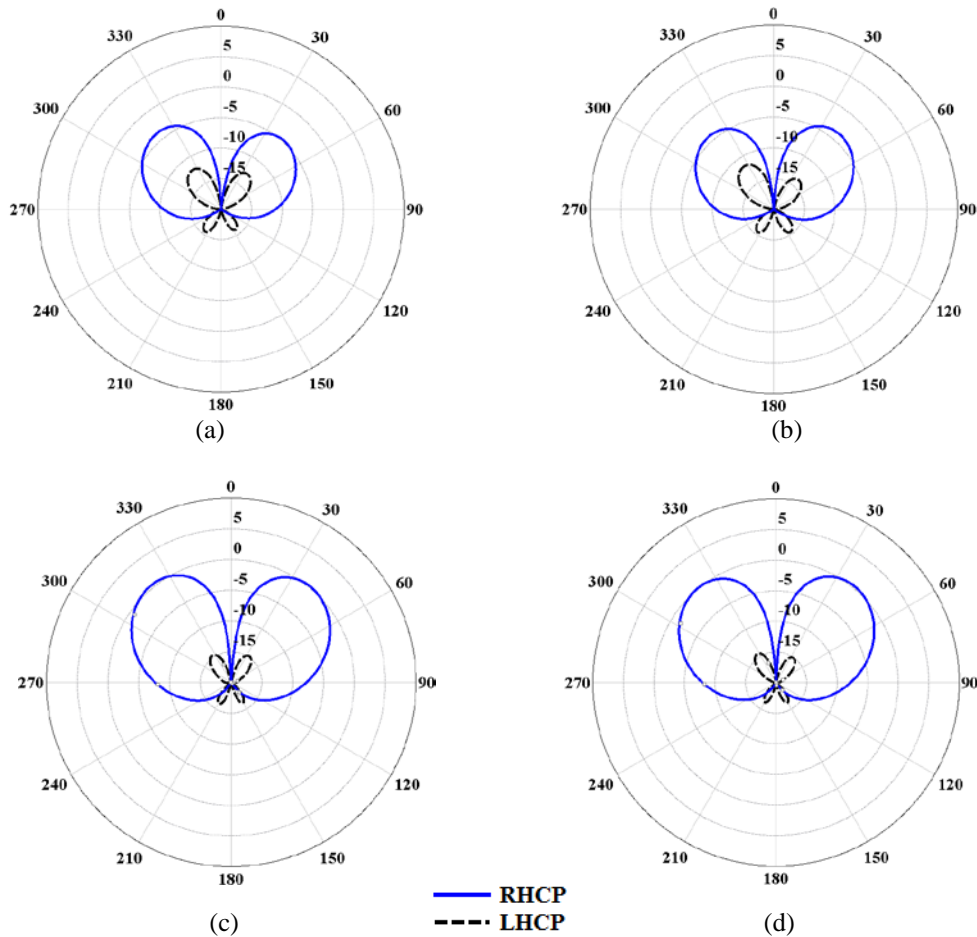
Fig. 3.20. Simulated RHCP and LHCP patterns of the antenna shown in Fig. 3.17 with N=2.5 operating at the second mode at (a) f=1.2GHz, $\phi=0^o$, (b) f=1.2GHz, $\phi=90^o$ (c) f=1.4GHz, $\phi=0^o$ and (d) f=1.4GHz, $\phi=90^o$ planes.

The frequency responses of the antenna shown in Fig. 3.17 are numerically studied in terms of RHCP gain and cross-polarization at both first and second order modes. The results are summarized in Table 3.7 and also compared when the absorber is removed from the antenna structure. It is shown that the absorber material effectively reduces the cross-polarization levels, which is more profound at the second mode than the dominant mode. However, a gain drop of about 2dB is associated with the partially-filled absorber structure at both first and second order modes at the frequency of 1.2GHz.

Table 3.7. Comparison of RHCP gain and cross-polarization of the antenna shown in Fig. 3.17 with N=2.5 with and without absorber at the first and second spiral modes.

Frequency (GHz)	Mode 1				Mode 2			
	Without Absorber		With Absorber		Without Absorber		With Absorber	
	Gain (dBic)	Xpol (dB)	Gain (dBic)	Xpol (dB)	Gain (dBic)	Xpol (dB)	Gain (dBic)	Xpol (dB)
1.2	8.2	-19	6.1	**-21**	-1.7	-0.7	-3.7	**-8.5**
1.3	9.1	-23	7.4	**-25**	1.8	-2.4	-1.3	**-14**
1.4	8.7	-23	7.1	**-25**	4.0	-8.4	+0.5	**-15**

3.4 Summary

In this chapter, a low profile four-arm Archimedean spiral antenna was presented for GPS frequency bands. However, the operating frequency could be easily extended to any frequency band. The antenna axial size reduction was achieved based on the combination of absorbing material and a novel wideband balun. The proposed balun was a small disk printed on the bottom of a thin dielectric slab, on top of which the spiral itself is etched. The novelty of the design was in its simplicity. Three antennas were fabricated and tested in the University of Manitoba Antenna Laboratory. The results for both first and second modes were provided, which successfully verified the idea in practice. Also, some simulation results of the proposed antenna

were presented, which were carried out using the commercial software FEKO. In the simulation, Cumming's absorber C-RAM LF-79 layers were used. The simulations results were matched with the measurement. The overall height of the structure is about 0.1λ; where λ is the free-space wavelength at the frequency of 1.22GHz.

Chapter 4

Performance of Center-Fed Low Profile Circularly Polarized Spiral Antennas with Senses of Polarization along and Opposite to the Direction of Winding

4.1 Introduction

Frequency reuse antennas with higher bit-rate capabilities and enhanced channel capacities are in great demand in a variety of applications, such as multimode Global Positioning Systems (GPS), modern satellite navigation, and radar systems. Two orthogonally polarized waves are employed for each transmit and or receive terminals which increase the link capacity. The orthogonality is normally realized by using two perpendicularly linearly polarized signals or two circularly polarized ones with different senses of polarization. In particular, the utilization of both clockwise and counter clockwise CP signals is necessary in some radio-astronomical applications studying the surrounding atmosphere of planets [44], as well as in direction finding, tracking, and homing. Implementing both such orthogonally polarized waves in a single aperture antenna is highly desirable with the ever-growing technology progress in compact, reconfigurable, and multifunctional antennas. Therefore, the antennas for transmit and receive terminals can be integrated into one, which significantly reduces the system volume and complexity.

The possible polarization diversity scenarios include vertical-horizontal linear polarization and right-hand and left-hand circular polarizations. The latter is of our interest in this thesis. For such polarization selectivity, frequency independent antennas, such as helices and spirals, are best candidates. Since the polarization of these antennas is predominantly dependent on the winding direction of their arms, an opposite sense of polarization can be obtained, when they are fed at outer ends of their arms in helical [45] and spiral [46-47] antennas. However, a simultaneous excitation of both senses of polarization requires complex and bulky feeding networks, which are not easy to incorporate in practice at both terminals. The possibility of generating both senses of CP, with a central feeding method in conical logarithmic spiral antennas, was introduced and experimented in [48-50], and later the radiation mechanism was briefly explained and patented in [51] for bi-directional and planar logarithmic spiral antennas in free space. To the best of our knowledge, the idea has not been extended to low profile and planar Archimedean spiral antennas with unidirectional radiation patterns. Also, the frequency responses have not been elucidated in the above works.

In this chapter, low profile, unidirectional, planar and quasi self-complementary four-arm Archimedean spiral antennas are investigated to be used for polarization diversity applications generating both right-hand and left-hand circularly polarized waves. The proposed antenna is only center-fed and produces both senses of CP waves over the same frequency band, while the spiral winding direction is preset to the right direction. It is backed by a conducting ground plane placed at a distance of 11.5mm from the antenna. First, the radiation mechanism of an N-arm Archimedean spiral antenna is reviewed and mathematically shown that both senses of polarization with broadside

60

patterns can be realized based on the current band theory [4], using incident and reflected travelling currents within a specific size of spirals. To address the frequency responses of the antennas, two different ground plane sizes are studied and shown how the effective frequency bandwidth changes in terms of the antenna size. CP gain, beamwidths, and cross-polarization are presented and discussed. The numerical results are obtained by the full-wave electromagnetic solver, based on the Finite Element method, ANSYS HFSS v.15 [25]. To validate the results in practice, prototypes of the antennas are fabricated and tested at the University of Manitoba's Antenna Laboratory. The simulated and measured results are compared, which exhibit excellent agreement.

4.2   Overview of Radiation Mechanism in Dual-Polarized Spiral Antennas

The radiation from a planar two-arm Archimedean spiral antenna was qualitatively explained in 1960 by Kaiser [4] based on the current band theory. According to this theory, the radiation occurs within an annular ring, over which the currents in the neighboring arms become in-phase. The circumference of the ring is equal to λ, where λ is the free space wavelength, for the first mode. This ring is often referred to as the active region. For an N-arm spiral antenna, there exist N-1 independent modes, whose active regions progressively enlarge in accordance with $m\lambda$, where m is the order of modes. In other words, the spiral must be large enough to allow the radiation of higher order modes. The radiation patterns are broadside for the first mode and become boresight-null shapes for the higher order modes, as the antenna size progressively enlarges based on the current band theory. In general, there are infinite numbers of modes for a given spiral

61

antenna. However, the radiating modes will be limited by the excitation feeding network and size of the spiral under study.

Now, let's consider both incident and reflected travelling currents for an *N*-arm spiral antenna, allowing the propagation of both right-handed (RH) and left-handed (LH) circular polarized waves. Therefore, assuming a time dependence of $e^{j\omega t}$, the total electric field of an *N*-arm spiral can be expressed by Eq. 4.1, where +*m* and –*m* denote right- and left-hand CP of the mth mode, respectively.

$$E(\theta,\phi) = \sum_{m=1}^{N-1} (C_{+m} F_{+m} e^{-jm\phi} + D_{-m} F_{-m} e^{+jm\phi}) \qquad (4.1)$$

wherein *F* represents the radiation functions and *C* and *D* are the weighting amplitude factors of the RHCP and LHCP modes, respectively. The required balanced current excitation array for an *N*-arm spiral antenna, with a winding direction preset to right, can be described by I_m as below, having identical excitation amplitudes:

$$I_m = 1\angle A_m \qquad (4.2)$$

where A_m is the required excitation phase for the mth mode, changing by a $2m\pi/N$ term, and they are expressed as follows, for *N* equal or larger than 4:

$$A_1 = (0 \;,\; -\frac{2\pi}{N} \;,-\frac{4\pi}{N} \;,....,-\frac{2\pi(N-1)}{N}) \qquad (4.3)$$

$$A_2 = (0 \;,\; -\frac{4\pi}{N} \;,-\frac{8\pi}{N} \;,....,-\frac{2\pi(N-2)}{N}) \qquad (4.4)$$

.
.
.

$$A_{N-2} = (0 \;,\; -\frac{2\pi(N-2)}{N}, \;...,\; -\frac{8\pi}{N} \;,-\frac{4\pi}{N} \;) \qquad (4.5)$$

$$A_{N-1} = (0 \;,\; -\frac{2\pi(N-1)}{N} \;, \;...,\; -\frac{4\pi}{N} \;,\; -\frac{2\pi}{N}) \qquad (4.6)$$

It is observed that the spatial arrangements of the feeding excitation array undergo a left-right flip starting at the second element of the arrays expressed by Eqs. 4.3 and 4.6, and 4.4 and 4.5 and etc. This implies that if a center-fed spiral antenna is excited according to the mode N-1, it is possible to generate CP waves, whose sense of polarization is opposite to that of mode 1, provided the spiral circumference is sufficiently smaller than the required active region for the N-1 mode, that is, it must be less than $(N-1)\lambda$. It is worth mentioning that the sense of polarization of mode 1 accords with the winding direction of the spiral. Therefore, both senses of polarization can be realized by a central-feed technique, without the need for extra complex networks at the outer arm ends. The radiation for each sense of polarization is then best explained using incident and reflected currents travelling along the spiral arms. That is, for the excitation given by Eq. 4.3, the currents travels along the arms with negligible attenuation until they reach the active zone for the mode 1 and will be sharply attenuated as they radiate out. As for the excitation expressed by Eq. 4.6, the currents will travel along the arms without radiation, and reflect back from the truncated arms, as the spiral size is not large enough to radiate the mode N-1. The reflected wave resembles that of the spiral, when excited at its outer ends with the phase relationships given by Eq. 4.6. This wave travels backward on a counter wound spiral and generates a LHCP. On such a spiral the excitation by Eq. 4.6 corresponds to the excitation of mode 1 for a LHCP. Thus, the reflected currents continue to travel backward until reaching the active region for the mode 1, as if the antenna would have been fed at the outer ends of the spiral arms. Due to the constraint placed on the spiral circumference less than $(N-1)\lambda$, the radiation of the spiral, fed by Eqs. 4.3 and 4.6, can be mathematically described by,

$$E(\theta,\phi) = C_{+1} F_{+1} e^{-j\phi} + D_{-1} F_{-1} e^{+j\phi} \tag{4.7}$$

Therefore, there exist right- and left-hand CP waves with the radiation similar to the dominant mode. The same analogy can be applied to the excitation of Eqs. 4.4 and 4.5 for clockwise and counter-clockwise CP with the exception that the pattern accords with that of the second mode, i.e. a boresight-null pattern for N equal or larger than five.

For the sake of clarity and completeness, since the antenna under study is a four-arm Archimedean spiral, the required phase shifts for generating broadside radiation patterns with both clockwise and counter-clockwise CP waves are rewritten below as,

$$A_1 = (0 , -90^o , -180^o, -270^o) \tag{4.8}$$

$$A_3 = (0 , -270^o , -180^o, -90^o) \tag{4.9}$$

Since all ports are balanced, the excitation amplitudes of the ports are identical and equal to unity. Therefore, the vectorial excitation forms of Eqs. 4.8 and 4.9 are,

$$I_1 = (1 , -j , -1, +j) \tag{4.10}$$

$$I_3 = (1 , +j , -1, -j) \tag{4.11}$$

In the following sections, the above phase shifts will be used to excite low-profile planar four-arm Archimedean spirals from their inner arm ends to address the antenna properties such as gain, axial ratio, cross-polarization, and beamwidth, over the frequency bandwidth shared by both senses of CP waves.

4.3 Antenna Configuration and Design Overview

Geometry of the proposed antenna is shown in Fig. 4.1. It is a planar center-fed Archimedean four-arm spiral antenna with a counter-clockwise winding direction. It is designed as a quasi-self-complementary structure, whose inner and outer radii are

selected to accommodate the feeding cables and to be large enough to allow incident and reflected travelling currents flow on the arms to excite both RHCP and LHCP of the dominant mode 1, respectively. That is, the circumference of the spiral arms should approximately be less than 3λ, as discussed in the previous section. Since the proposed antenna is backed by a ground plane in a close proximity to the spiral arms, the exact value of the spiral circumference will be less than the 3λ criteria, which will be addressed in the next section. To realize a low-profile structure, the distance between the spiral and the ground plane is numerically investigated to find a reasonably small height, without sacrificing the CP performance of the antenna. After extensive studies, the height is finalized as 11.5mm. Conventionally, a wideband balun is needed to generate balanced spiral modes, which makes the feeding networks more complex. In lieu of such expensive baluns, a small conducting disk, placed underneath the center of the spiral, was proposed in [38-40] for spiral antennas, which acts as a balun. From Eqs. 4.10 and 4.11, it is realized that the sum of all input currents for both modes 1 and 3 is identical to zero. Thus, the concept of the disk, as a balun, is electromagnetically compatible with the proposed four-arm spiral antenna in Fig. 4.1, as long as the disk diameter is very small in wavelength to avoid interacting with the spiral radiating zone.

In the present design, the inner radius of the spiral, which determines the higher frequency end, is set to 4.0 mm to accommodate the connection of four RG174 coaxial cables to feed spiral arms. The disk radius was then numerically finalized to 5.5mm to have minimum interactions with the spiral radiating zones. For the ease of fabrication and assembly, the spiral arms and the disk are etched on the top and bottom layers of a 1.5mm thick dielectric slab, respectively. For mechanical stability, the disk is

65

peripherally shorted to the supporting ground plane through a cylindrical wall, as shown in Fig. 4.1. The effects of the wall were also studied and concluded that it has negligible impact on the spiral radiation patterns. The outer radius of the spiral should be designed such that it is large enough to support the RHCP and LHCP waves, being excited by the incident and reflected currents, respectively. That is, it must be smaller than the active region of the mode 3, which is about 3λ. Due to the presence of the ground plane, this value is numerically found, which is reduced to about 2.2λ for effective excitation of broadside radiation patterns with both senses of polarization, sharing a respectable frequency band as will be explained in the following section.

For a self-complementary four-arm Archimedean spiral structure, the metallization width of the spiral is equal to the spacing between the arms. In Archimedean spiral antennas, the radius change after a 2π rotation is equal to $2\pi a$, as explained in Appendix A, where a is the spiral constant. Hence, the spiral constant is dictated by w, the metallization width, and is determined by the following equation,

$$8w = 2\pi a \quad \Rightarrow \quad a = \frac{4w}{\pi} \tag{4.12}$$

Herein, the metallization width of each arm is selected as 2mm, due to the minimum available width constraint for fabrication and machining. Therefore, the resulting spiral constant is a=2.55 mm/rad, from Eq. 4.12.

(a)   **(b)**
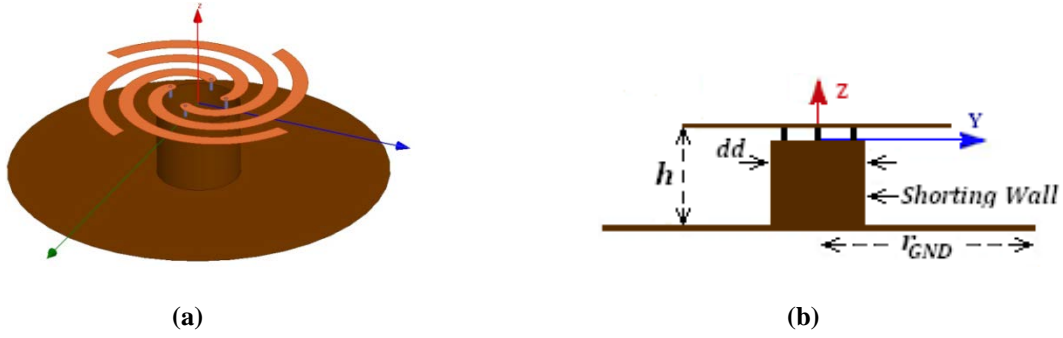
Fig. 4.1. (a) 3-D view and (b) cross-section view of the proposed four-arm Archimedean spiral antenna with spiral constant of *a*=2.55 mm/rad, arm thickness of *w*=2mm, and *h*=11.5mm.

4.4   Performance of Dual-Polarized Four-Arm Archimedean Spiral Antennas

In this section, the performance of the proposed dual-polarized spiral antenna, depicted in Fig. 4.1, is investigated. Numerically generated results are presented for two different ground plane sizes, referred to as case I and case II. The radii of ground planes are equal to 60mm and 37.5mm, for case I and case II, respectively. As mentioned earlier, to maintain a low-profile structure, the distance between the spiral and the ground plane is numerically finalized as 11.5mm to attain the best CP performance and it is fixed throughout our investigations. Moreover, the disk diameter of *dd*=11mm is also numerically finalized to have minimum interactions with the spiral radiating zones. The impacts of the height, disk radius, and spiral constant on the spiral antenna performance will be investigated separately in sections 4.4.4, 4.4.5, and 4.4.6. In this section, the other spiral parameters, except the number of spiral turns, remain unchanged, and they are a=2.55mm/rad and *w*=2mm.

It should be mentioned that the antenna under study is excited according to Eqs. 4.10 and 4.11, to generate the RHCP and LHCP waves, respectively, based on the

mechanism explained in section 4.2. It is demonstrated that the antenna fed by Eq. 4.10 generates the conventional mode 1 broadside radiation patterns, with right-hand CP waves. When it is excited by Eq. 4.11, however, the currents travel along the spiral arms to presumably produce the mode 3 patterns. Because, the arms are truncated well below the required active region of the mode 3, the currents will be reflected back and now progressively phased to efficiently radiate mode 1 patterns. Interestingly, the opposite sense of polarization is obtained since the energy travels inward. The antenna properties such as the CP gain, cross-polarization, purity of CP waves in the form of axial ratios, beamwidths, and radiation patterns are presented here over the frequency range of 1.5-6.2GHz. The common frequency bandwidths, in which the antenna is capable of exciting both RHCP and LHCP waves, will be studied for both cases.

4.4.1   Case I: Ground Plane with a Radius of 60mm

In this case, the radius of the ground plane is 60mm. The RHCP and LHCP boresight gains are plotted in Fig. 4.2 for different numbers of spiral turns from 0.85, 1.0, to 1.05, over the frequency range of 1.5-6.2GHz. As can be seen, the boresight gains for both senses of polarization reach to their maximum values around 4 GHz, and start decreasing thereafter. It should be noted that the LHCP gains in Fig. 4.2.b, remain about 10dBic, up to near the higher end of the frequency range for the spiral number of turns of 0.85.
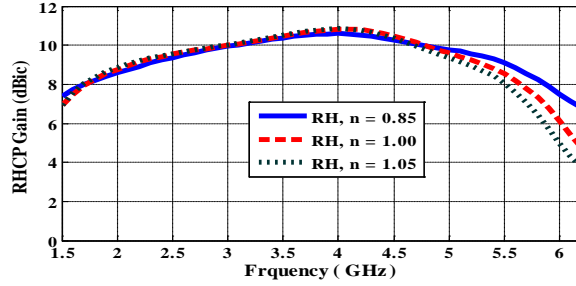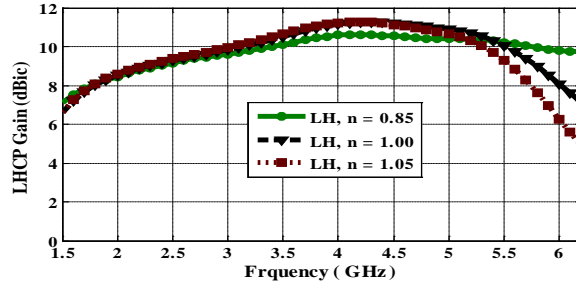
Fig. 4.2. (a) RHCP and (b) LHCP peak gain at the $\theta=0^o$ for the antenna shown in Fig. 4.1, when r_{GND}=60mm, a=2.55 mm/rad, w=2mm, dd=11mm, and h=11.5mm. The RHCP and LHCP waves are excited by Eqs. 4.10 and 4.11, respectively.

The functionality of the CP antenna is not solely based on the CP gain, as the cross-polarization component plays a key role to determine the purity of the CP waves. The corresponding peak cross-polarization values, defined over the forward angular range of $-90^o< \theta <+90^o$, are shown in Fig. 4.3 at the $\phi=45^o$ plane. These values are the difference between the peak cross-polarization and peak gain. As can be seen, there is about 3.5GHz of shared frequency bandwidths, over which both senses of polarization contain cross-polarization less than -15dB, which is equivalent to a 3dB axial ratio. More specifically, the proposed dual-polarized antenna covers frequency ranges of 1.5-5.5GHz, 1.5-5.2GHz, and 1.5-5.0GHz, as the number of spiral turns varies from 0.85, 1.0, to 1.05, respectively. The bandwidth becomes narrower, decreasing from the higher frequency ends, as the number of turns increases. This is because the larger the number of turns, the

69

faster the diameter of the spiral reaches the 3λ zone, at the higher frequency ends, and reduces the reflection of the 3rd mode currents..

For all values of *n*, the spiral number of turns under study, the axial ratios at the boresight direction of $\theta=0^o$ are less than 0.2 dB, over the whole frequency range of interest, as depicted in Fig. 4.4.
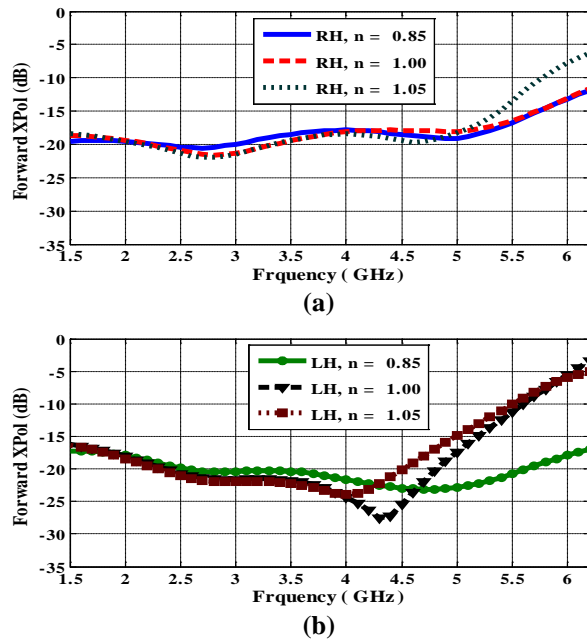
Fig. 4.3. (a) RHCP and (b) LHCP peak cross-polarization at the $\phi=45^o$ plane in the forward region over -90°<θ <+90° for the antenna shown in Fig. 4.1, when r_{GND}=60mm, a=2.55 mm/rad, w=2mm, dd=11mm, and h=11.5mm. The RHCP and LHCP waves are excited by Eqs. 4.10 and 4.11, respectively.

(b)
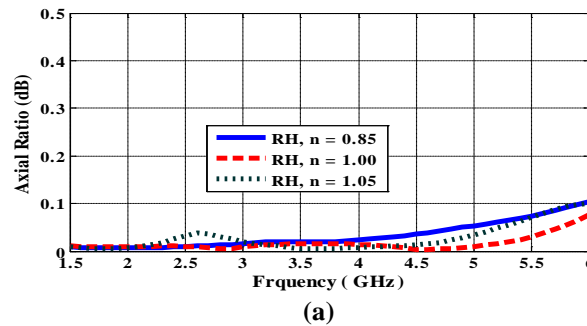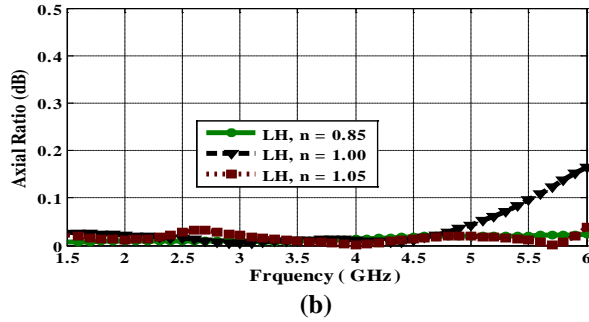
Fig. 4.4. (a) RHCP and (b) LHCP axial ratios at the θ=0° for the antenna shown in Fig. 4.1, when r_{GND}=60mm, a=2.55 mm/rad, w=2mm, dd=11mm, and h=11.5mm. The RHCP and LHCP waves are excited by Eqs. 4.10 and 4.11, respectively.

Due to the symmetrical structure of the proposed antenna, the E- and H-plane radiation patterns of the antenna maintain excellent symmetry as well. That is, they produce equal beamwidths at the principal planes. Since the developed CP antenna has a polarization reconfigurable capability, it is instructive to investigate the beamwidth equality as the sense of polarization alters. The corresponding 3-, 6-, and 10-dB beamwidths are presented in Fig. 4.5, for n=0.85, 1.1, 1.05. As observed, excellent pattern symmetry is obtained for both senses of CP waves, over the frequency range of 1.5 GHz to about 4.5GHz.

(a)
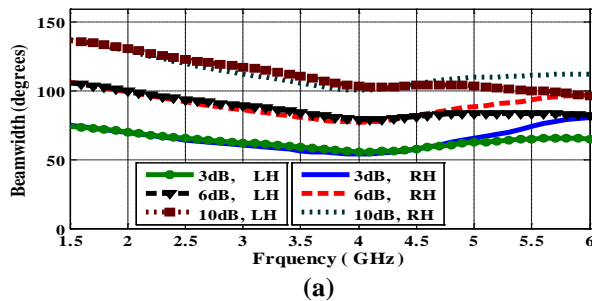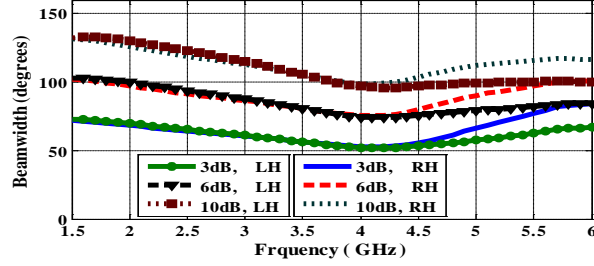
(b)
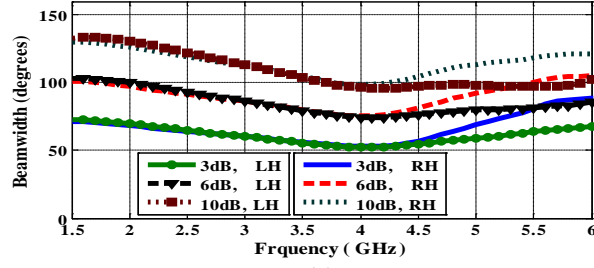
(c)

Fig. 4.5. 3-dB, 6-dB, and 10-dB RHCP-LHCP beamwidths of the antenna shown in Fig. 4.1, when r_{GND}=60mm, *a*=2.55 mm/rad, *w*=2mm, *dd*=11mm, **and** *h*=11.5mm **for different numbers of turn: (a)** *n*=0.85; **(b)** *n*=1; **(c)** *n*=1.05. **The RHCP and LHCP waves are excited by Eqs. 4.10 and 4.11, respectively.**

To show the CP performance of the proposed antenna over the entire angular range in space, the associated radiation patterns of the antenna for both RHCP and LHCP cases are shown in Fig. 4.6, when *n*=1, at three frequencies of 2.0, 3.5, and 5.0GHz. Excellent pattern symmetry and good cross-polarization discrimination are observed. It is noted that the cross-polarization at the θ=180° becomes noticeable, especially at the lower frequency ends as the ground plane size in wavelength becomes smaller. Since this mainly contributes to the cross-talk in the back radiation region, it is not of much concern in practice. Nonetheless, its detrimental impact can be alleviated with a larger ground plane size.
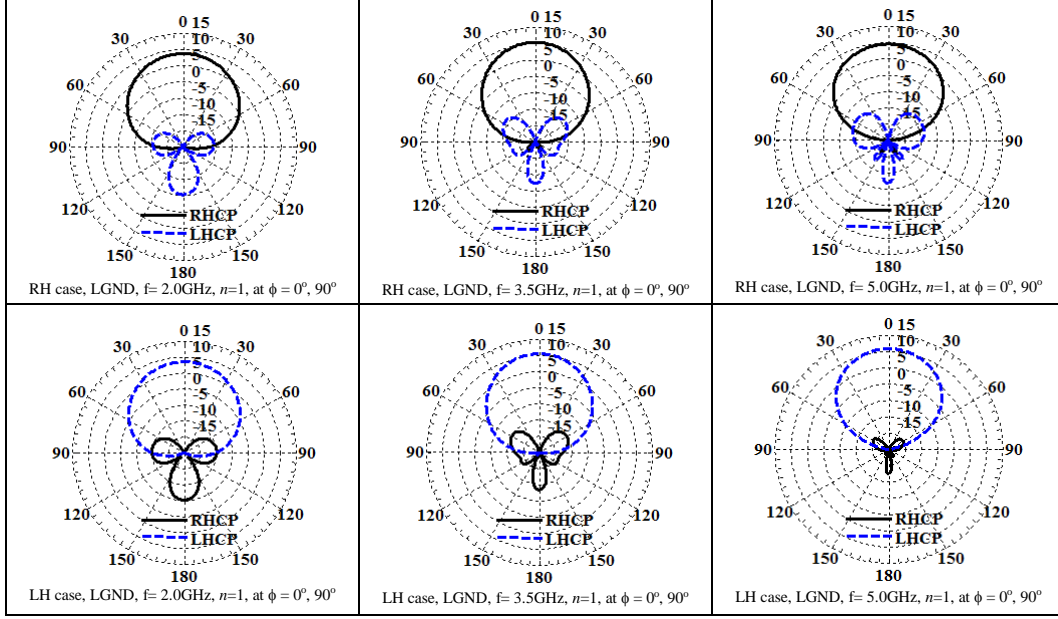
Fig. 4.6. CP radiation patterns of the antenna shown in Fig. 4.1, when r_{GND}=60mm, a=2.55 mm/rad, w=2mm, dd=11mm, and h=11.5mm, when n=1, for both senses of polarization at frequencies of 2.0, 3.5, and 5.0GHz. The RHCP and LHCP waves are excited by Eqs. 4.10 and 4.11, respectively.

4.4.2 Case II: Ground Plane with a Radius of 37.5mm

In this section, the proposed antenna is further investigated when the ground plane radius shrinks to as small as 37.5 mm. Herein, the main objective is to understand how the shared frequency bandwidth, gain, and CP performance are affected by the reduced ground plane size. The RHCP and LHCP peak gains, at the boresight angle, are plotted in Fig. 4.7. Gains of larger than 6dBic are obtained for both senses of polarization at operating frequencies larger than 2.0GHz. For case II, the gains reach to their maximal levels near the higher frequency ends. To better understand the CP performance, the corresponding peak cross-polarization levels in the forward region are given in Fig. 4.8. According to these figures, the common frequency bandwidth, in which the antenna has an axial ratio below 3dB and a respectable CP gain for both senses of polarization, is slightly decreased, as compared to the case I. For better clarity, the shared frequency bandwidths are summarized in Table 4.1 for both cases I and II. The boresight axial ratios

73

are well below 0.2 dB for this case. The results are similar to the ones shown in Fig. 4.4, and they are omitted here for brevity.

(a)

(b)
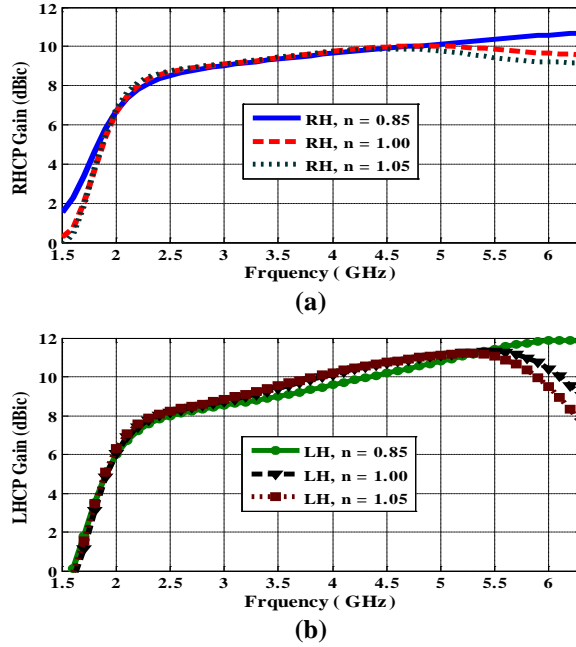
Fig. 4.7. (a) RHCP and (b) LHCP peak gains at the θ=0° for the antenna shown in Fig. 4.1, when r_{GND}=37.5mm, a=2.55 mm/rad, w=2mm, dd=11mm, and h=11.5mm. The RHCP and LHCP waves are excited by Eqs. 4.10 and 4.11, respectively.

(a)

(b)
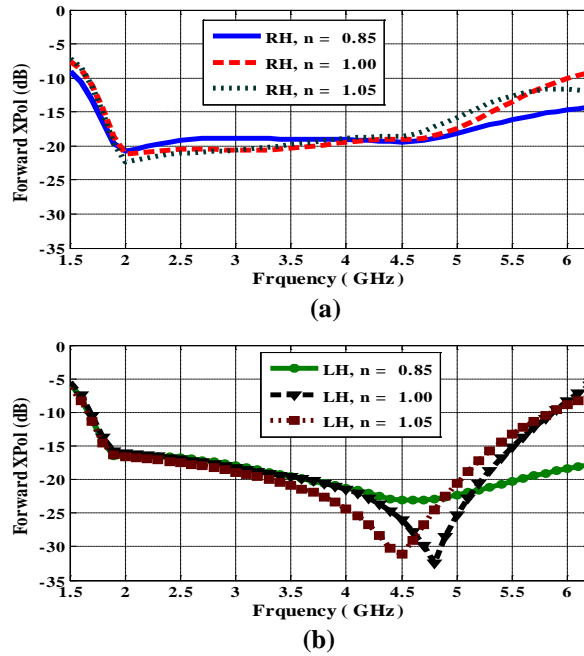
Fig. 4.8. (a) RHCP and (b) LHCP peak cross-polarizations at the ϕ=45° plane in the forward region over -90°<θ<+90° for the antenna shown in Fig. 4.1, when r_{GND}=37.5mm, a=2.55 mm/rad, w=2mm, dd=11mm, and h=11.5mm. The RHCP and LHCP waves are excited by Eqs. 4.10 and 4.11, respectively.

74

	Shared Frequency Bandwidths by both RHCP and LHCP		
	n=0.85	n=1	n=1.05
Case I: r_{GND}=60mm	1.5–5.5GHz	1.5–5.2GHz	1.5–5.0GHz
Case II: r_{GND}=37.5mm	1.8–5.8GHz	1.8–5.3GHz	1.8–5.0GHz

As for the radiation pattern symmetry with regard to the polarization diversity, the 3-, 6-, and 10-dB beamwidths of the antenna are illustrated in Fig. 4.9, for the same values of n as before, i.e. 0.85, 1.0, and 1.05. Good pattern symmetries are attained over the frequency band of nearly 2.5-4.5GHz, which is narrower than its counterpart in case I. This is attributed to the more profound edge effects of the smaller ground plane size on the forward and backward travelling waves responsible for RHCP and LHCP waves.
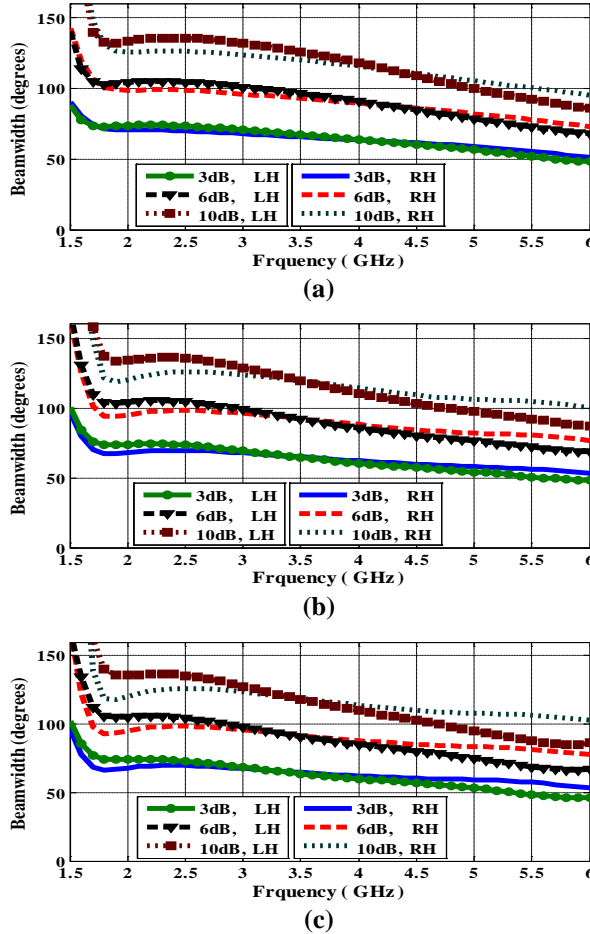
Fig. 4.9. 3-dB, 6-dB, and 10-dB RHCP-LHCP beamwidths of the antenna shown in Fig. 4.1, when r_{GND}=37.5mm, a=2.55 mm/rad, w=2mm, dd=11mm, and h=11.5mm for different numbers of turn: (a) n=0.85; (b) n=1; (c) n=1.05. The RHCP and LHCP waves are excited by Eqs. 4.10 and 4.11, respectively.

Similarly, to illustrate the CP performance of the proposed antenna over the observation angle of $\pm180^{\circ}$, the radiation patterns of the antenna for both RHCP and LHCP cases are shown in Fig. 4.10, when $n=1$, at the three frequencies of 2.0, 3.5, and 5.0GHz. Superior pattern symmetry and good cross-polarization performance are observed. It is noted that the cross-polarization at the $\theta=180^{\circ}$ becomes quite noticeable at the lower frequency ends as the ground plane size in wavelength now becomes even smaller than the previous case I. Had a better back cross-polarized component been required at lower frequencies, a larger ground plane size should have been used, to better suppress the backlobe of the cross-polarization components. However, the use of a smaller ground plane size causes the effective operating frequency to increase. This is because the effective aperture area, which is determined by the ground plane size, becomes smaller and thus the center operating frequency shifts up.
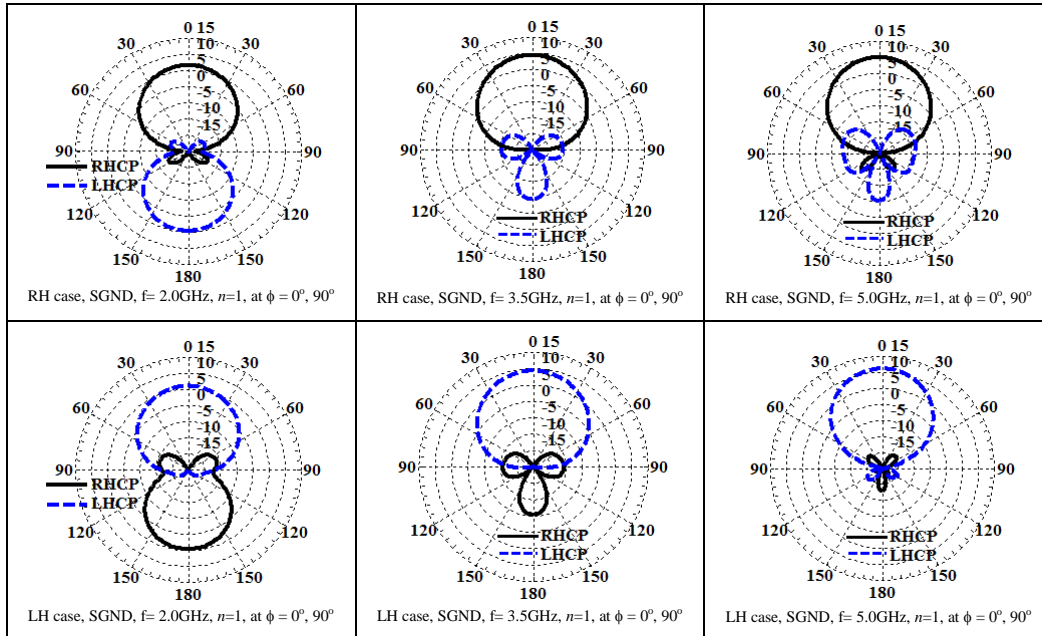
Fig. 4.10. CP radiation patterns of the antenna shown in Fig. 4.1, when r_{GND}=37.5mm, a=2.55mm/rad, w=2mm, dd=11mm, and h=11.5mm, when n=1, for both senses of polarization at frequencies of 2.0, 3.5, and 5.0GHz. The RHCP and LHCP waves are excited by Eqs. 4.10 and 4.11, respectively.

76

4.4.3 Effect of the Ground Plane on the Radiation Zone

From the preceding section, the operating frequency bands of the above cases were numerically determined, as listed in Table 4.1. For an ideal and free-standing spiral, with bidirectional radiation patterns, the radiation zone of dual-polarized broadside pattern is limited between about λ and 3λ. In practice, however, the zone starts earlier around 0.75λ and 2.75λ [51]. The objective of this section is to determine how the ground plane size affects the radiation zone of our proposed dual-polarized spiral antenna with unidirectional patterns. The presence of the ground plane introduces a correction factor, which can be expressed as,

$$(0.75 - CF_1)\lambda_{f_{low}} \leq 2\pi r_{out} \leq (2.75 - CF_3)\lambda_{f_{high}} \tag{4.13}$$

where r_{out} is the outer radius of the spiral, CF_1 and CF_3 are the correction factors of the 1st and 3rd active zones, respectively. $\lambda_{f_{low}}$ and $\lambda_{f_{high}}$ are the wavelengths of the lowest and highest frequencies of operation. From the frequency ranges in Table 4.1, the correction factor of the 3rd mode is directly related to the diameter of the ground plane that is normalized to the largest wavelength of the frequency band. That is,

$$CF_3 \approx \frac{2r_{GND}}{\lambda_{f_{low}}} \tag{4.14}$$

Consequently, the correction factor of the 1st mode is readily determined by scaling Eq. 4.14 by a factor of 3.7, which is the ratio of 2.75/0.75. That is,

$$CF_1 \approx \frac{2r_{GND}}{3.7\lambda_{f_{low}}} \tag{4.15}$$

Therefore, the radiation zone for the dual-polarized spiral antenna backed by a ground plane can be approximately given by the following inequality,

$$(0.75 - \frac{2r_{GND}}{3.7\lambda_{f_{low}}})\lambda_{f_{low}} \leq 2\pi r_{out} \leq (2.75 - \frac{2r_{GND}}{\lambda_{f_{low}}})\lambda_{f_{high}} \qquad (4.16)$$

To examine the validity of above inequality, the radiation zones of the dual-polarized spiral antenna, backed by two ground planes, are given in Table 4.2 and compared with the ones, which are numerically found in sections 4.4.1 and 4.4.2. As can be seen, the estimated radiation zones are very close to the computed ones. Therefore, one can easily follow Eq. 4.16, which satisfactorily includes the impact of the ground plane size to design dual-polarized spiral antennas.

Table 4.2. Comparison of the active zones of the proposed unidirectional spiral antenna obtained by numerical results of Table 4.1 and the estimated inequality of Eq. 4.16 based on the ground plane size, for the number of spiral turn of 1.0.

	Active Zones of the Proposed Dual-Polarized Unidirectional Spiral Antennas	
	From inequality 4.16	from Table 4.1
Case I: r_{GND}=60mm	$0.59\lambda_{f_{low}} < 2\pi r_{out} < 2.15\lambda_{f_{high}}$	$0.63\lambda_{f_{low}} < 2\pi r_{out} < 2.15\lambda_{f_{high}}$
Case II: r_{GND}=37.5mm	$0.63\lambda_{f_{low}} < 2\pi r_{out} < 2.3\lambda_{f_{high}}$	$0.76\lambda_{f_{low}} < 2\pi r_{out} < 2.23\lambda_{f_{high}}$

4.4.4 Effect of the Structure Height on CP Performance

To continue the parametric studies, the distance between the spiral arms and the ground plane, represented by h in Fig. 4.1, is modified and its effects are numerically investigated in this section. As a representative example, the antenna of case II with r_{GND}=37.5mm is selected to conduct the parametric studies on the structure height. Other parameters, such as the spiral metallization width, spiral constant, disk diameter, and number of turns are fixed and they are w=2 mm, a=2.55 mm/rad, dd=11mm, and n=1, respectively. The corresponding RHCP and LHCP gains and cross-polarization levels are shown in Fig. 4.11, for three different heights of 9.5, 11.5, and 13.5mm. As can be seen, changing the structure height by ±2mm from the nominal value of h=11.5mm, as selected

in the preceding sections, has a limited impact on the frequency response of the antenna. In particular, the low-end frequency remains unchanged, based on the -15dB cross-polarization criterion and it is 1.8GHz for all heights. The same trend is observed when h further decreases down to 1.7mm. The corresponding results are shown in Fig. 4.12, for reduced values of h from 7.5mm, 5.5mm, 3.5mm, to 1.7mm. However, it is found that decreasing the antenna height further, e.g. down to 1.7mm, the RHCP and LHCP gains drop considerably at low-end frequencies. This is illustrated in Fig. 4.13 at the frequency of 1.8GHz, which clearly presents a gain drop of at least 4dB as the height decreases from 11.5mm to 1.7mm for both senses of polarization.
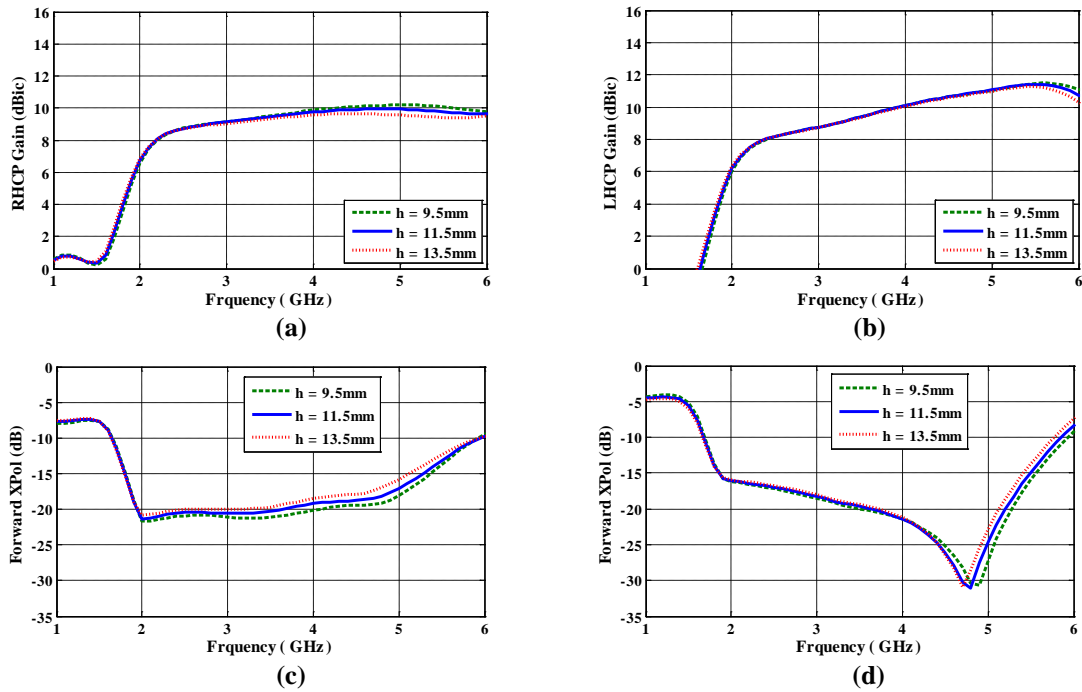
Fig. 4.11. (a) RHCP peak gain, (b) LHCP peak gain, (c) RHCP peak cross-polarization, and (d)LHCP peak cross-polarization of the antenna shown in Fig. 4.1 with n=1, r_{GND}=37.5mm, a=2.55mm/rad, dd=11mm, and w=2mm, for h changing from 9.5mm, 11.5mm, to 13.5mm. The RHCP and LHCP waves are excited by Eqs. 4.10 and 4.11, respectively.
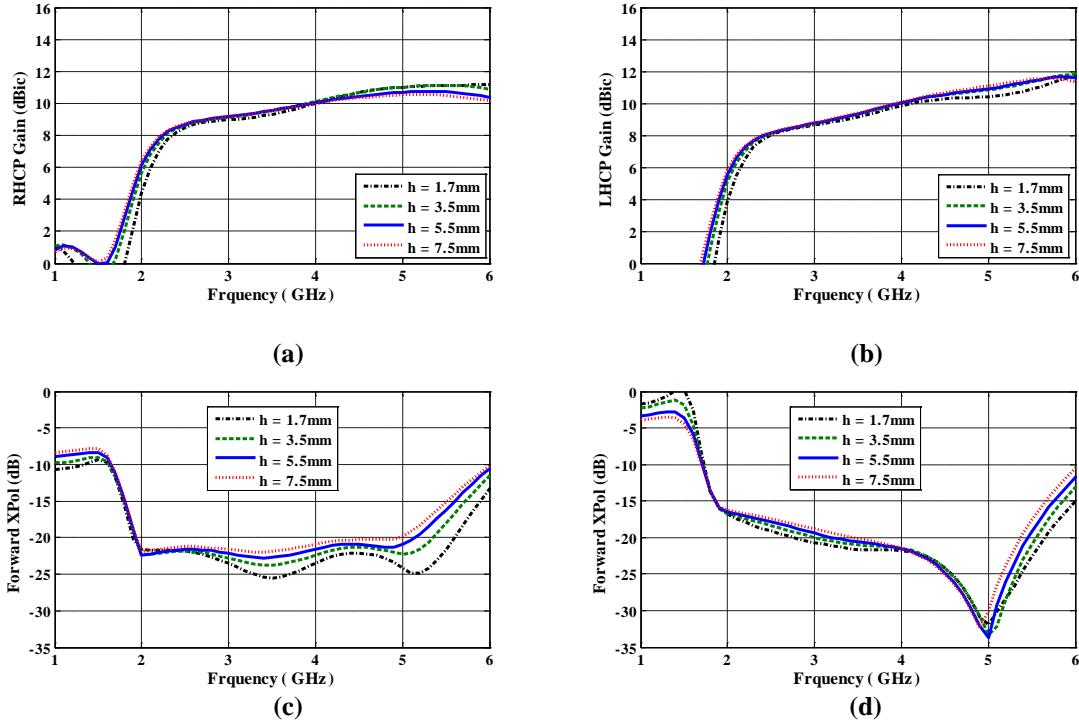
Fig. 4.12. (a) RHCP peak gain, (b) LHCP peak gain, (c) RHCP peak cross-polarization, and (d)LHCP peak cross-polarization of the antenna shown in Fig. 4.1 with *n*=1, *r*$_{GND}$=37.5mm, *a*=2.55mm/rad, *dd*=11mm, and *w*=2mm, for *h* as small as 7.5mm, 5.5mm, 3.5mm, and 1.7mm. The RHCP and LHCP waves are excited by Eqs. 4.10 and 4.11, respectively.
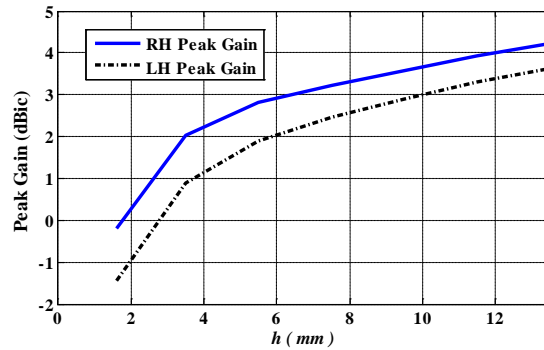
Fig. 4.13. RHCP and LHCP peak gains of the antenna shown in Fig. 4.1 with *n*=1, *r*$_{GND}$=37.5mm, *a*=2.55 mm/rad, *dd*=11mm, and *w*=2mm against *h* at f=1.8GHz. The RHCP and LHCP waves are excited by Eqs. 4.10 and 4.11, respectively.

As for the high-end frequency, even though it seemingly increases with decreasing the antenna height based on the cross-polarization responses in Figs. 4.11c-d and Figs. 4.12c-d, the co-polar CP radiation patterns lose their right-left symmetry and start creating side lobes. These are not desirable, especially when used as feeds in

80

symmetrical reflector antennas. As an example, the resultant RHCP and LHCP radiation patterns of the antenna are shown in Fig. 4.14 at the frequency of 5.3GHz for h=1.7mm and h=3.5mm. That is, the ground plane is very close to the antenna and the strong EM interactions between them deteriorate the radiation pattern symmetry, which is more profound in the RHCP patterns. Therefore, the structure height of 11.5mm ensures a reasonable CP performance of the antenna, free from the aforementioned deleterious impacts. Nonetheless, the proposed dual-polarized spiral antennas with reduced heights can be employed in applications, where limited frequency bands are needed, e.g. in GPS applications.

(a)   **(b)**

(c)   **(d)**
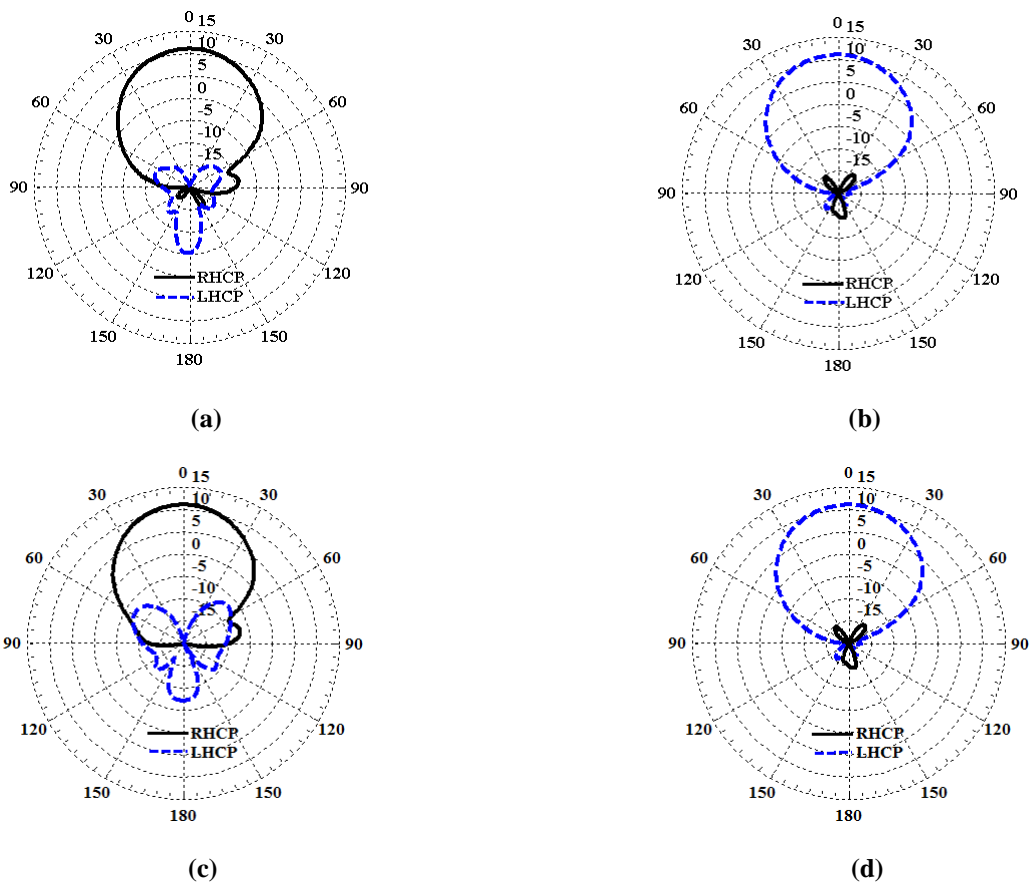
Fig. 4.14. CP radiation patterns of the antenna shown in Fig. 4.1 with n=1, r_{GND}=37.5mm, a=2.55mm/rad, w=2mm, and dd=11mm at f=5.3GHz. The co-polar component is (a) RHCP with h=1.7mm, (b) LHCP with h=1.7mm, (c) RHCP with h=3.5mm, and (d) LHCP with h=3.5mm.

81

4.4.5 Effect of the Disk Diameter on CP Performance

Another parametric study is performed to address the impact of the disk diameter on the CP operation of the antenna. The disk radius should be at least 9mm to accommodate the four RG174 coaxial cables to feed spiral arms, as explained in section 4.3. Thus, the antenna of case II is further investigated, with the disk diameter as the parameter, denoted by *dd* in Fig. 4.1, changing from 9mm, 11, to 13 mm, while other parameters are fixed as w=2 mm, a=2.55 mm/rad, h=11.5mm, and n=1. The RHCP and LHCP gains and cross-polarization levels are illustrated in Fig. 4.15, showing their insensitive frequency behaviors as the disk size enlarges up to 13mm.

(a)

(b)

(c)

(d)
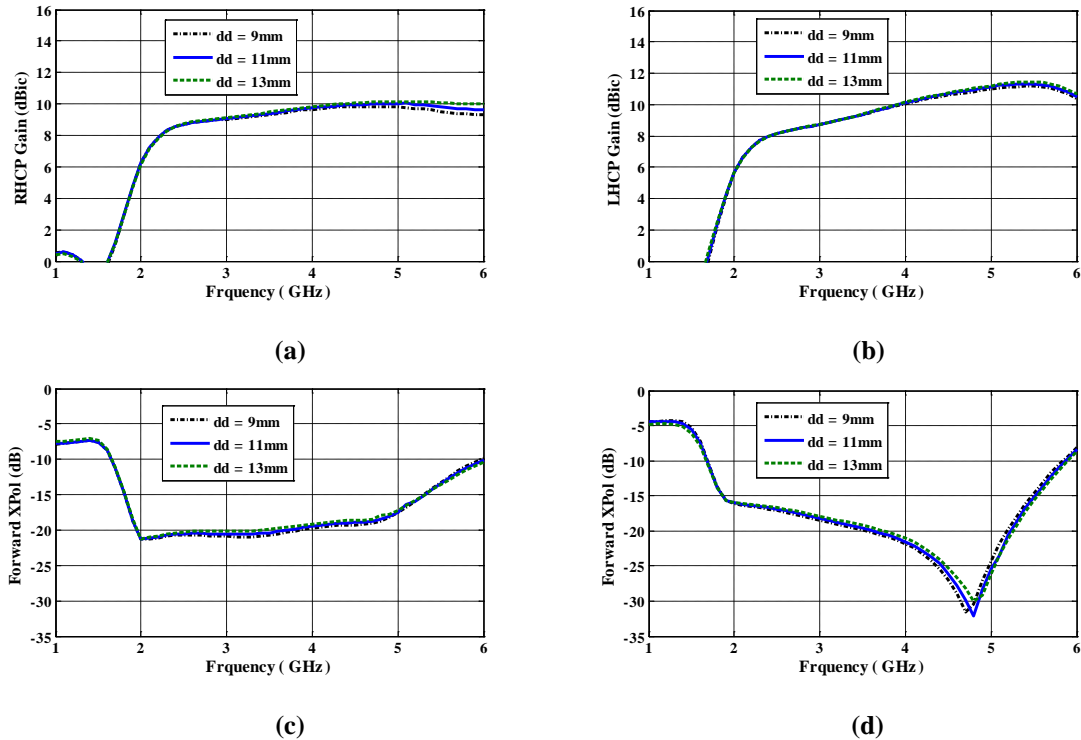
Fig. 4.15. (a) RHCP peak gain, (b) LHCP peak gain, (c) RHCP peak cross-polarization, and (d)LHCP peak cross-polarization of the antenna shown in Fig. 4.1 with n=1, r_{GND}=37.5mm, a=2.55 mm/rad, w=2mm, and h=11.5mm, as disk diameter, *dd*, varies. The RHCP and LHCP waves are excited by Eqs. 4.10 and 4.11, respectively.

It should be mentioned that larger values of the disk size has a detrimental impact on the radiation zones of the antenna. Particularly, the high-end frequency responses are adversely affected. For further clarification, the antenna with a disk size as large as 21mm in diameter is also studied. The corresponding RHCP and LHCP radiation patterns are shown in Fig. 4.16, at the frequency of 5.3GHz, which is the high-end frequency range of the antenna studied in section 4.4.2. For the sake of comparison, the counterpart results are also given in Fig. 4.16 for the nominal value of dd=11mm, at the same frequency of 5.3GHz. It is demonstrated that the cross-polar components become larger and the co-polar ones generate noticeable minor lobes in the unwanted backward region, as the disk diameter increases from 11mm to 21mm.
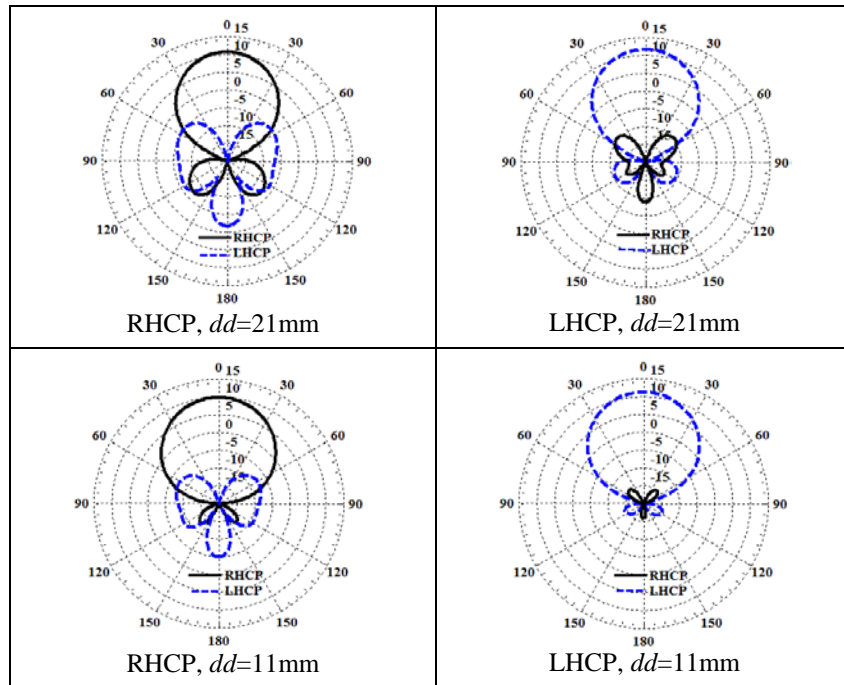
Fig. 4.16. CP radiation patterns of the antenna shown in Fig. 4.1, when r_{GND}=37.5mm, a=2.55 mm/rad, w=2mm, h=11.5mm, and n=1, for both senses of polarization at f= 5.3GHz for dd=11 and 21mm.

4.4.6   Effect of the Spiral Constant on CP Performance

In this section, the impact of the spiral constant on the CP performance of the proposed dual-polarized spiral antenna is numerically investigated. Similar to the previous sections, the antenna of case II is selected to conduct the parametric study, as spiral constant changes from its nominal value of 2.55mm/rad, to 2 and 3mm/rad. The other antenna parameters, except number of turns, are fixed as *w*=2 mm, *h*=11.5mm, and *dd*=11mm. In order to make a valid comparison, the spiral number of turns is changed such that it will keep the spiral outer radius equal to that of the nominal case of *a*=2.55mm/rad and *n*=1. Thus, the spiral number of turns will be 0.85 and 1.3, as *a* changes from 3mm/rad to 2mm/rad, respectively. Since the metallization width is unchanged, the spiral geometry is no longer self-complementary for the aforementioned spiral constants. The resulting RHCP and LHCP gains and cross-polarization levels are plotted in Fig. 4.17. It is observed that the smaller value of spiral constant slightly improves the RHCP and LHCP gain responses at the low-end frequency. On the other hand, the high-end frequency considerably increases as the spiral constant becomes larger, based on gain and cross-polarization responses.

(a)   (b)

84
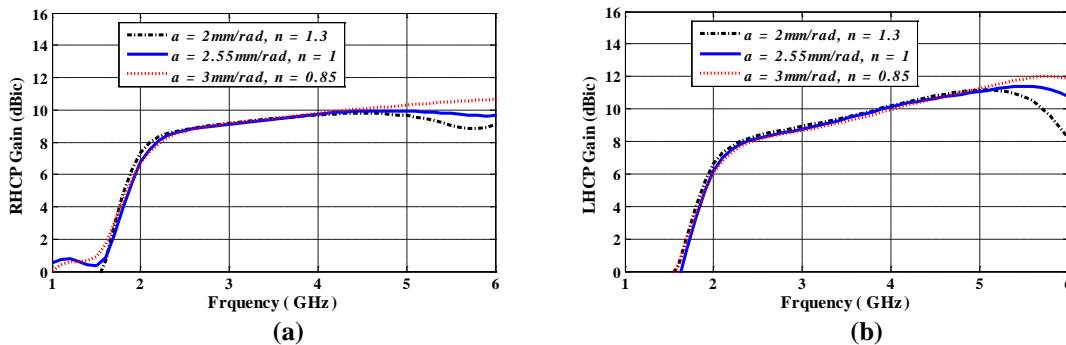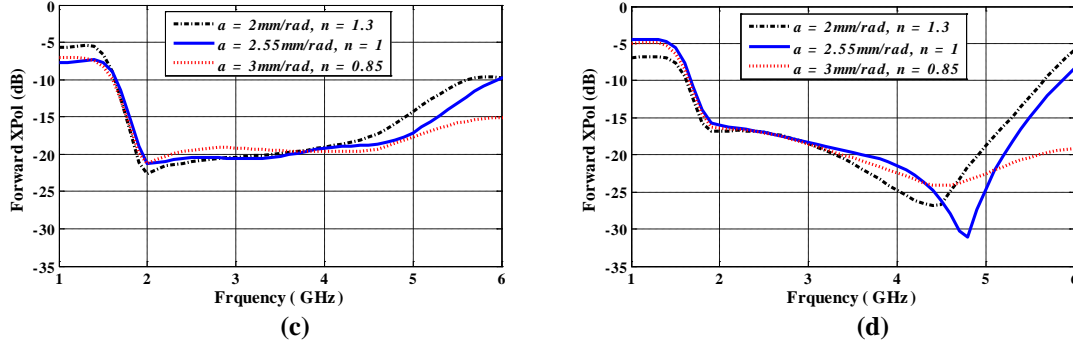
Fig. 4.17. (a) RHCP peak gain, (b) LHCP peak gain, (c) RHCP peak cross-polarization, and (d) LHCP peak cross-polarization of the antenna shown in Fig. 4.1 with r_{GND}=37.5mm, dd=11mm, w=2mm, and h=11.5mm, as spiral constant, a, varies. The RHCP and LHCP waves are excited by Eqs. 4.10 and 4.11, respectively.

4.5   Formulizing the CP Gain of the Proposed Antenna

Further attempts were made to find a simple formula similar to Kraus's [8] to find the CP peak gain of the antennas, based on the numerical results of half-power beamwidths presented in sections 4.4.1 and 4.4.2.   Interestingly enough, it is asymptotically found that the following equation approximately governs the CP gain of the four-arm Archimedean spiral antenna for both senses of polarization,

$$G \cong \frac{36500}{HPBW^E.HPBW^H} \cong \frac{36500}{(HPBW^E)^2} \tag{4.17}$$

wherein $HPBW^E$ and $HPBW^H$ are the 3-dB beamwidths in degrees at the E- and H-planes, respectively. To validate the above equation, the numerical and the computed CP gain according to Eq. 4.17 are plotted and compared in Fig. 4.18, for both RHCP and LHCP of case I with n=1.05, as an example. As can be seen, they are in excellent agreement over the frequency range of 2.0-5.0GHz. To further examine Eq. 4.17, the corresponding results for case II with same value of n are given in Fig. 4.19, exhibiting excellent agreement between the predicted and numerical CP gain, over the slightly reduced frequency range of 2.3-5.0GHz.

85
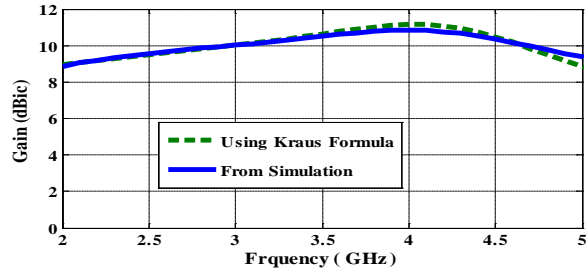
(a)
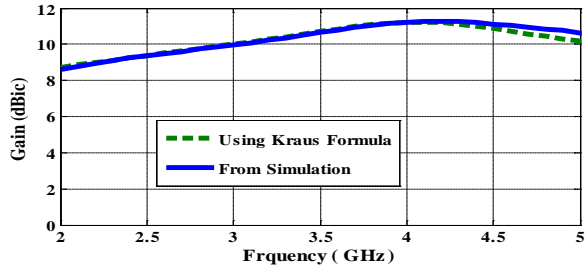
(b)

Fig. 4.18. Predicted by Eq. 4.17 and numerical (a) RHCP and (b) LHCP peak gain at the $\theta=0^o$ for the antenna shown in Fig. 4.1, when r_{GND}=60mm, a=2.55 mm/rad, w=2mm, n=1.05, dd=11mm, and h=11.5mm. The RHCP and LHCP waves are excited by Eqs. 4.10 and 4.11, respectively.
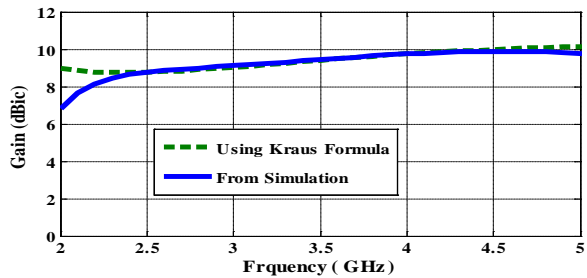
(a)
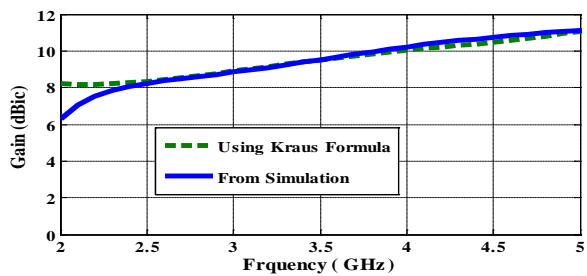
(b)

Fig. 4.19. Predicted by Eq. 4.17 and numerical (a) RHCP and (b) LHCP peak gain at the $\theta=0^o$ for the antenna shown in Fig. 4.1, when r_{GND}=37.5mm, a=2.55 mm/rad, w=2mm, n=1.05, dd=11mm, and h=11.5mm. The RHCP and LHCP waves are excited by Eqs. 4.10 and 4.11, respectively.

4.6 Measurement Results

A photograph of the prototype antenna with a number of turn of 1, $n=1$, is depicted in Fig. 4.20a. For the ease of fabrication, mechanical stability, and avoiding suspending the proposed antenna in air, the spiral arms and the small disk are fabricated on Rogers' RT/duroid® 5880LZ substrate [71], with a thickness of 1.5mm and dielectric constant of 1.96. Since the height of the shorting cylindrical wall is 10mm, which is much larger than the substrate thickness, the effective dielectric constant of the antenna will remain close to that of the air. The supporting ground plane and the shorting cylindrical wall are machined as one piece. The fabricated PCB is then mounted on the machined ground plane with four small plastic screws, as shown in Fig. 4.20a. The resulting antenna is tested in the University of Manitoba's 16ft-Compact-Test Range Antenna Laboratory. The antenna feeding network is also shown in Fig. 4.20b, consisting of three couplers, two 90°s and one 180°. These hybrids are from M/A-COM with part numbers of 2032 and 2031. The spiral arms are then excited according to excitation currents defined by Eqs. 4.10 and 4.11 to generate the RHCP and LHCP signals, respectively.
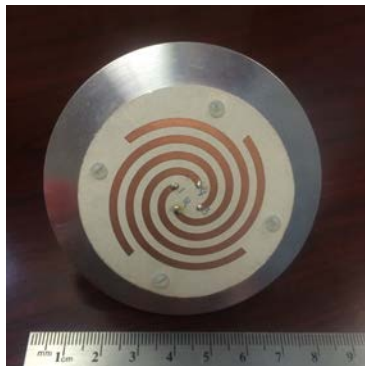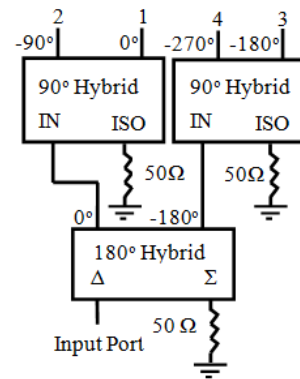
(a)   (b)

Fig. 4.20. (a) Photograph of the prototype center-fed four-arm Archimedean spiral antenna for polarization diversity with $a=$2.55 mm/rad, $w=$2mm, $h=$11.5mm, $dd=$11mm, and $n=$1. (b) Feeding network of the proposed antenna.

The corresponding CP radiation patterns of the antenna, with the ground plane size of case I, are shown in Fig. 4.21. They are compared with their simulated results at the selected operating frequencies 3.0, 3.5, 4.0, and 4.5GHz, at the principal planes of 0° and 90° planes. The measured results satisfactorily agree with the simulated ones. Symmetric co-polar radiations are observed with cross-polarization levels less than -15dB at these frequencies, equivalent to axial ratios smaller than 3dB. It should be mentioned that the comparisons are made over the observation angles of $\pm 120^o$, as Compact Range's rotation angles are limited within this region. The associated measured and simulated radiation patterns of the proposed antenna with the ground plane size of case II with $n=1$ are also plotted in Fig. 4.22, showing excellent match and therefore successfully validating the computed results in practice.

Since the proposed antenna is a four-port network, the active S_{ii} is usually useful to measure the reflected power at the one of the input port. The simulated and measured active S_{11} of the antennas of cases I and II are shown in Figs. 4.23a and 4.23b, which are in good agreement with each other. The spiral number of turns is equal to one, i.e. $n=1$. Considering the -7dB reflection coefficient, which is good enough for most mobile and handheld electronic devices, the proposed antennas have a frequency band from near 3.3 GHz to 5.5 GHz. As presented in Figs. 4.21 and 4.22, both senses of circular polarization are readily guaranteed over the aforementioned frequency range. The passive S_{11} of the antenna is also measured and the results are shown in Fig. 4.23c for both antennas of cases I and II. Passive S_{11} is the reflection coefficient of port 1 when the other ports are terminated with matched loads, while active S_{11} is the reflection coefficient of port 1 when the other ports are excited according to the radiation mode of interest.

Large GND	f=3.0GHz	f=3.5GHz	f=4.0GHz	f=4.5GHz
RHCP $\phi = 0^o$				
RHCP $\phi = 90^o$				
LHCP $\phi = 0^o$				
LHCP $\phi = 90^o$				
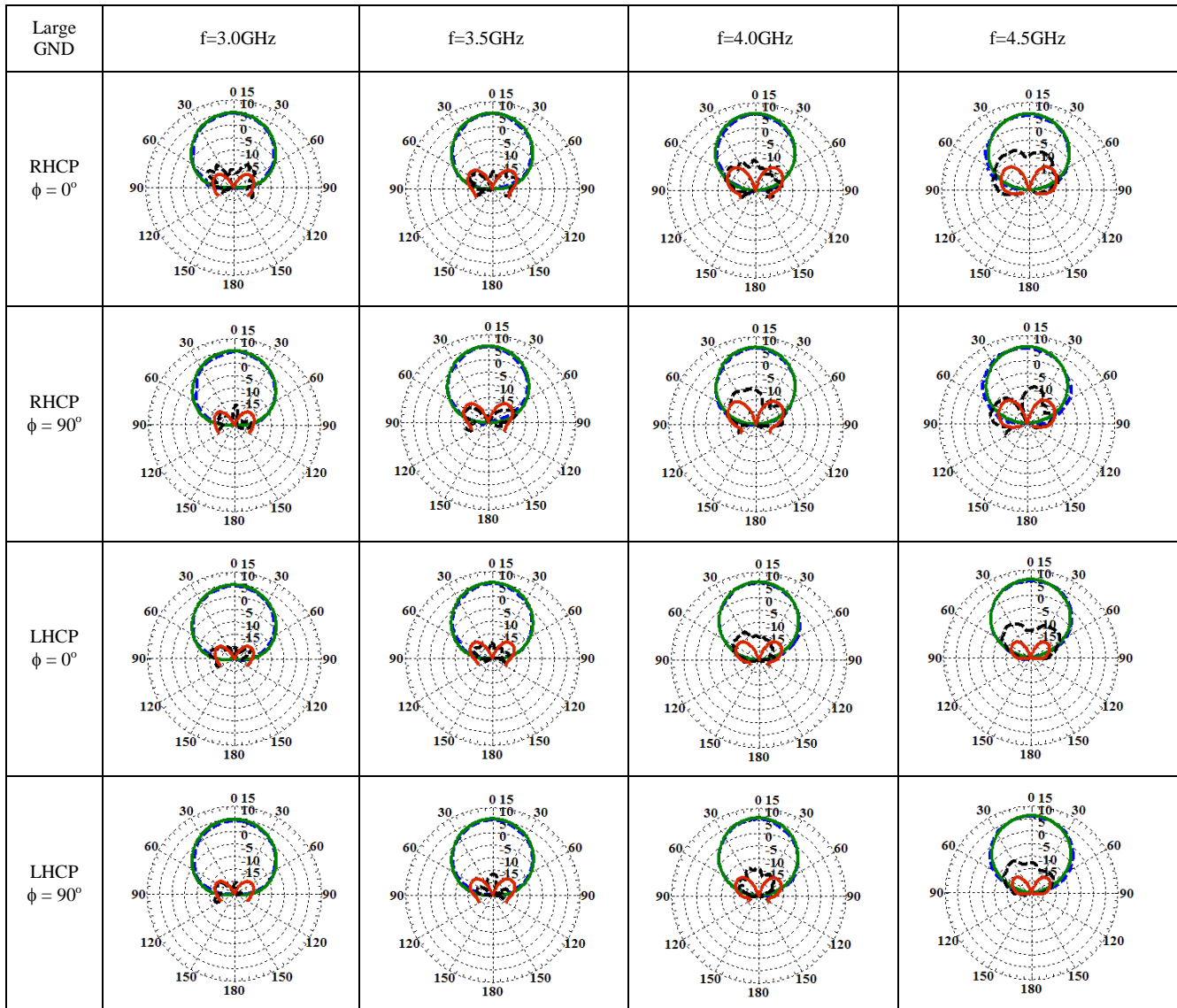
— Simulated Copol — Simulated Xpol

- - - Measured Copol - - - Measured Xpol

Fig. 4.21. Measured and simulated CP radiation patterns of the prototype antenna shown in Fig. 4.20a, backed by a large ground plane of case I with r_{GND}=60mm, a=2.55 mm/rad, w=2mm, h=11.5mm, dd=11mm, and n=1, at operating frequencies of 3.0, 3.5, 4.0, and 4.5GHz.

Small GND	f=3.0GHz	f=3.5GHz	f=4.0GHz	f=4.5GHz
RHCP $\phi = 0^o$				
RHCP $\phi = 90^o$				
LHCP $\phi = 0^o$				
LHCP $\phi = 90^o$				

———— Simulated Copol   ———— Simulated Xpol

– – – Measured Copol   – – – Measured Xpol
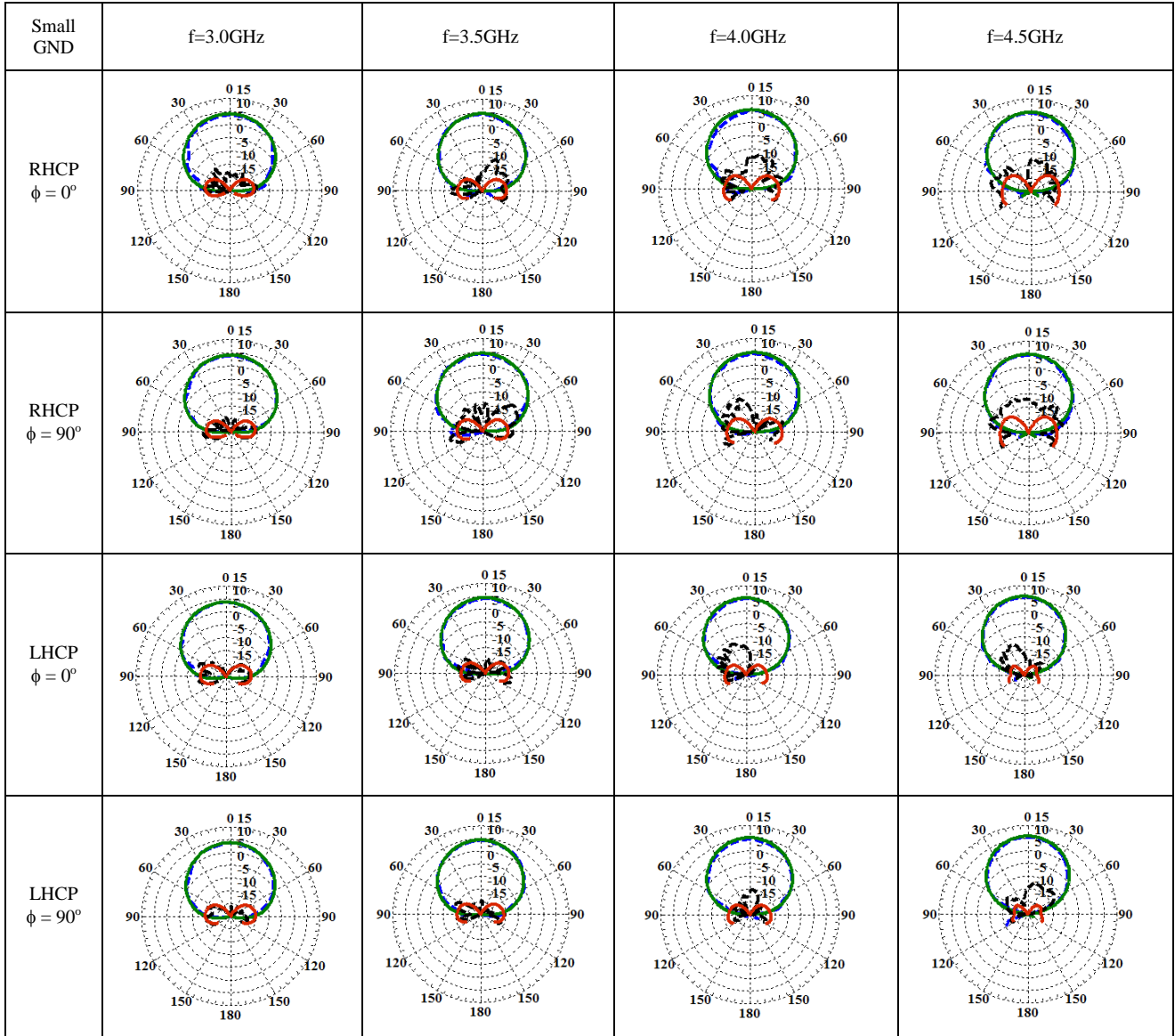
Fig. 4.22. Measured and simulated CP radiation patterns of the prototype antenna shown in Fig. 4.20a, backed by the small ground plane of case II with r_{GND}=37.5mm, a=2.55 mm/rad, w=2mm, h=11.5mm, dd=11mm, and n=1, at operating frequencies of 3.0, 3.5, 4.0, and 4.5GHz.
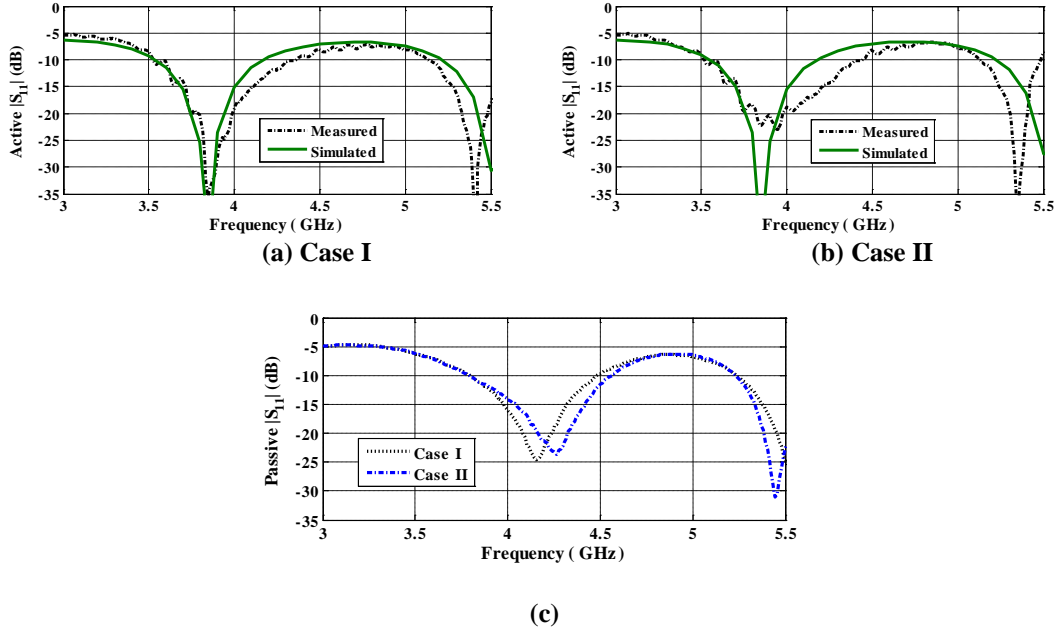
Fig. 4.23. Measured and simulated active S_{11} of the proposed four-arm Archimedean spiral antennas of (a) case I with r_{GND}=60mm, and (b) case II with r_{GND}=37.5mm, (c) measured passive S_{11} of the proposed four-arm Archimedean spiral antennas of case I and case II; n=1.

4.7 Summary

In this chapter, circular polarization diversity of unidirectional, planar, compact, and center-fed four-arm Archimedean spiral antennas was investigated. Their dual-polarized radiation mechanism was explained through incident and reflected currents travelling along the spiral arms. It was shown that when the circumference of the spirals are less than 2.2λ, both RHCL and LHCP waves can be generated by properly exciting the arms with equal amplitudes and phase progression according to the modes 1 and 3 of the spiral, respectively. The antenna with a small conducting disk, acting as a balun, was backed by a ground plane to make unidirectional radiation patterns. Two different ground plane sizes were studied. Parameters such as CP gain, axial ratios, and beamwidths were extensively investigated for both clockwise and counter-clockwise CP waves. The proposed antenna exhibited excellent pattern symmetry for either of the CP polarization.

91

In particular, asymptotic equation was found using Kraus' equation to estimate the peak CP gains of the antenna.

It was demonstrated how one could control the common operating frequency bandwidths, shared by both RHCP and LHCP waves, by varying the ground plane size and the spiral number of turns. The lower end of the common frequency range can be adjusted by the ground plane size. It increased as the ground plane shrank. The upper end of the frequency band can be controlled by adjusting the spiral number of turns such that it decreases as the spiral becomes larger. Two prototype antennas were fabricated and tested in the antenna laboratory. The measured results satisfactorily agreed with the simulated ones, therefore validating the concept of CP polarization diversity of center-fed spiral antennas. Such reconfigurable and multi-functional antennas are excellent candidates for tracking, homing, and direction finding applications.

Chapter 5

Applications of Spiral Antennas as Primary Feeds in Parabolic Reflector Antennas

5.1 Introduction

Symmetrical parabolic reflector antennas, widely used in satellite and high gain wireless communication systems, require an illuminating source, also called a primary feed, with symmetrical radiation pattern properties. Circularly polarized primary feeds are of special interest due to their added feature of being able to easily overcome the detrimental effects of the linear polarization in Faraday rotation, multipath fading loss, and sensitivity to the RX/TX antenna alignments. For wideband wireless applications, spiral and helical antennas are excellent candidates as CP primary feeds. In particular, unidirectional feeds are preferred in order to improve the reflector performance by effectively directing most of the feed energy toward the reflector surface, thus, reducing the spillover power. In addition, polarization diversity adds another incentive to the frequency reuse systems, which result in higher bit-rate data link and improved channel capacity.

The proposed spiral antenna in the previous chapter, showed excellent pattern symmetry with polarization diversity capable of generating both RHCP and LHCP waves, is an excellent CP primary feed for symmetrical parabolic reflector antennas. The proposed feed is geometrically compact, which lessens the reflector shadow region, and is unidirectional in radiation patterns, which confines most of its energy within the

reflector surface. In this chapter, the performance of the proposed spiral antenna is investigated as primary feeds in symmetrical parabolic reflector antennas with circular rims. Different antenna parameters such as gain, cross-polarization, and efficiency are studied for paraboloids, with different focal lengths in both RHCP and LHCP operations. In reflector antenna engineering, these primary feeds are classified as forward feeds. To complete our investigation, backward spiral antennas are also introduced and their performances as rear-radiating feeds are presented for reflector antennas. Backward primary feeds are significantly advantageous in small front-fed reflector antennas, as they can be mounted directly from the apex of the reflector through a single rod. As such, the need for supporting struts is eliminated, resulting in lesser blockage on the reflector aperture. The results presented in this chapter are numerically obtained by a full-wave finite-element bases electromagnetic solver, HFSS V.15 [25].

5.2   Geometry of Parabolic Reflector Antennas

A symmetrical-cut front-fed parabolic reflector antenna with a circular rim is selected in this chapter to conduct our investigation. A parabolic surface is defined by its focal length (F), projected aperture diameter ratio (D), and half-angle ($\theta*$) subtended by the rim, as illustrated in Fig. 5.1. These parameters are expressed by Eq. 5.1 as [6],

$$F/D = \frac{1}{4 \ \tan(\theta*/2)} \tag{5.1}$$

To reduce the computation time, reflector antennas with a projected aperture diameter as small as 20λ are chosen in this chapter, where λ is the wavelength in free space. Different focal lengths are then selected to study the performances of the spiral antennas as primary feeds, which are placed at the focal point of the parabolic reflector
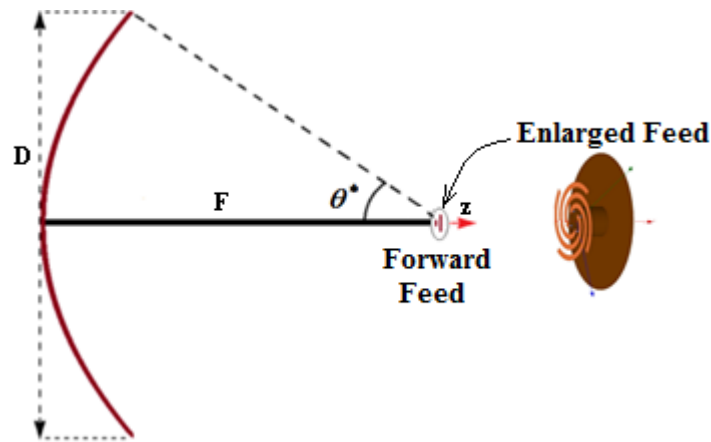
antenna.

Fig. 5.1. Geometry of a parabolic reflector antenna; F, D, and θ* are focal length, aperture diameter, and half-angle subtended by the rim, respectively.

Conventionally, parabolic surfaces are defined by their focal length to the diameter ratios, denoted as F/D in Eq. 5.1, some representative values of which are listed in Table 5.2 along with the corresponding angle θ*. In practice, the most popular F/D value is 0.375 or θ*=67.38°. These curved structures are usually categorized with regard to the depth of the parabola as shallow and deep reflectors. The latter has normally a half-angular opening of larger than 80°, i.e. θ*>80°.

Table 5.1. Parabolic surface specifications with different F/D values

F/D	θ*
2.8575	10.0
1.4178	20.0
0.9330	30.0
0.6869	40.0
0.5361	50.0
0.4330	60.0
0.3750	67.38
0.3570	70.0
0.2979	80.0
0.2500	90.0

One of the important parameters in reflector applications is the feed efficiency, which depends on its primary feed radiation properties. It is a measure of how uniformly the primary feed illuminates the reflector. Thus, it is defined by the ratio of the reflector gain illuminated by the feed under study to that of the ideal feed with uniform radiation. It is expressed by

$$\eta_f = \frac{Gain}{(\pi D / \lambda)^2} \qquad (5.2)$$

wherein the nominator refers to a lossless gain. In terms of co-polar and cross-polar radiation components, the feed efficiency is defined by the following equation [72-73] for a fourfold symmetric feed with RHCP fields,

$$\eta_f = 2\cot^2(\frac{\theta*}{2}) \frac{\left| \int_0^{\theta*} E_R(\theta)\tan(\theta/2)d\theta \right|^2}{\int_0^{\pi} (|E_R(\theta)|^2 + |E_L(\theta)|^2)\sin\theta\, d\theta} \qquad (5.3)$$

wherein E_R and E_L are the electric field components of RHCP and LHCP, respectively. For a LHCP feed, E_R must be simply replaced by E_L in the numerator of Eq. 5.3. The feed efficiency, given by Eq. 5.3, is a product of several sub-efficiency factors such as illumination, spillover, phase, and cross-polarization efficiencies [72-73]. That is,

$$\eta_f = \eta_I \eta_{sp} \eta_{xp} \eta_\phi \qquad (5.4)$$

Where,

Illumination efficiency: $\quad \eta_I = 2\cot^2(\frac{\theta*}{2}) \frac{\left[\int_0^{\theta*} |E_R(\theta)|\tan(\theta/2)d\theta \right]^2}{\int_0^{\theta*} |E_R(\theta)|^2 \sin\theta\, d\theta} \qquad (5.5)$

Spillover efficiency:

$$\eta_{sp} = \frac{\int\limits_{0}^{\theta*}\left(\left|E_R(\theta)\right|^2 + \left|E_L(\theta)\right|^2\right)\sin\theta\,d\theta}{\int\limits_{0}^{\pi}\left(\left|E_R(\theta)\right|^2 + \left|E_L(\theta)\right|^2\right)\sin\theta\,d\theta}$$ (5.6)

Cross-polarization efficiency:

$$\eta_{xp} = \frac{\int\limits_{0}^{\theta*}\left|E_R(\theta)\right|^2\sin\theta\,d\theta}{\int\limits_{0}^{\theta*}\left(\left|E_R(\theta)\right|^2 + \left|E_L(\theta)\right|^2\right)\sin\theta\,d\theta}$$ (5.7)

Phase efficiency:

$$\eta_{\phi} = \frac{\left|\int\limits_{0}^{\theta*}E_R(\theta)\tan(\theta/2)d\theta\right|^2}{\left[\int\limits_{0}^{\theta*}\left|E_R(\theta)\right|\tan(\theta/2)d\theta\right]^2}$$ (5.8)

For feeds with uniform phase patterns and low cross-polarization levels, the illumination and spillover efficiency factors become significantly important in overall efficiency. If a primary feed uniformly illuminates a reflector region, which is confined within an imaginary cone whose apex is the focal point, 100% illumination efficiency is attained. However, outside this cone, practical feeds do spill some of their radiated power, which will be lost in unwanted region. This is called spillover region. Therefore, the maximum efficiency is a compromise between these two factors. In practical applications, the primary feed radiation is tapered at the edge of the cone or the reflector rim by about -10 dB below its maximum axial gain. This will then improve the spillover factor as well as the overall feed efficiency. For example, a feed with 10-dB beamwidths of 135° is well suited for a reflector with $\theta*=67.5^o$ or F/D≈0.375.

It is also worth mentioning that when a reflector antenna is illuminated by a CP source, the sense of the polarization will be changed due to the 180° change in the direction of the propagation of reflected waves. That is, if a RHCP source impinges a reflector antenna, the resulting co-polar component will be LHCP and vice versa.

5.3 Reflector Antennas Illuminated by Forward CP Spiral Feeds with Polarization Diversity

In this section, the proposed four-arm Archimedean spiral antenna, depicted in Fig. 4.1, is placed at the focal point of the reflector antenna shown in Fig. 5.1, as a forward CP primary feed. Both investigated cases of the proposed antenna in the previous chapter are studied, which had two different ground plane sizes to make the antenna unidirectional, namely ground radii of 60mm and 37.5mm. As mentioned earlier, the reflector diameter is fixed at 20λ for the computation convenience, which is carried out by the Integral Equation Module of ANSYS HFSS V.15 [25]. Based on the aperture theory [6], the maximum directivity of a circular aperture with a 20λ diameter, illuminated by a uniform feed, is determined by $(\pi D / \lambda)^2$, which is equal to 35.96 dBi. However, larger reflector sizes may be used, should more directive patterns be required.

Based on the shared frequency bandwidths of the proposed spiral antennas summarized in Table 4.1, a mid-band operating frequency of 3.5GHz is first selected to determine the feed efficiencies versus different F/D ratios. Then, frequency responses are also investigated for the reflector geometry with peak efficiencies. The results are presented in the following two sub-sections.

5.3.1 Primary Feed of Case I with r_{GND}=60mm

In this section, the proposed four-arm Archimedean spiral antenna of case I presented in section 4.4.1 is placed at the focal point of the reflector antenna shown in Fig. 5.1. The spiral antenna is backed by a ground plane with a radius of 60mm, placed

underneath the plane of spiral arms at a distance of 11.5mm. The spiral geometry is defined by the spiral constant of a= 2.55mm/rad and a 2mm metallization arm width. The reflector efficiencies are illustrated in Fig. 5.2 with both RHCP and LHCP secondary radiation patterns, for the spiral number of turns of 0.85 and 1.0 at the frequency of 3.5GHz. They are plotted versus half-angle subtended by the reflector rim θ^* ranging from 10° to 90° (bottom horizontal axis), which corresponds to the F/D ratio of 2.857 to 0.25 (top horizontal axis), respectively. For aforementioned spiral number of turns, the efficiency (η_f) reaches its maximum value of around 75% when θ^*=50° or F/D=0.536 in both RHCP and LHCP operations, which is quite significant. In addition, the feed efficiency is not sensitive to the sense of the CP polarization, when n=1 as depicted in Fig. 5.2b. As for n=0.85, the RHCP performs slightly better than the LHCP towards deep reflectors with small F/D ratios, as shown in Fig. 5.2a.
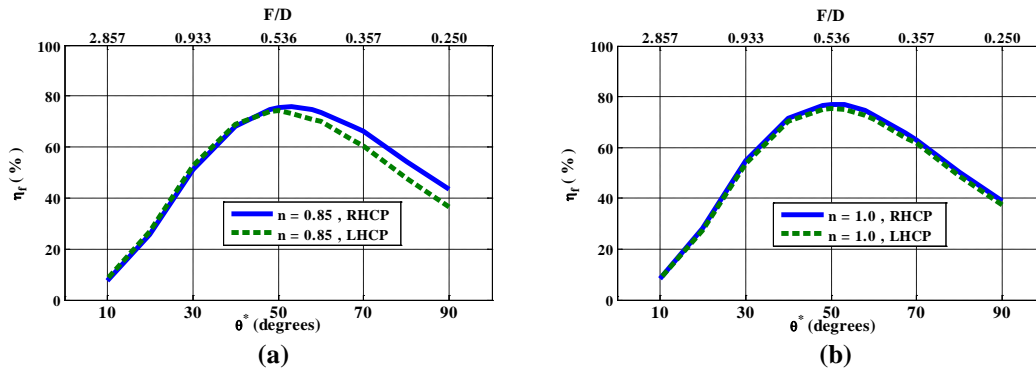
Fig. 5.2. RHCP and LHCP efficiencies of the reflector antenna shown in Fig. 5.1 with D=20λ at f=3.5GHz versus different F/D ratios, when illuminated by the proposed spiral antenna of case I with r_{GND}=60mm, a=2.55 mm/rad, w=2mm, and h=11.5mm with number of spiral turns of (a) n=0.85 and (b) n=1. Top and bottom horizontal axes show subtended half-angle θ* and the corresponding F/D, respectively.

Based on the results of Fig. 5.2, the F/D ratio of 0.536, at which maximum feed efficiency is achieved, is selected to further investigate the frequency response of the reflector antenna under investigation over the range of 2.0-5.5GHz, in terms of the

boresight gain, cross-polarization, and radiation patterns. The spiral number of turn of $n=1$ is chosen to conduct the frequency responses. The boresight CP gain is illustrated in Fig. 5.3 for both senses of polarization. As observed, the reflector gain is stable over the frequency range of interest for both RHCP and LHCP fields. The corresponding efficiencies are given in Fig. 5.4, showing maximum efficiencies of about 80% and 75% at f=4.75GHz and f= 3.5GHz, for RHCP and LHCP fields, respectively. Average efficiencies of about 75% and 72.5% are realized for RHCP and LHCP waves, respectively, over the entire frequency range of 2.0-5.5GHz, which is quite significant.
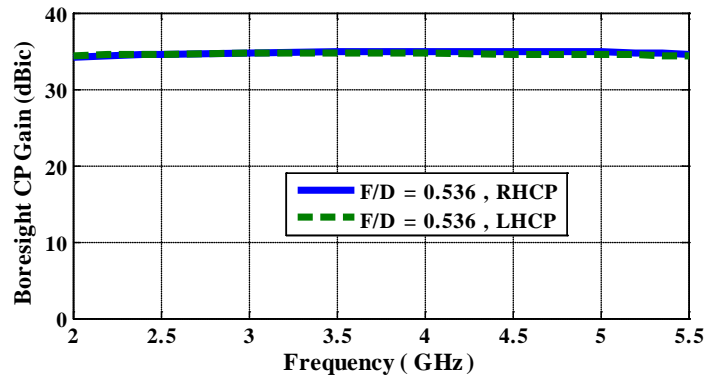
Fig. 5.3. Frequency response of the RHCP and LHCP boresight gains of the reflector antenna shown in Fig. 5.1 with D=20λ and F/D=0.536, when illuminated by the proposed spiral antenna of case I with r_{GND}=60mm, a=2.55 mm/rad, w=2mm, h=11.5mm, and n=1.
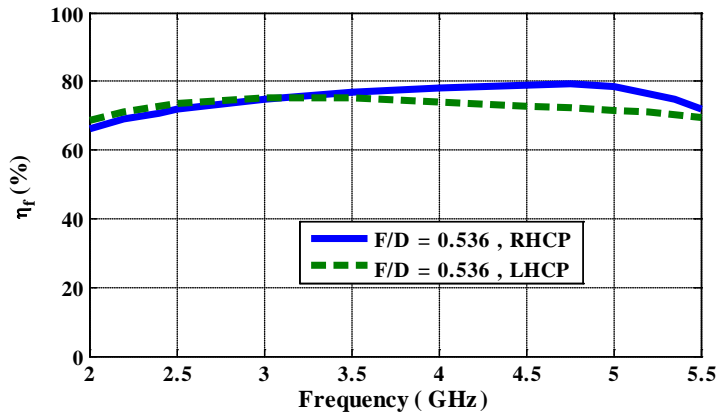
Fig. 5.4. Frequency response of the RHCP and LHCP efficiencies of the reflector antenna shown in Fig. 5.1 with D=20λ and F/D=0.536, when illuminated by the proposed spiral antenna of case I with r_{GND}=60mm, a=2.55 mm/rad, w=2mm, h=11.5mm, and n=1.

100

It is instructive to study the frequency response of the peak cross-polarization of the reflector antennas as well, for the selected F/D=0.536 and n=1. The results are shown in Fig. 5.5, in which the peak cross-polarization levels are given for RHCP and LHCP fields, at both principal and diagonal planes. As can be seen, the peak cross-polarization levels are below -23dB, up to 5GHz. Such excellent cross-talk discrimination makes the resulting antenna a well suited candidate for frequency reuse wireless applications.

(a)   (b)
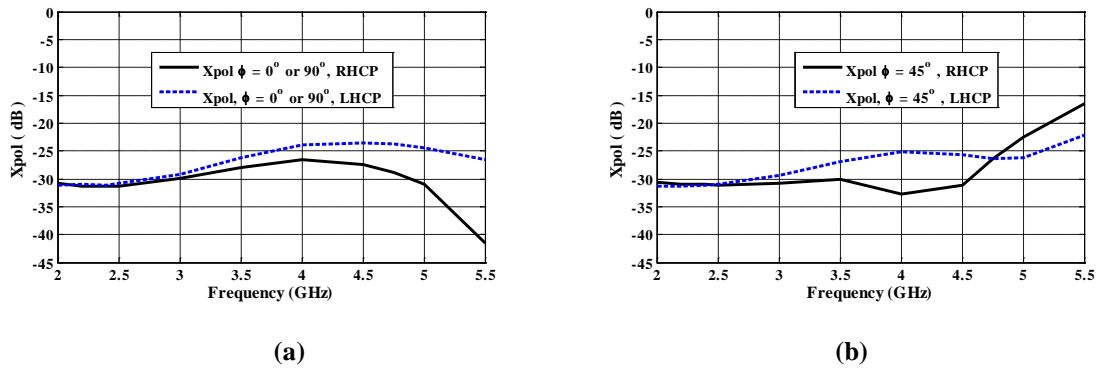
Fig. 5.5. RHCP and LHCP peak cross-polarization levels of the reflector antenna shown in Fig. 5.1 with D=20λ and F/D=0.536 versus frequency, when illuminated by the proposed spiral antenna of case I with r_{GND}=60mm, a=2.55 mm/rad, w=2mm, h=11.5mm, and n=1, at (a) principal planes of 0° and 90°, and (b) ϕ=45° plane.

As representative examples, the secondary co-polar and cross-polar radiation patterns of the reflector antenna with F/D=0.536 and D=20λ, illuminated by the proposed spiral antenna of case I in Fig. 4.1, are shown in Fig. 5.6 at the two frequencies of 3.5GHz and 4.75GHz, where maximum efficiency is achieved for LHCP and RHCP waves, respectively. The co-polar components are axial, with a peak at the boresight direction of θ=0°. The sidelobe levels well below -27dB are obtained for both senses of polarization. As an example, close-up presentations of the far-field radiation patterns at f=3.5GHz are also depicted in Fig. 5.7, over the angular range of -10° to $+10^o$. The performance of the reflector with D=20λ and F/D=0.536, illuminated with the spiral feed

101

of case I with *n*=1, is summarized in Table 5.2 for both senses of polarization, where gain, efficiencies, and peak cross-polarization at the diagonal plane of 45° are listed in the table.
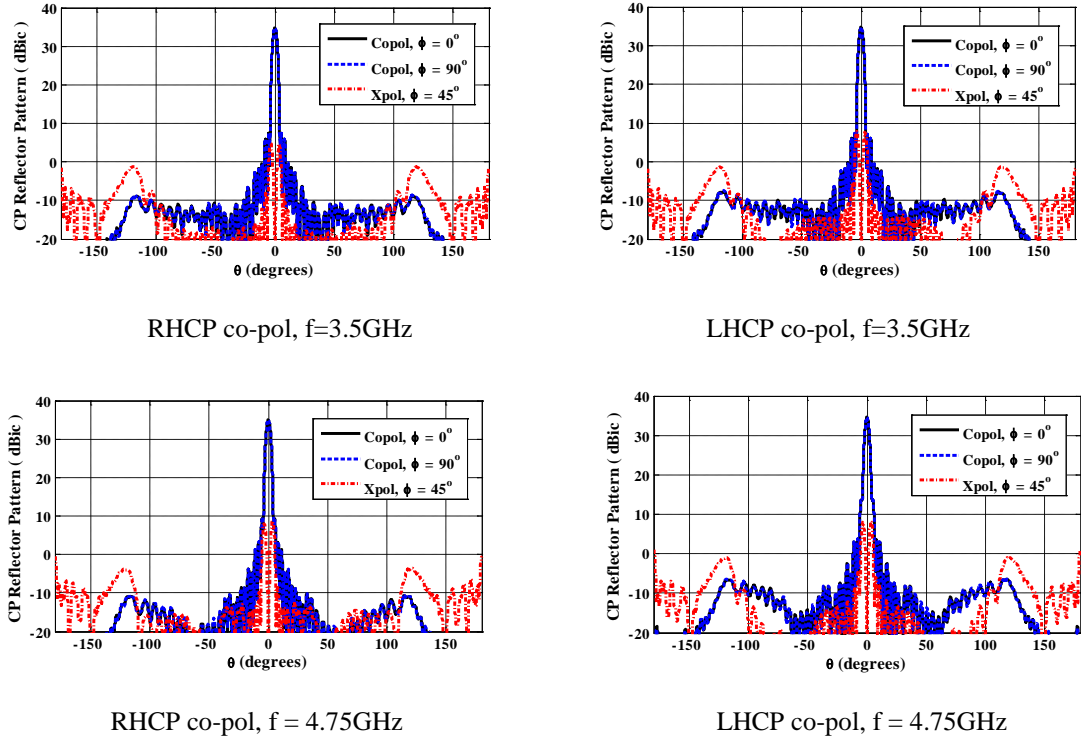
RHCP co-pol, f=3.5GHz

LHCP co-pol, f=3.5GHz

RHCP co-pol, f = 4.75GHz

LHCP co-pol, f = 4.75GHz

Fig. 5.6. Secondary co-pol and cross-pol radiation patterns of the reflector antenna shown in Fig. 5.1 with D=20λ and F/D=0.536, when illuminated by the proposed spiral antenna of case I with r_{GND}=60mm, *a*=2.55 mm/rad, *w*=2mm, *h*=11.5mm, and *n*=1.

RHCP co-pol, f=3.5GHz

LHCP co-pol, f=3.5GHz
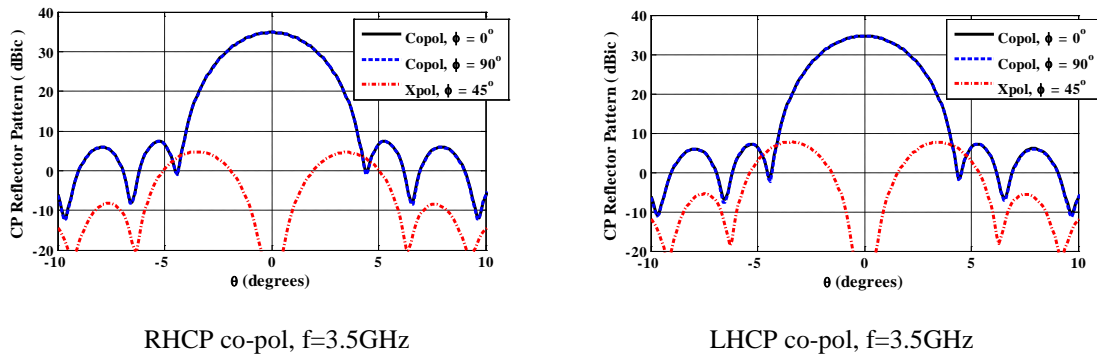
Fig. 5.7. Close-up secondary co-pol and cross-pol radiation patterns of the reflector antenna shown in Fig. 5.1 with D=20λ and F/D=0.536, when illuminated by the proposed spiral antenna of case I with r_{GND}=60mm, *a*=2.55 mm/rad, *w*=2mm, *h*=11.5mm, and *n*=1 at the frequency of 3.5GHz.

Table 5.2. Summary performance of the parabolic reflector antenna with D=20λ and F/D=0.536, fed by the spiral antenna of case I with r_{GND}=60mm, a=2.55 mm/rad, w=2mm, h=11.5mm, and n=1.

Frequency (GHz)	RHCP			LHCP		
	Gain (dBic)	Efficiency	Xpol(dB) $\phi = 45^o$	Gain (dBic)	Efficiency	Xpol(dB) $\phi = 45^o$
2.0	34.18	66.32%	-30.68	34.33	68.70%	-31.34
2.5	34.53	71.81%	-31.09	34.62	73.40%	-30.99
3.0	34.70	74.75%	-30.71	34.73	75.21%	-29.36
3.5	34.82	76.88%	-30.03	**34.74**	**75.38%**	**-26.99**
4.0	34.88	77.87%	-32.66	34.66	74.05%	-25.18
4.5	34.93	78.87%	-31.14	34.58	72.80%	-25.72
4.75	**34.96**	**79.33%**	**-26.31**	34.55	72.24%	-26.34
5.0	34.92	78.66%	-22.49	34.52	71.72%	-26.19
5.5	34.53	71.87%	-16.42	34.38	69.37%	-22.23

5.3.2 Primary Feed of Case II with r_{GND}=37.5mm

In this section, the performance of the reflector antenna is investigated, when it is fed by the proposed spiral antenna of case II in section 4.4.2. The primary feed is smaller in the lateral dimension, which leaves fewer blockage on the reflector surface as compared to the feed in case I. The reflector has a circular rim with a 20λ diameter as before. The feed is placed at the focal point of the reflector, whose focal length varies from 0.25D to 2.857D, where D=20λ at the frequency of 3.5GHz. In other words, the reflector subtended half-angle changes from 10° to 90°. The results of the efficiencies against different F/D ratio are shown in Fig. 5.8. Similar to the previous case, the efficiency peaks for a specific F/D ratio. The maximum efficiency of 75% is obtained when F/D=0.48 which is equivalent to θ^*=55°, for RHCP and LHCP operations. As observed in Fig. 5.8, the trend of efficiency performance is almost identical for both senses of polarization irrespective of the selected spiral number of turns.
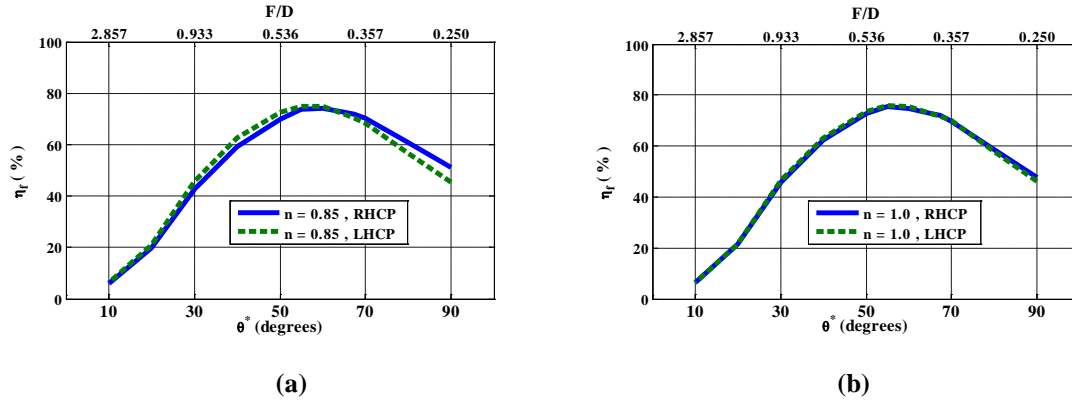
Fig. 5.8. RHCP and LHCP efficiencies of the reflector antenna shown in Fig. 5.1 with D=20λ at f=3.5GHz versus different F/D ratios, when illuminated by the proposed spiral antenna of case II with r_{GND}=37.5mm, a=2.55 mm/rad, w=2mm, and h=11.5mm with number of spiral turns of (a) n=0.85 and (b) n=1. Top and bottom horizontal axes show subtended half-angle θ* and the corresponding F/D, respectively.

The frequency responses of the reflector antenna are carried out for the parabolic reflector with an F/D=0.48, at which the maximum efficiency occurs, as illustrated in Fig. 5.8 when the spiral number of turns is 1.0. The same frequency range of 2.0-5.5GHz is assumed as before. The boresight CP gains of the reflector are plotted in Fig. 5.9 for both RHCP and LHCP fields, which are flat and near 34.5dBic over the range of 2.5-5.5GHz. The slight gain drop at the low frequency end below 2.5GHz is due to the large beamwidths of the spiral feed of case II, as shown in Fig. 4.9. The corresponding efficiencies are shown in Fig. 5.10 versus frequency. Maximum efficiencies of 77.82% at f=4.5GHz and 76.15% at f=3.0GHz are obtained for the RHCP and LHCP waves, respectively. An average efficiency of about 73% is realized over the frequency range of 2.5-5.5GHz for both senses of polarization.
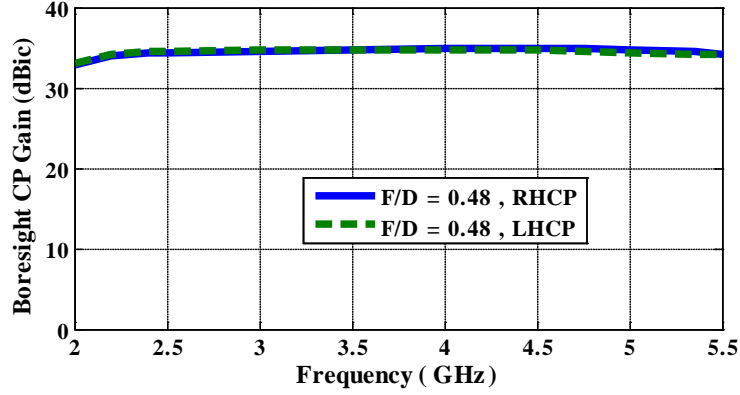
Fig. 5.9. Frequency response of the RHCP and LHCP boresight gains of the reflector antenna shown in Fig. 5.1 with D=20λ and F/D=0.48, when illuminated by the proposed spiral antenna of case II with r_{GND}=37.5mm, a=2.55 mm/rad, w=2mm, h=11.5mm, and n=1.
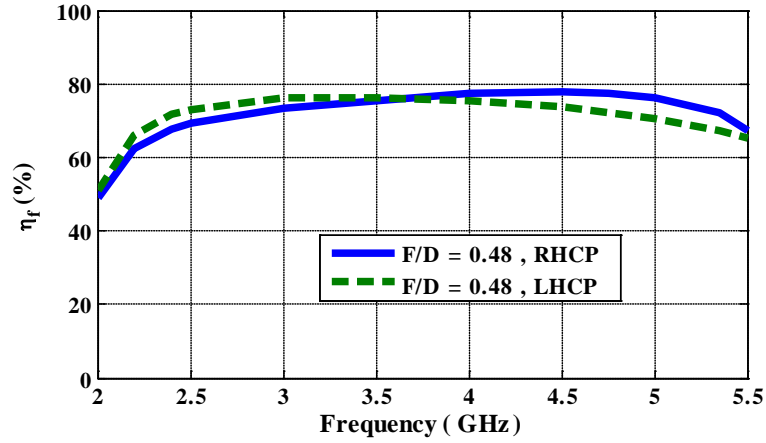
Fig. 5.10. Frequency response of the RHCP and LHCP efficiencies of the reflector antenna shown in Fig. 5.1 with D=20λ and F/D=0.48, when illuminated by the proposed spiral antenna of case II with r_{GND}=37.5mm, a=2.55 mm/rad, w=2mm, h=11.5mm, and n=1.

The peak cross-polarization levels of the reflector antenna under study are also shown in Fig. 5.11 at the diagonal and principal planes for both senses of polarization, when the spiral number of turns is 1.0. They are less than -24dB over the frequency range of 2.0-5.0GHz and slightly larger beyond up to 5.5GHz, which makes the reflector antenna a perfect transmit/receive device in frequency reuse applications with circular polarization with enhanced wireless channel capacity.

105
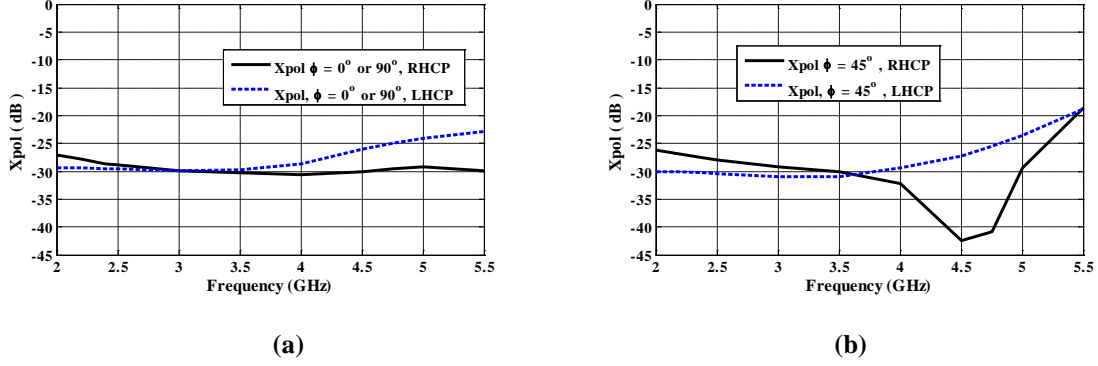
Fig. 5.11. RHCP and LHCP peak cross polarization levels of the reflector antenna shown in Fig. 5.1 with D=20λ and F/D=0.48 versus frequency, when illuminated by the proposed spiral antenna of case II with r_{GND}=37.5mm, a=2.55 mm/rad, w=2mm, h=11.5mm, and n=1, at (a) principal planes of 0° and 90°, and (b) ϕ=45° plane.

The far-field CP radiation patterns of the reflector antenna with the spiral antenna of case II of n=1 are shown in Fig. 5.12 at frequencies of 3.0GHz and 4.5GHz, where maximum efficiencies are realized for LHCP and RHCP waves, respectively. The copolar patterns are axial, whereas the crosspolar ones have a null at the θ=0° direction and their peaks at the diagonal plane of ϕ=45° are less than -27dB for these frequencies. The sidelobe levels are also well below -27dB. For better illustration, close-up versions of the CP far-field radiation patterns at f=4.5GHz are also illustrated in Fig. 5.13, over the observation angle of -10° to +10°.

The performance of the reflector with D=20λ and F/D=0.48, illuminated with the spiral feed of case II with n=1, is summarized in Table 5.3 for both RHCP and LHCP fields, where gain, efficiencies, and peak cross-polarization at the ϕ=45° plane are listed in the table.

106
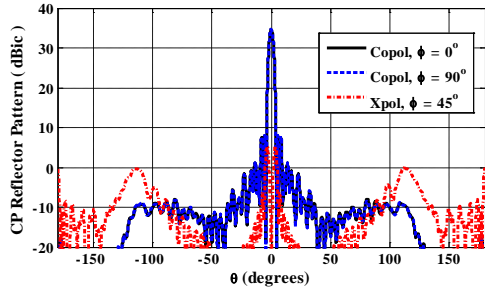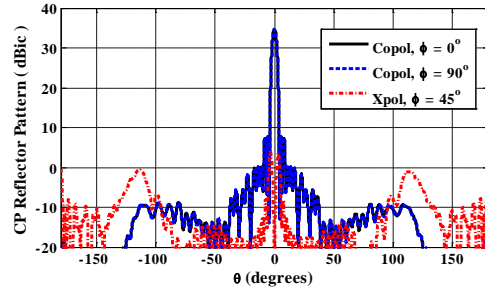
RHCP co-pol, f = 3.0GHz

LHCP co-pol, f = 3.0GHz
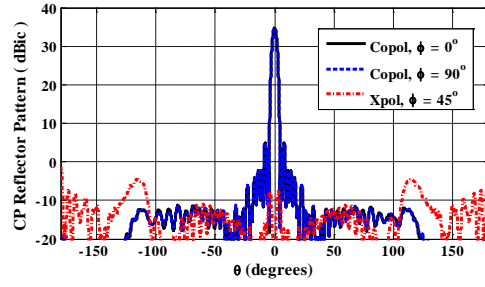
RHCP co-pol, f = 4.5GHz
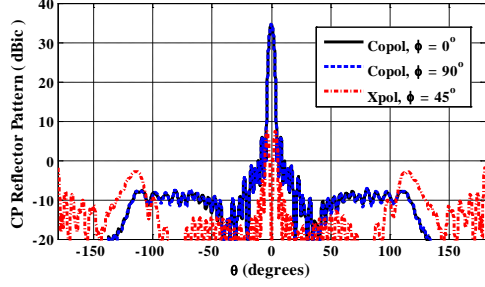
LHCP co-pol, f = 4.5GHz

Fig. 5.12. Secondary co-pol and cross-pol radiation patterns of the reflector antenna shown in Fig. 5.1 with D=20λ and F/D=0.48, when illuminated by the proposed spiral antenna of case II with r_{GND}=37.5mm, a=2.55 mm/rad, w=2mm, h=11.5mm, and n=1.
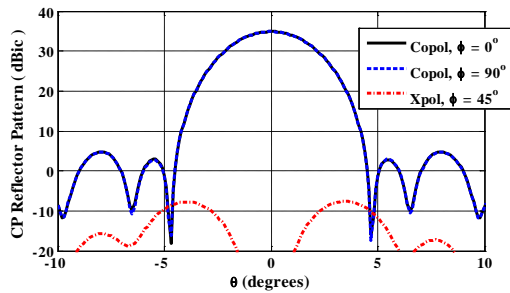

RHCP co-pol, f=4.5GHz
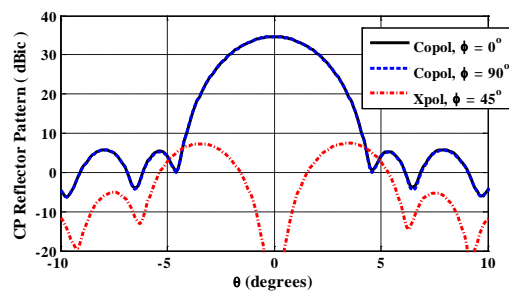
LHCP co-pol, f=4.5GHz

**Fig. 5.13. Close-up secondary co-pol and cross-pol radiation patterns of the reflector antenna shown in Fig. 5.1 with D=20λ and F/D=0.48, when illuminated by the proposed spiral antenna of case II with r_{GND}=37.5mm, a=2.55 mm/rad, w=2mm, h=11.5mm, and n=1 at the frequency of 4.5GHz.**

Table 5.3. Summary performance of the parabolic reflector antenna with D=20λ and F/D=0.48, fed by the spiral antenna of case II with r_{GND}=37.5mm, a=2.55 mm/rad, w=2mm, h=11.5mm, and n=1.

Frequency (GHz)	RHCP			LHCP		
	Gain (dBic)	Efficiency	Xpol(dB) $\phi = 45^\circ$	Gain (dBic)	Efficiency	Xpol(dB) $\phi = 45^\circ$
2.0	32.86	48.96%	-26.23	33.03	50.93%	-30.13
2.5	34.37	69.32%	-28.02	34.61	73.15%	-30.40
3.0	34.62	73.37%	-29.25	**34.78**	**76.15%**	**-31.04**
3.5	34.74	75.38%	-30.03	34.77	76.04%	-31.01
4.0	34.85	77.33%	-32.13	34.74	75.39%	-29.33
4.5	**34.87**	**77.82%**	**-42.52**	34.64	73.69%	-27.20
4.75	34.85	77.43%	-40.86	34.55	72.21%	-25.51
5.0	34.77	76.02%	-29.45	34.44	70.41%	-23.50
5.5	34.25	67.32%	-18.53	34.11	65.19%	-18.80

5.4 Reflector Antennas with Backward Spiral Feeds

In this section, a compact and center-fed four-arm Archimedean spiral antenna is investigated to address both its rear-radiating properties as a primary feed and its applications in symmetric front-fed parabolic reflector antennas. The backward feeds are of special interest in small front-fed reflector antennas, since they eliminate the need for mechanical struts. Instead, they can be easily mounted through a single rod extended from the reflector apex toward its focal point. It is shown that the spiral antenna generates broadside CP backward radiation patterns with an opposite sense of polarization to the spiral winding direction, when its circumference is well below the conventional active zone of the first mode, which is in the order of one wavelength. First, the realization of the backward radiation in spiral antennas is explained. Different antenna properties such as CP gain, beamwidths, and cross-polarization are discussed and presented. Then, the performances of the proposed backward CP spiral feeds are studied as primary feeds in symmetric parabolic reflector antennas. The secondary radiation patterns and the reflector

gain factor will be presented, validating the effectiveness of the proposed backward feed assembly through a single rod, without the need for extra supporting struts in practice. The numerical results are carried out by the full-wave Finite-Element based electromagnetic solver, ANSYS HFSS V.15 [25].

5.4.1 Four-Arm Archimedean Spiral Antenna as a Rear-Radiating Element

The radiation mechanism of spiral antennas is best understood based on the current band theory, qualitatively explained in 1960 by Kaiser [4] for a planar two-arm Archimedean spiral. According to this theory, the radiation occurs within an annular ring, over which the currents in the neighboring arms become in-phase. For the dominant mode with a broadside radiation pattern, the circumference of the ring is about one wavelength, λ. This ring is often referred to as the active region. It is well known that a free-standing planar spiral antenna radiates bidirectional CP waves into the upper and lower half-space regions. In most applications, however, a unidirectional radiation is desired. This is normally realized by placing the spiral antenna above a ground plane, larger than the spiral arm diameter, to effectively direct the energy in the upper half-space medium. If the ground plane size reduces to the order of the spiral diameter, then the radiation patterns become bidirectional. Therefore, as opposed to the helical antenna in [68], shrinking the ground plane size does not result in a backward radiation for a spiral antenna. However, if the spiral diameter is smaller than the conventional active region of λ, it is possible to direct the radiation of the first mode to the lower-half space, which is the main objective of this section. For such a reduced-sized spiral, the currents travel

along the spiral arms, producing significant reflected waves at the arm ends. The reflected waves experience a phase progression toward the center of the spiral. The associated induced currents on the supporting ground plane will then result in backward radiation patterns. The sense of polarization of the corresponding CP waves is opposite to the winding direction of the spiral, due to the fact that the reflected waves are now the source of radiation.

The geometry of the proposed feed is shown in Fig. 5.14. It is a planar center-fed Archimedean four-arm spiral antenna with a counter-clockwise winding direction. The spiral parameters are based on the proposed spiral antenna in previous chapter, with much reduced spiral arm ends to better facilitate the aforementioned reflected waves. Thus, the spiral number of turns is smaller than unity and it is around 0.4. The supporting ground plane has a radius of 25mm. Four RG174 coaxial cables are connected to spiral inner arms to excite the antenna with equal amplitudes and phase progression of 0°, -90°, -180°, and -270°, according to the spiral first mode to produce a broadside radiation pattern. The outer radius of the spiral should be a small fraction of the conventional one-wavelength zone to direct the radiation backward with a left-hand circular polarization.

(a)   (b)
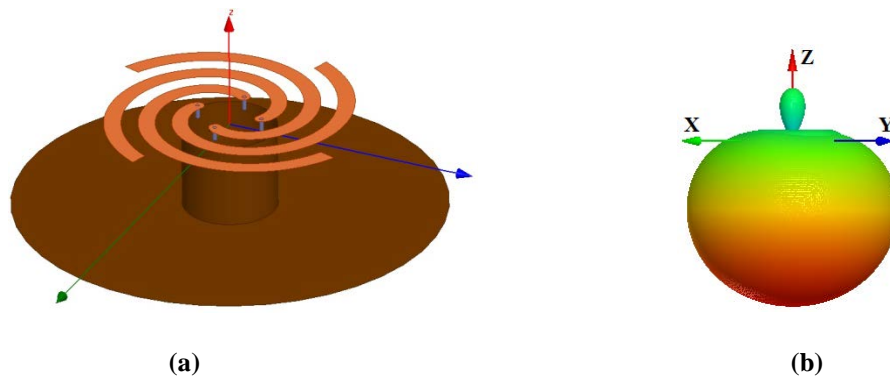
Fig. 5.14. (a) 3-D view and of the proposed four-arm Archimedean spiral antenna with a=2.55 mm/rad, w=2mm, h=11.5mm, and r_{GND}=25mm (b) typical backward radiation pattern of the proposed feed.

5.4.2 Results of Rear-Radiating Archimedean Spiral Antennas

In this section, numerical results of the proposed rear-radiating four-arm Archimedean spiral antenna are presented when the radius of the supporting ground plane is 25mm. Spiral numbers of turns as small as 0.3, 0.4, and 0.5 are selected to prevent forming the conventional- one-wavelength active zone required for the forward radiation. For the counter-clockwise spiral arms illustrated in Fig. 5.14 excited by equal amplitudes and aforementioned progressive phase shifts, the antenna radiates backward with an opposite sense of polarization, i.e. left-handed circular polarization (LHCP). The corresponding LHCP gains at the $\theta=180^{o}$ direction are plotted in Fig. 5.15a over the frequency range of 1-3GHz. The LHCP gain reaches its maximum value of about 7dBic at the frequency of 2.5GHz. It is noted that the circumference of the largest spiral arms, i.e. $n=0.5$, is only 0.76λ at the highest frequency of 3GHz over the above band, which is sufficiently smaller than the one-wavelength conventional active zone. As mentioned earlier, the induced current on the ground plane is the source of backward radiation. Thus, as the selected spiral number of turns increases, the effective aperture area on the ground plane enlarges, improving the LHCP gain.

The associated axial ratios of the antenna at the end-fire direction of 180° are shown in Figure 5.15b, values of which are well below 0.5dB representing an excellent CP performance around this direction.
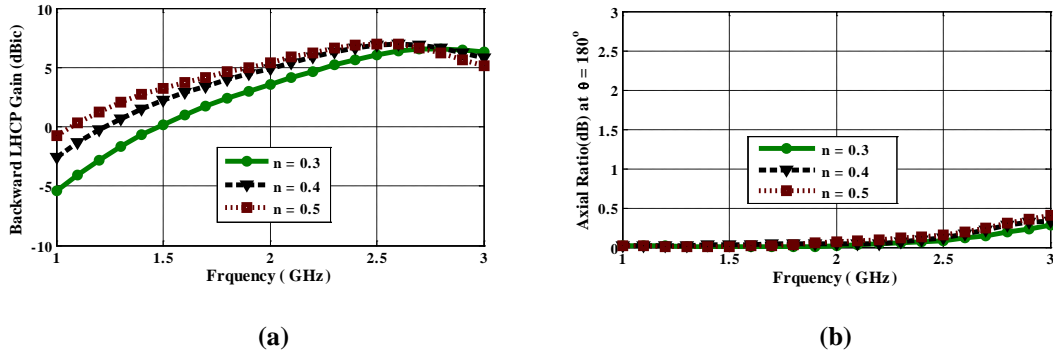
Fig. 5.15. (a) Peak LHCP gain and (b) axial ratios at the θ=180° of the proposed rear-radiating four-arm Archimedean spiral antenna shown in Fig. 5.14a with r_{GND}=25mm, a=2.55 mm/rad, w=2mm, and h=11.5mm.

In order to show the LHCP performance of the proposed antenna over the entire observations angles in space, the radiation patterns of the antennas are plotted in Fig. 5.16 at different frequencies for the spiral number of turn of 0.4. As can be seen, the antenna effectively radiates LHCP in the backward region. The cross-polarization components, i.e. the RHCP, within the main beam are small. However, the cross-polarization level at the forward axis of θ=0° tends to vary as frequency changes. In this regard, the best operation is observed at the frequency of 2.3GHz. To quantify this property, it is worth investigating the peak cross-polarization levels at both backward and forward regions. The corresponding results are depicted in Fig. 5.17. The peak cross-polarization within the backward main beam over the angular range ±70° off the peak is shown in Fig. 5.17a, becoming well below -15dB, equivalent to a 3dB axial ratio with larger spiral arms near the high frequency end. On the other hand, the cross-polarization at θ=0° reaches low levels only over a very narrow frequency band, as plotted in Fig. 5.17b. Since this occurs in the upper half-space, which is now the backlobe region, the conventional -15dB cross-polarization criterion can be relaxed to -10dB instead, equal to around 5dB axial ratio.

112

Complying with the -15dB and -10dB cross-polarization level criteria in the backward and forward regions, respectively, the effective frequency band of the backward feed is from 2.0 to 2.5GHz for n=0.4 and 0.5.
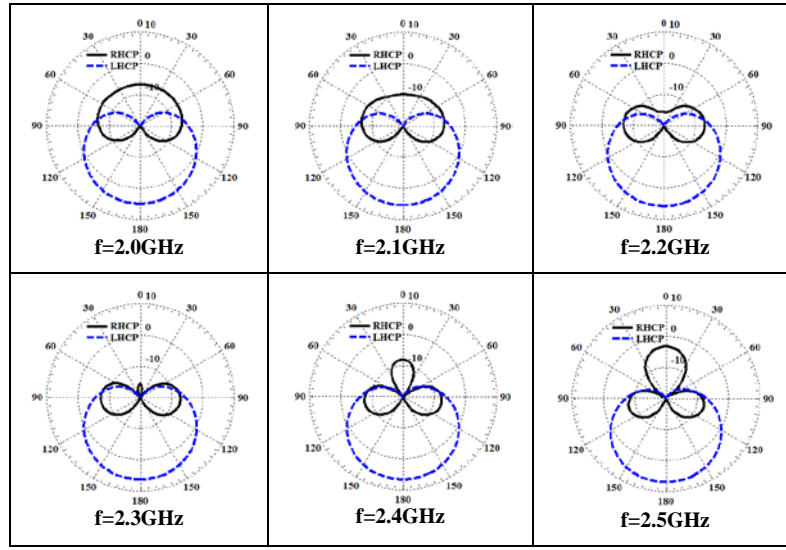
Fig. 5.16. LHCP and RHCP radiation patterns of the proposed rear-radiating four-arm Archimedean spiral antenna shown in Fig. 5.14a with r_{GND}=25mm, a=2.55 mm/rad, w=2mm, h=11.5mm, and n= 0.4.

(a)   **(b)**
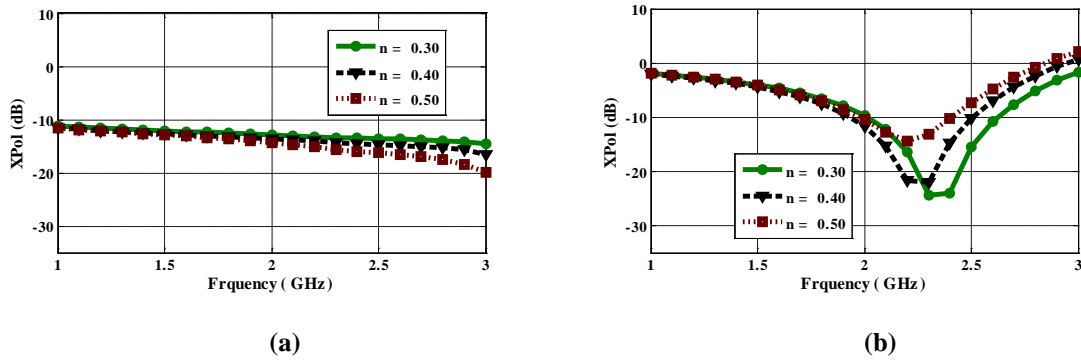
Fig. 5.17. (a) Peak cross-polarization within the angular range of $\pm 70^{o}$ away from the end-fire direction of θ=180°, and (b) back cross-polarization level at the θ=0° of the proposed rear-radiating four-arm Archimedean spiral antenna shown in Fig. 5.14a with r_{GND}=25mm, a=2.55 mm/rad, w=2mm, and h=11.5mm. The cross-polarization is the RHCP component at the ϕ=45° plane.

113

As stated earlier, such backward radiation properties make the proposed antenna an excellent candidate as a primary feed in front-fed symmetrical parabolic reflector antennas. Therefore, the pattern symmetry of the feed is significantly important. This is shown in Fig. 5.18, where 3-, 6-, and 10-dB beamwidths of the E- and H-plane radiation patterns of the proposed antenna are plotted versus frequency for the *n*=0.4 case. As observed, the antenna exhibits excellent symmetry with such equal beamwidths, which is due to the symmetrical structure of the proposed antenna. As a result, it is well suited as a feed for front-fed prime-focused reflector antennas with circular rims.
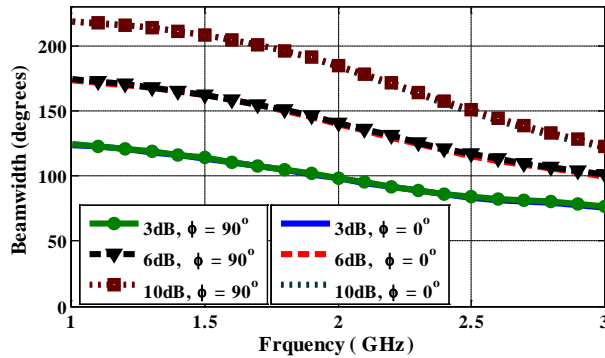
Fig. 5.18. The 3-dB, 6-dB, and 10-dB LHCP beamwidths at the principal planes of the proposed rear-radiating four-arm Archimedean spiral antenna shown in Fig. 5.14a with r_{GND}=25mm, a=2.55 mm/rad, w=2mm, h=11.5mm, and n= 0.4.

5.4.3   Performance of the Backward Spiral Antenna as a Primary Feed in Prime-Focus Parabolic Reflector Antennas

In this section, the performance of the proposed rear-radiating spiral antenna as a primary feed is investigated. The proposed backward antenna is placed at the focal point of a circular-rim parabolic reflector with an aperture diameter of 20λ, as shown in Fig. 5.19. Different focal lengths to diameter ratios (F/D), varying from 0.25 to 2.857, are

chosen to conduct our investigation, corresponding half illumination angles of 90° to 10°, respectively. The results of the secondary peak gains, which are now RHCP due to the phase reversal introduced by the reflecting surface, are shown in Fig. 5.20a at the frequency of 2.4GHz for spiral numbers of turns of 0.3 and 0.4. As can be seen, the gain reaches its maximum level when F/D=0.357 for both numbers of turns and it is larger when n=0.4, around 34dBic. The corresponding gain factors are plotted in Fig. 5.20b, showing an efficiency of 65%, when F/D=0.357 and n=0.4.
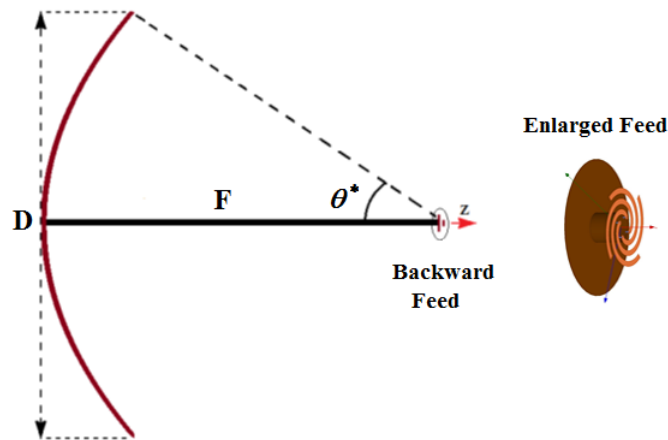
Fig. 5.19. Geometry of the front-fed circular-rim parabolic reflector antenna illuminated by the proposed rear-radiating spiral antenna in Fig. 5.14a, reflector aperture diameter: D=20λ.

(a)   (b)
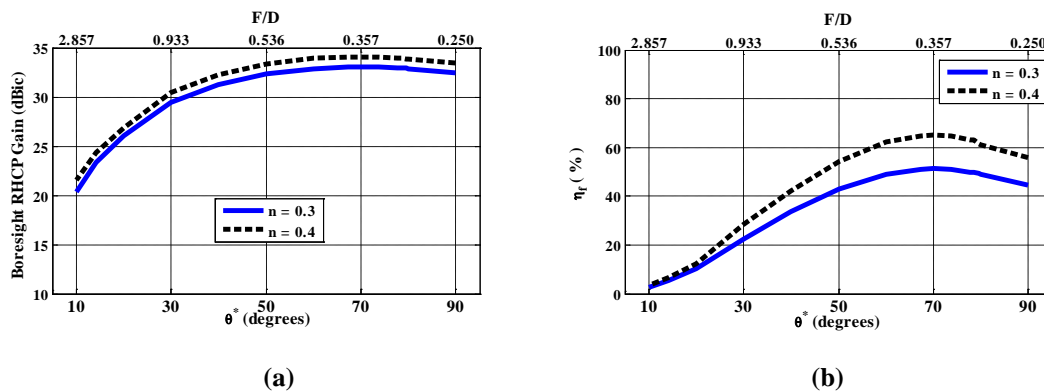
Fig. 5.20. (a) Boresight RHCP gain and (b) gain factors of the reflector illuminated by the backward spiral antenna in Fig. 5.14a, when the reflector aperture diameter is 20λ at f=2.4GHz.

Fig. 5.21 shows how the reflector boresight gain changes versus frequency for different F/D, when the spiral number of turns is equal to 0.4. As can be seen, the best performance is realized with a reflector structure defined by F/D=0.357, corresponding to a half-subtended angle of 70°, having a maximum gain of 34.2dBic.
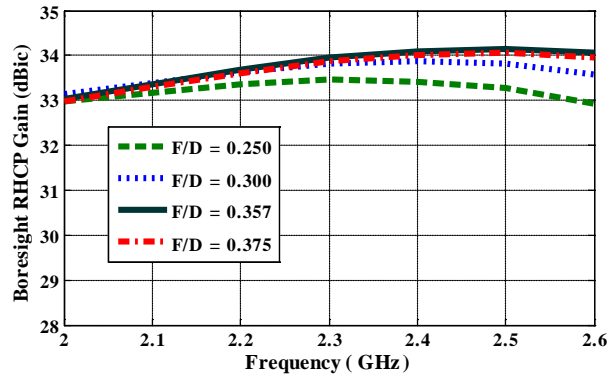
Fig. 5.21. Frequency response of the boresight gain of the parabolic reflector with an aperture diameter of 20λ illuminated by the backward spiral antenna in Fig. 5.14a with *n*=0.4 and *r*GND=25mm.

As a representative example, the secondary CP radiation patterns of the compound reflector and the proposed backward spiral feed are illustrated in Fig. 5.22 for a spiral number of turns of 0.4 at the frequency of 2.3GHz. The co-polar components are RHCP with a boresight gain of 33.92dBic and the peak cross-polarization levels, i.e. LHCP, are about 25dB below the co-polar one at the diagonal plane of 45°. For better illustration, a closed-up view of the radiation patterns is given in Fig. 5.22b.
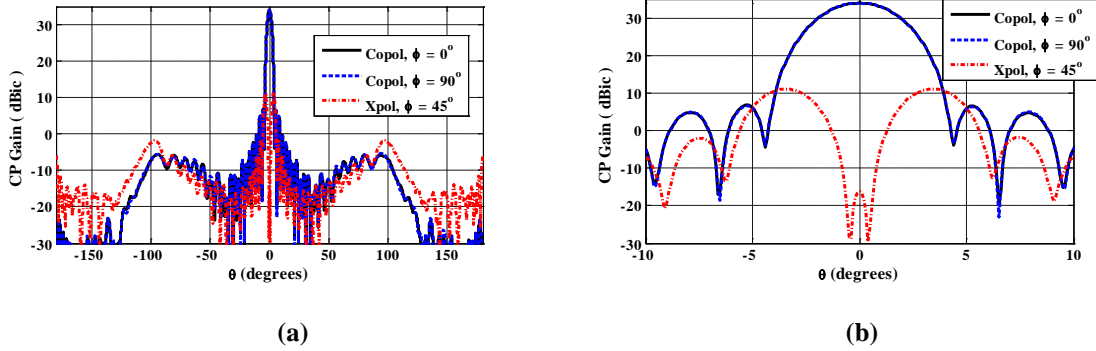
Fig. 5.22. Secondary CP radiation patterns of the parabolic reflector with an aperture diameter of 20λ and F/D=0.357, illuminated by the backward spiral antenna in Fig. 5.14a with n=0.4 and r_{GND}=25mm at f=2.3GHz, over (a) the whole observation angles and (b) angular range of ±10°.

5.5 Summary

Performances of compact forward and backward four-arm Archimedean spiral antennas were numerically investigated as primary feeds in front-fed parabolic reflector antennas with circular symmetry. The forward feeds were based on the dual-polarized CP spiral antennas proposed in chapter 4 as they exhibited excellent radiation pattern symmetry for both senses of polarization. Both cases I and II were extensively studied with two ground plane radii of 60mm and 37.5mm. Efficiencies as large as 77.8% and better were realized for symmetrical-cut paraboloids illuminated with these dual-polarized CP feeds. The resultant antennas contained excellent cross-polarization discriminations, well suited for frequency reuse wireless applications in order to improve the channel capacity. The footprint of the largest dimension of the proposed spiral feed with polarization diversity is only 1.4λ at the frequency of 3.5GHz, which introduces insignificant blockage on the illumination aperture even for reflectors as small as 20λ in diameter.

In addition, rear-radiating radiation properties of LHCP four-arm Archimedean spiral antennas were explored and their potentials as backward feeds in reflector antennas were numerically investigated. It was shown that one can effectively direct the spiral radiation into the backward region by properly selecting the spiral outer radius. In particular, when the circumference of the spiral is smaller than the one-wavelength active zone, normally required for the forward radiation of the first mode of the spiral, the induced currents on the ground plane resulted in rear-radiating type patterns. The maximum circumference size of about 0.75λ was found to be sufficient to create the backward radiation. This intriguing rear radiation was realized at the price of the reduced frequency bandwidth. Nonetheless, an efficiency of about 65% was achieved. In general, backward feeds become attractive in small front-fed reflectors as they can be easily mounted through a single rod extending from the apex of the reflector, resulting in considerable blockage suppression without the need for extra mechanical struts, which usually leave considerable shadow on the reflector illumination aperture. The physical size of the proposed backward spiral feed is only 0.33λ at the frequency of 2GHz, introducing negligible blockage even for a small reflector size in the order of 20λ.

Chapter 6

Dielectric Loaded Dual-Polarized Four-Arm Archimedean Spiral Antennas

6.1 Introduction

Inserting dielectric materials into an antenna structure, also known as capacitive loading, is widely used to miniaturize the antenna structure as it leads to an increased electrical path length [30]. This will then decrease the lower operating frequency of the antenna. Generally, high contrast substrates are needed in order for a significant reduction in the antenna size. However, the associated dielectric loss becomes particularly troublesome, which deteriorates the antenna efficiency performance. Low contrast dielectric materials, on the other hand, become quite beneficial for frequency tuning of already compact antenna structures, without a significant degradation in antenna performance.

In this chapter, frequency responses of the compact dual-polarized four-arm Archimedean spiral antennas, proposed in chapter 4, are numerically investigated when they are loaded with relatively low contrast dielectric materials. The direct advantage is to shift down the low end frequency band of such traveling antennas without the need to enlarge their electrical aperture sizes. Therefore, the antenna footprint will not change, making its electromagnetic shadowing effects intact in reflector antenna applications. In particular, the polarization diversity of proposed antennas is thoroughly studied when the

proposed compact antenna of case II with $r_{GND}=37.5$mm is loaded with low contrast substrates with dielectric permittivity up to 4.0. Three different dielectric loading profiles are discussed, namely full, partial, and grooved dielectric structures. The antenna parameters such as CP gain, beamwidths, radiation patterns, and cross polarization are addressed over their scaled frequency bands for both senses of polarization.

6.2   Fully Dielectric Loaded Spiral Antennas

In this section, the dual-polarized four-arm Archimedean spiral antenna of case II with the supporting ground radius of 37.5mm is loaded with dielectric substrate with the same axial and lateral profile of the antenna enclosing the shorting cylindrical wall, as shown in Fig. 6.1. To investigate the effects of dielectric loading, the spiral antenna parameters are kept unchanged. That is, a=2.55 mm/rad, w=2mm, h=11.5mm, and r_{GND}=37.5mm.   Two spiral numbers of turns of n=0.85 and n=1, with low contrast dielectric materials, with permittivities of 1.6, 2.5, and 4.0 are selected to conduct our investigation. In addition, the antenna loaded with a dielectric of ε_r=2.5 is further investigated for low profile structures with heights as small as 5.5mm and 1.7mm.
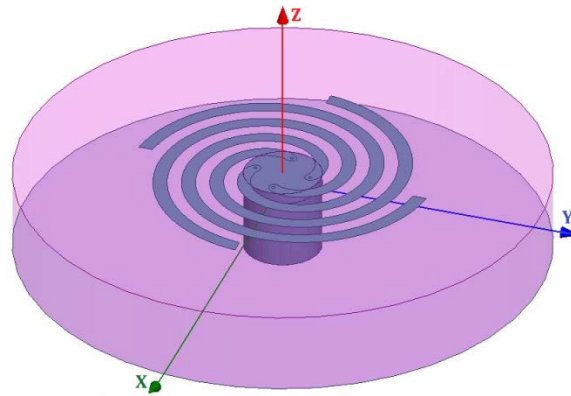
Fig. 6.1. Geometry of fully dielectric loaded four-arm Archimedean spiral antenna with polarization diversity; spiral constant of a=2.55 mm/rad, w=2mm, h=11.5, and r_{GND}=37.5mm, similar to the proposed feed of case II in section 4.4.2.

For the spiral number of turns of n=0.85, the results of boresight gains and peak cross polarization levels, obtained over the angular range of $\pm 90^o$ at the ϕ=45° plane, are presented in Fig. 6.2, for both senses of polarization. For the sake of comparison, the corresponding results of the reference case with no dielectric material are also given. The dielectric loading directly affects the frequency bandwidth of the antenna, as indicated in section 2.3.1, which makes it narrower with higher permittivity. For both RHCP and LHCP gains, a rapid roll-off rate occurs near the high-end frequency band as permittivity increases, which is quite noticeable for the LHCP gain. The reason is that the wavelength is inversely reduced by a factor of $\sqrt{\varepsilon_{eff}}$, which electrically enlarges the spiral circumference. Therefore, the currents find more opportunities to travel along the spiral arm and radiate out as RHCP waves rather than reflecting back to create the LHCP radiation. In addition, higher order modes [2], [74] may also excite as frequency increases further. As a result, the LHCP operation degrades faster than its RHCP counterpart. The low-end band shifts down from the original value of 1.8GHz, for the un-loaded case, to about 1.3GHz with ε_r=4.0. The -15dB cross polarization bandwidths also narrows as ε_r increases, having the same trend explained above for the gain. It is worth mentioning that the effective dielectric constant of a conventional microstrip line, etched on an infinite grounded dielectric slab, is specified by [75]

$$\varepsilon_{eff} = \frac{\varepsilon_r + 1}{2} + \frac{\varepsilon_r - 1}{2}\left(1 + 10\frac{h}{w}\right)^{-0.5} \qquad (6.1)$$

where h is the substrate height and w is the width of the microstrip line. For w=2mm, h=11.5mm, and ε_r=4.0, the effective dielectric constant is equal to 2.7 based on Eq. 6.1. For the present study, however, since curved lines such as spiral arms are assumed over a

finite ground plane, the effective dielectric constant will be smaller than 2.7. Based on the microstrip patch antenna [75], an effective dielectric constant of 1.92 can be estimated from the square of the low-end frequency ratio, i.e. $(1.8/1.3)^2$.

Thus, the dielectric loading method can be used to shrink the frequency bandwidth, which is useful to improve the signal to noise ratio, as well as scaling down the low frequency ends without the need to enlarge the physical aperture size of the antenna, while retaining its polarization diversity. Frequency responses of the gain and cross polarization with $n=1$ are depicted in Fig. 6.3. The trend is the same as explained for $n=0.85$. Because of the physically larger spiral size with $n=1$, the frequency bandwidths now become narrower compared with the $n=0.85$. The shared frequency bandwidths by both RHCP and LHCP waves of above cases are summarized and listed in Table 6.1, showing how one can tune the frequency bandwidths using low contrast dielectric materials.
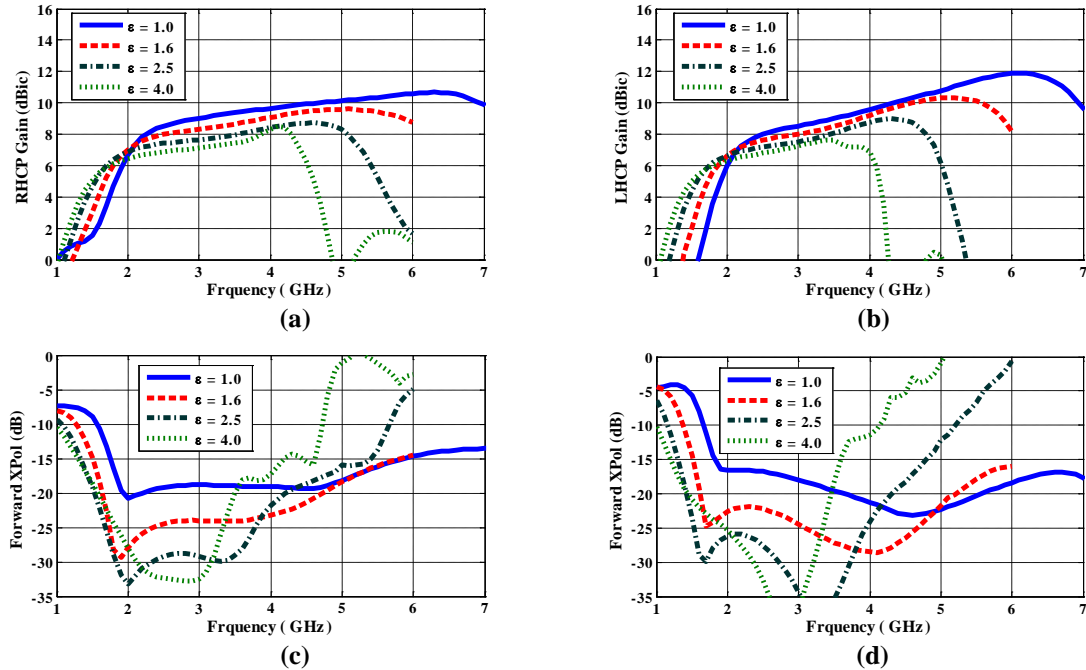
Fig. 6.2. (a) RHCP peak gain, (b) LHCP peak gain, (c) RHCP peak cross polarization, and (d) LHCP peak cross polarization of the antenna shown in Fig. 6.1 with $n=0.85$, loaded with different dielectric materials. The peak cross polarization is given at the $\phi=45^o$ plane in the forward region over $-90^o<\theta<+90^o$.

122
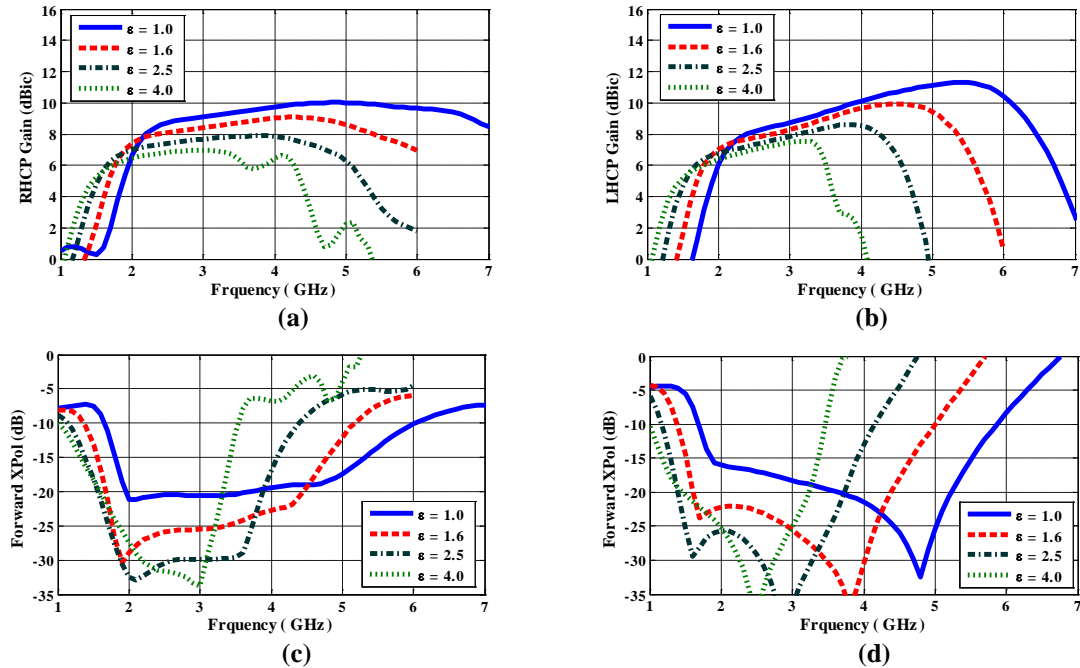
Fig. 6.3. (a) RHCP peak gain, (b) LHCP peak gain, (c) RHCP peak cross polarization, and (d) LHCP peak cross polarization of the antenna shown in Fig. 6.1 with *n*=1, loaded with different dielectric materials. The peak cross polarization is given at the φ=45° plane in the forward region over -90°<θ <+90°.

Table 6.1. Shared frequency bandwidths by both senses of polarization of the antenna shown in Fig. 6.1 fully loaded with different dielectric substrates for *n*=0.85 and *n*=1.

Dielectric Medium	Shared Frequency Bandwidths by both RHCP and LHCP	
	n=0.85	*n*=1
ε_r=1.0	1.8–5.8GHz	1.8–5.3GHz
ε_r=1.6	1.5–5.8GHz	1.5–4.7GHz
ε_r=2.5	1.35–4.8GHz	1.35–3.9GHz
ε_r=4.0	1.3–3.6GHz	1.3–3.35GHz

The 3, 6, and 10 dB beamwidths of the antenna, shown in Fig. 6.1, are also studied and the results are illustrated in Figs. 6.4 and 6.5, for the spiral numbers of turns of 0.85 and 1.0, respectively, for the selected permittivites of 1.6, 2.5, and 4.0. As can be observed, the RHCP and LHCP pattern symmetry preserves quite acceptably over their respective frequency bands as listed in Table 6.1. However, at frequencies above these bands the beamwidth symmetry is revoked with the presence of dielectric substrates. This

123

is because of the higher order modes as explained earlier [2], [74], which creates a partial null over the main beam and thus the beamwidth curves oscillate. To clarify this, corresponding RHCP and LHCP radiation patterns of the antenna with n=0.85 and ε_r=4.0 are illustrated in Fig. 6.6, at the frequency of 4.5GHz. This clearly illustrates unequal beamwidths of the CP patterns as the sense of polarization changes. Moreover, it is noted that for ε_r=1.6, as shown in Figs. 6.4a and 6.5a, the beamwidths below 1.5GHz are initially wide, since the antenna has not yet reached its conventional circularly polarized zone.

To illustrate the angular dependency of the CP radiation patterns of the resultant dielectric loaded antennas in Fig. 6.1, some representative examples are shown in Figs. 6.7 and 6.8, for two different spiral turns of n=0.85 and n=1, respectively, for both senses of polarization when ε_r=2.5. The selected frequencies are chosen to cover their respective bandwidths given in Table 6.1. They are 1.5GHz, 2.5GHz , and 3.5GHz for both numbers of spiral turns and near high frequency ends of 4.8GHz and 3.9GHz for n=0.85 and n=1, respectively. Dual-polarized waves generated by the antenna exhibit excellent CP performances over the mid- and high-end bands with slightly increased back cross polarization near the frequency of 1.5GHz. Since this occurs in the backward region, it is not of much concern in practical applications.

(a)   (b)

124

(c)
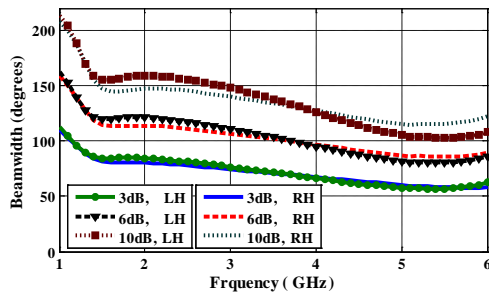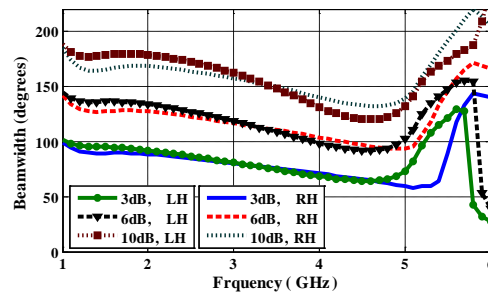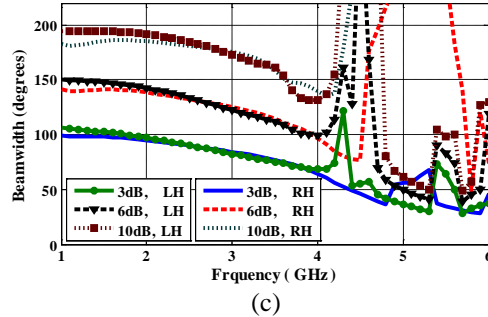
Fig. 6.4. 3-dB, 6-dB, and 10-dB RHCP-LHCP beamwidths of the antenna shown in Fig. 6.1 with
n=0.85, loaded with different dielectric materials of (a) ε_r=1.6, (b) ε_r=2.5, and (c) ε_r=4.0.
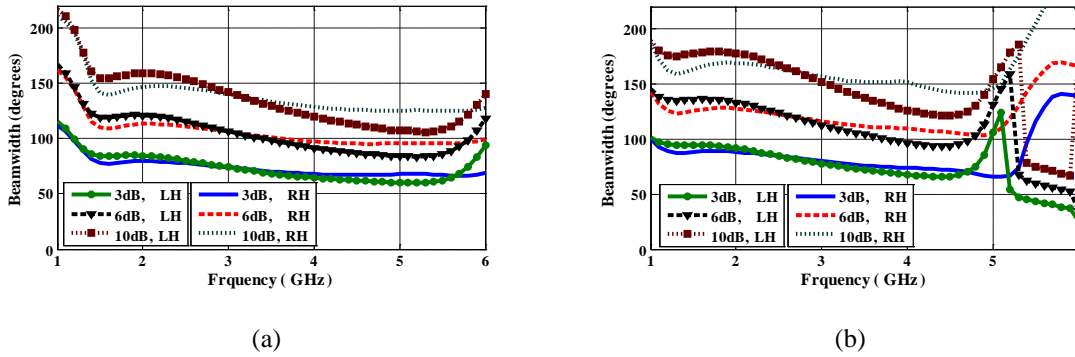
(a)

(b)
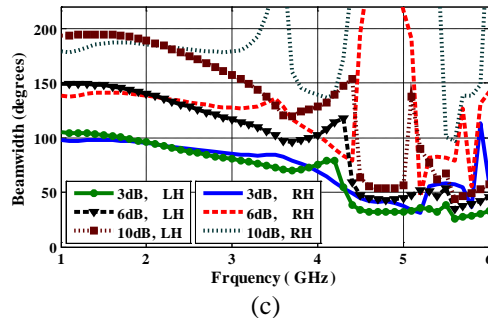
(c)

Fig. 6.5. 3-dB, 6-dB, and 10-dB RHCP-LHCP beamwidths of the antenna shown in Fig. 6.1 with n=1,
loaded with different dielectric materials of (a) ε_r=1.6, (b) ε_r=2.5, and (c) ε_r=4.0.
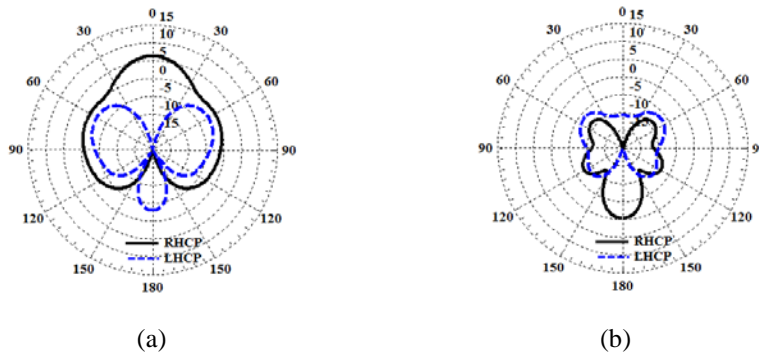
(a)

(b)

Fig. 6.6. RHCP and LHCP radiation patterns of the antenna shown in Fig. 6.1 with n=0.85, loaded
with a dielectric material of ε_r=4.0 at f=4.5GHz. The copolar component is (a) RHCP, (b) LHCP.
Co- and cross-polarized components are given at the principal and diagonal planes, respectively.

125

f=1.5GHz	f=2.5GHz	f=3.5GHz	f=4.8GHz
RHCP	RHCP	RHCP	RHCP
LHCP	LHCP	LHCP	LHCP
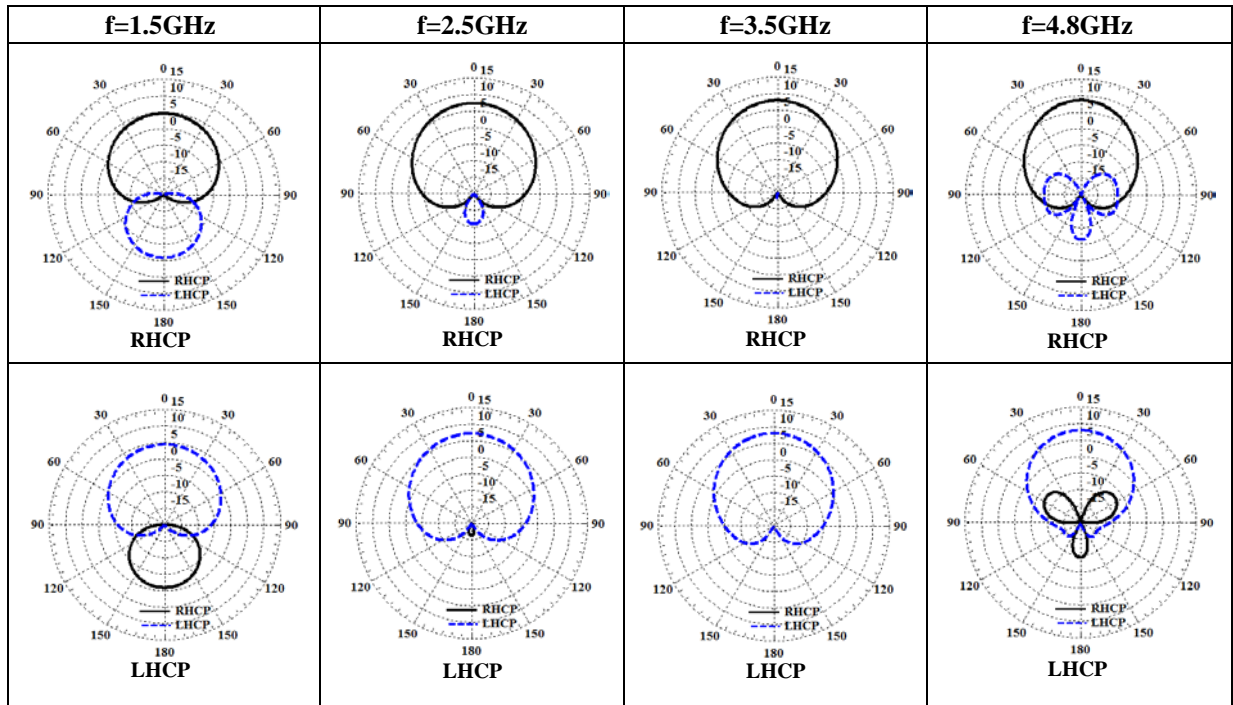
Fig. 6.7. RHCP and LHCP radiation patterns of the antenna shown in Fig. 6.1 with *n*=0.85, loaded with a dielectric material of ε$_r$=2.5 at the frequencies of 1.5GHz, 2.5GHz, 3.5GHz, and 4.8GHz. Co- and cross-polarized components are given at the principal and diagonal planes, respectively.

f=1.5GHz	f=2.5GHz	f=3.5GHz	f=3.9GHz
RHCP	RHCP	RHCP	RHCP
LHCP	LHCP	LHCP	LHCP
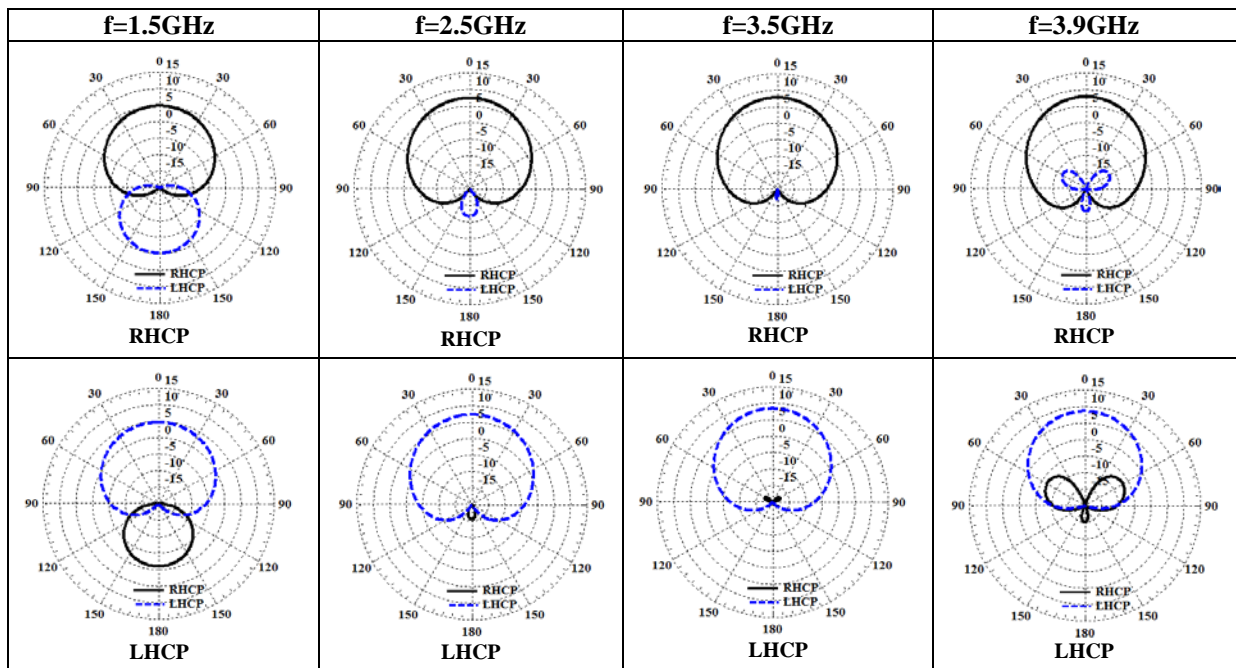
Fig. 6.8. RHCP and LHCP radiation patterns of the antenna shown in Fig. 6.1 with *n*=1, loaded with a dielectric material of ε$_r$=2.5 at the frequencies of 1.5GHz, 2.5GHz, 3.5GHz, and 3.9GHz. Co- and cross-polarized components are given at the principal and diagonal planes, respectively.

126

It is also worth investigating the dual polarized spiral antennas, fully loaded with dielectric materials, for low profile structures with reduced heights. To do so, the antenna in Fig. 6.1, loaded with a dielectric substrate of ε_r=2.5, is numerically analyzed, when its height decreases from 11.5mm to 5.5mm and 1.7mm. For the spiral number of turns of n=1, the results of boresight gains and peak cross polarization levels are illustrated in Fig. 6.9, for both senses of polarization. The CP gain frequency bandwidths considerably narrow as the height becomes as small as 1.7mm. As for the -15dB cross polarization responses, shown in Figs. 6.9c-d, the shared frequency bandwidths by both RHCP and LHCP waves widen from the upper ends, as the height decreases to 1.7mm.
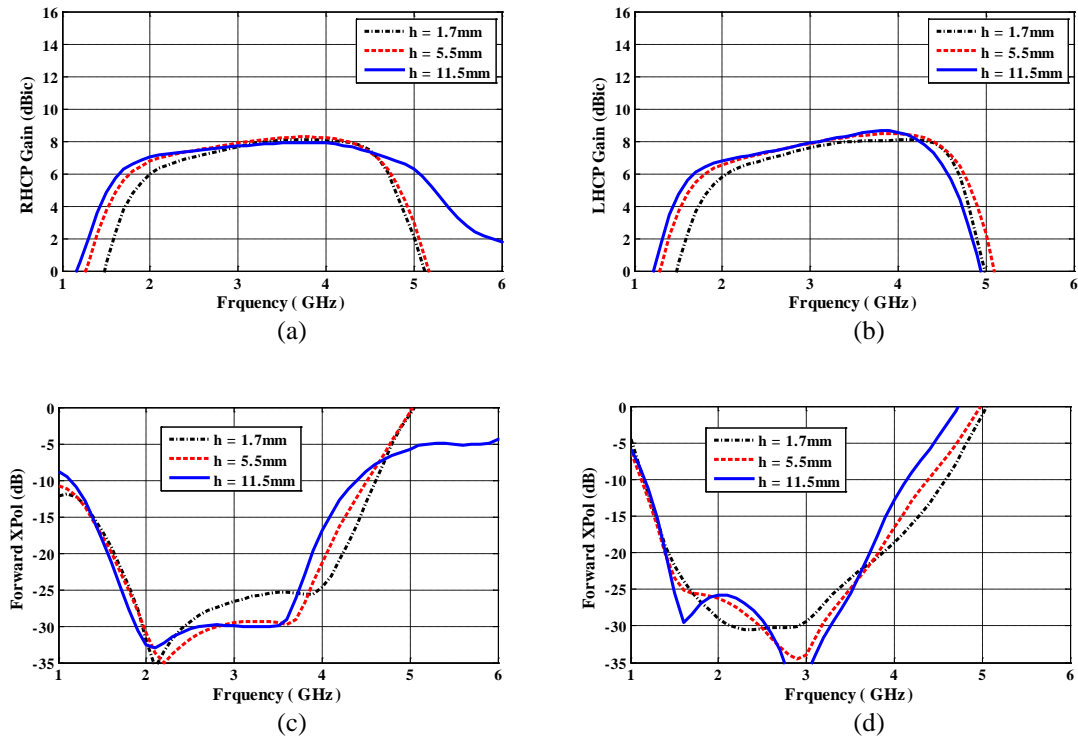

Fig. 6.9. (a) RHCP peak gain, (b) LHCP peak gain, (c) RHCP peak cross polarization, and (d) LHCP peak cross polarization of the antenna shown in Fig. 6.1 with n=1, fully loaded with a substrate of ε_r=2.5 for different structure heights. The peak cross polarization is given at the ϕ=45° plane in the forward region over -90°<θ <+90°.

127

6.3 Partially Dielectric Loaded Spiral Antennas

As shown in the preceding section, the impact of fully loaded dielectric on the polarization diversity performance introduces a convenient way to tune the operation frequency bandwidths of the spiral antenna under study. The dielectric loading decreased low-end frequency and narrowed the bandwidth. Now, the question becomes what if only the area under the spiral arms is loaded with the dielectric medium and how the frequency bandwidths vary accordingly. To address this question, the spiral antenna with a number of turn equal 1.0 is selected with a dielectric constant of $\varepsilon_r=2.5$ to further investigate the effects of a partial dielectric loading on the antenna performance. The geometry of the antenna is shown in Fig. 6.10a, wherein the dielectric is cut from the edge by a width denoted as W_{cut} in this figure. Thus, $W_{cut}=0$ refers to the fully dielectric loaded spiral discussed in the previous section with $\varepsilon_r=2.5$. As an example, the antenna geometry with $W_{cut}=20$mm is also depicted in Fig. 6.10b.

(a)   (b)
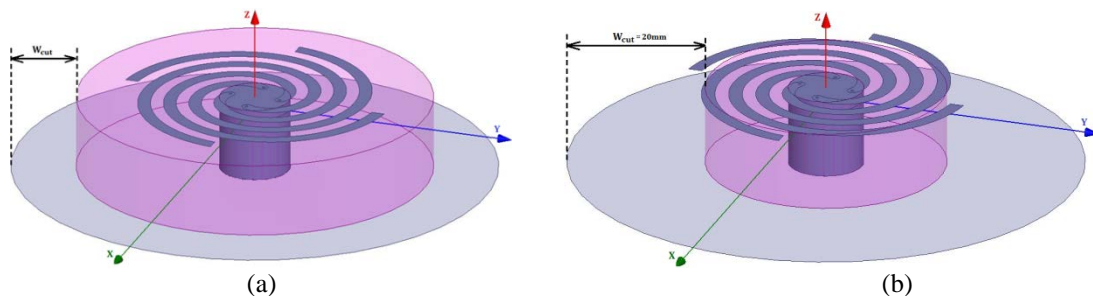
Fig. 6.10. (a) Geometry of partially dielectric loaded four-arm Archimedean spiral antenna with polarization diversity; spiral constant of $a=2.55$ mm/rad, $w=2$mm, $h=11.5$, and $r_{GND}=37.5$mm, similar to the proposed feed of case II in section 4.4.2, the dielectric is cut from the edge by W_{cut}; (b) Same geometry with $W_{cut}=20$mm.

The antenna depicted in Fig. 6.10a is numerically studied with different values of W_{cut} changing from 0 to 20mm with a 5mm increment for both senses of polarization.

The corresponding CP gains, at the boresight angle of $\theta=0^{\circ}$, and the peak cross polarization levels, at the diagonal plane of 45° over the observation angle of $\pm 90^{\circ}$, are illustrated in Fig. 6.11. As W_{cut} increases, indicating that the loaded dielectric region is mainly concentrated under the spiral arms, the low-end frequency slowly shifts up, whereas the high-end one grows much faster. The gain curves gradually start to restore the frequency responses, while the -15dB cross polarization bandwidth also improves. However, the rate of improvement in RHCP performance is much faster than its LHCP counterpart due to the electrically enlarged spiral region, better facilitating the RHCP operation as explained in the previous section. The resulting common frequency bandwidths versus W_{cut} are given in Table 6.2 to summarize the effect of partial loading.
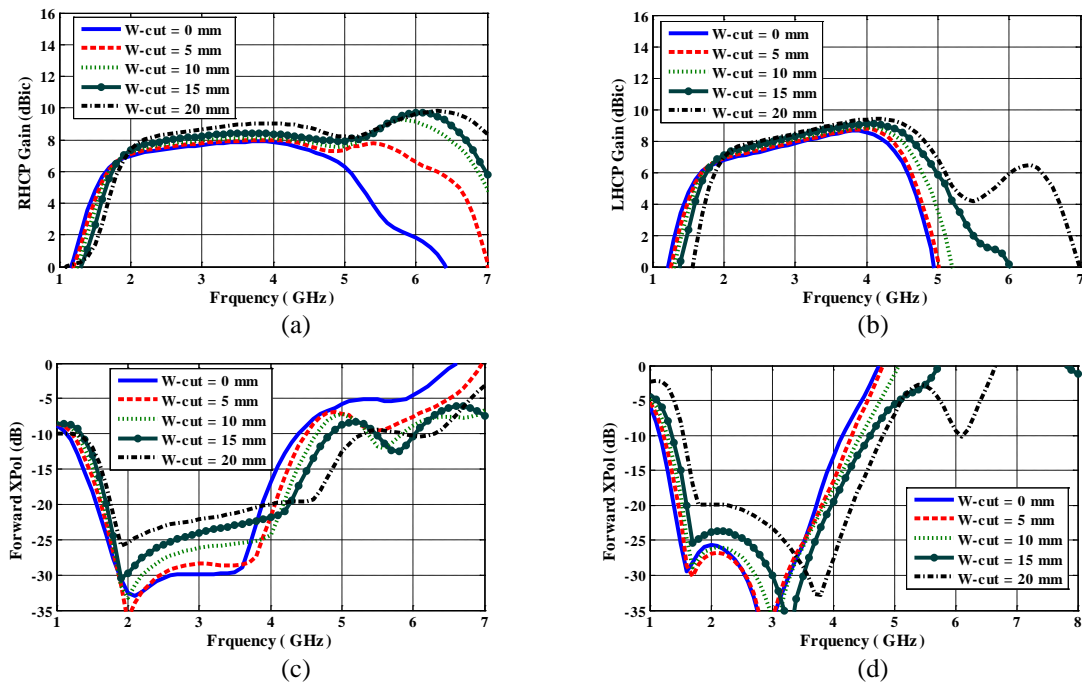
Fig. 6.11. (a) RHCP peak gain, (b) LHCP peak gain, (c) RHCP peak cross polarization, and (d) LHCP peak cross polarization of the antenna shown in Fig. 6.10a with n=1, partially loaded with a substrate of ε_r=2.5. The peak cross polarization is given at the ϕ=45° plane in the forward region over -90°<θ <+90°.

**Table 6.2. Shared frequency bandwidths by both senses of polarization of the antenna shown in Fig. 6.10a partially loaded with a substrate of ε_r=2.5, when n=1.**

W_{cut}	Shared Frequency Bandwidths by both RHCP and LHCP
0mm (full loading)	1.35–3.9GHz
5mm	1.45–4.1GHz
10mm	1.5–4.2GHz
15mm	1.55–4.3GHz
20mm	1.65–4.6GHz

As an example, the 3, 6, and 10 dB beamwidths of the partially loaded antenna in Fig. 6.10a, are plotted in Fig. 6.12, for both RHCP and LHCP waves, when W_{cut}=10mm. Over the shared frequency bandwidth of 1.5-4.2GHz, the half-power and 6-db beamwidths are close to each other, however the 10-dB beamwidths noticeably differ as the sense of polarization alters. This is due to the different frequency responses of RHCP and LHCP cases as depicted in Figs. 6.11a and 6.11b, respectively, wherein RHCP gain is almost flat against the aforementioned frequency range whereas the LHCP one increases monotonically with frequency, therefore the corresponding 10-dB beamwidths become noticeably different.
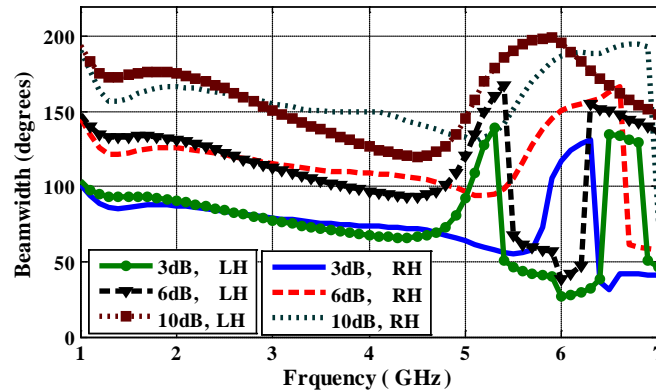
Fig. 6.12. 3-dB, 6-dB, and 10-dB RHCP-LHCP beamwidths of the antenna shown in Fig. 6.10a partially loaded with substrate of ε_r=2.5, when n=1 and W_{cut}=10mm.

The boresight axial ratios of the antenna under study with W_{cut}=10mm are shown in Fig. 6.13 for both senses of polarization and are well below 3dB over 1-5.5GHz range

for all values of W_{cut} up to 20mm. To completely illustrate the CP performance in space, the antenna radiation patterns are plotted in Fig. 6.14 for both senses of polarization, when W_{cut}=10mm at the selected frequencies of 1.5GHz, near the low-end, 2.5GHz, 3.5GHz, and high-end 4.2GHz, exhibiting excellent CP patterns for both RHCP and LHCP cases.

(a)   (b)
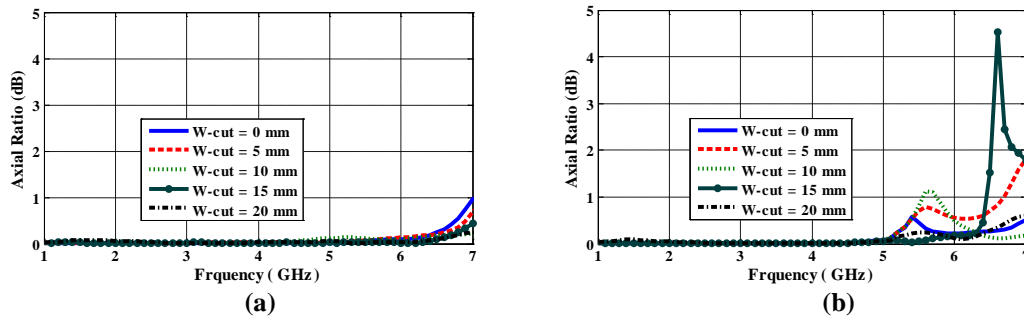
Fig. 6.13. (a) RHCP and (b) LHCP axial ratio at the θ=0° direction of the antenna shown in Fig. 6.10a with n=1, partially loaded with a substrate of ε_r=2.5.
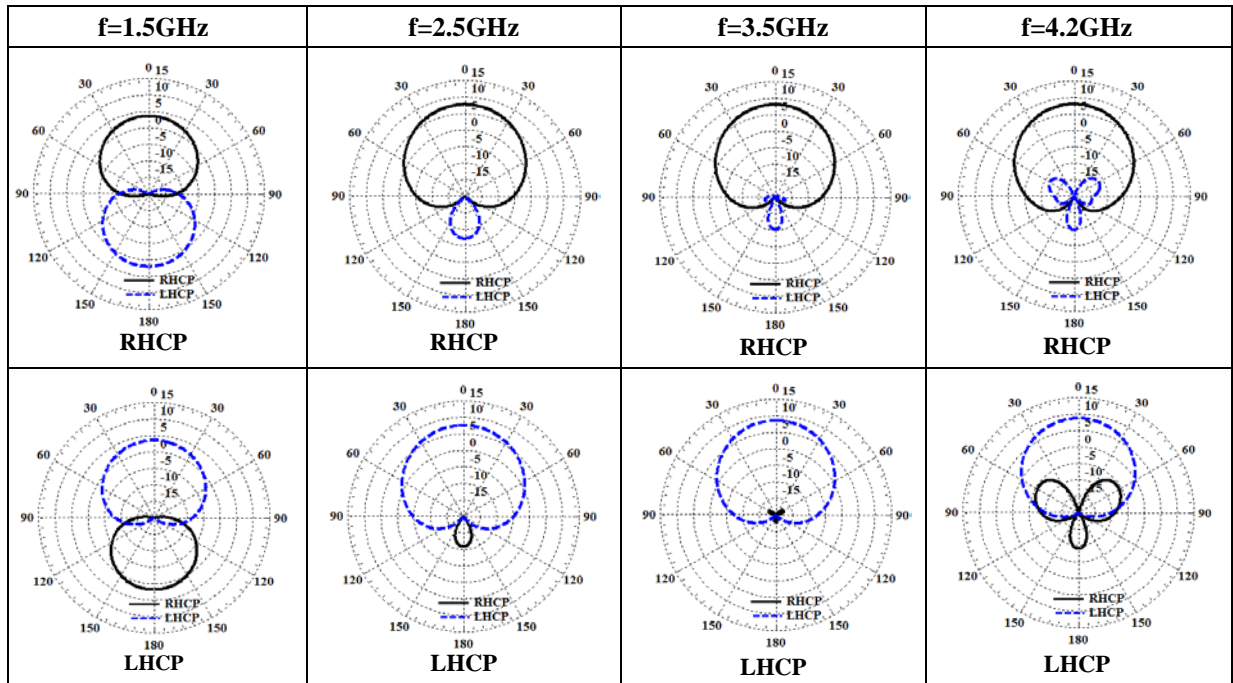
Fig. 6.14. RHCP and LHCP radiation patterns of the antenna shown in Fig. 6.10a partially loaded with substrate of ε_r=2.5, when n=1 and W_{cut}=10mm at the frequencies of 1.5GHz, 2.5GHz, 3.5GHz, and 4.2GHz. Co- and cross-polarized components are given at the principal and diagonal planes, respectively.

131

6.4   Spiral Antennas with Grooved Dielectric Substrates

In section 6.2, the proposed dual-polarized spiral antennas were fully loaded with different low-contrast substrates to tune their RHCP and LHCP frequency responses, which narrowed the bandwidth with lower-end operating frequency as permittivity increased. Thus, fine frequency tuning of the polarization diversity may be feasible with more quantified values of dielectric permittivity, e.g. ε_r = 1.6, 1.7, 1.8, and et cetera. In practice, however, dielectric substrates are available within standard ranges of permittivity and materials with a specific permittivity are difficult to realize with reasonable tolerances. Interestingly enough, the effective dielectric constant can be electrically altered by modifying the structure of a given dielectric by inserting air channels of arbitrary shapes into it. A convenient way of doing so for the proposed antenna in section 6.2 is to insert grooves [76] into the dielectric slab, as illustrated in Fig. 6.15 in which grooves are uniformly spaced starting from the dielectric outer edge. The groove widths are selected such that they are a small fraction of wavelength at low frequencies in the order of 0.01λ, which makes electromagnetic waves see a solid dielectric region at low frequencies. Therefore, the low frequency will not be affected by the grooved structure, whereas the overall bandwidth widens from high frequency ends. Grooves of 2.5mm wide and 11.5mm deep are then chosen for our study. In this section, the antenna such developed with four and six grooves, respectively shown in Fig. 6.15a and 6.15b, are investigated to address the polarization diversity responses of the antennas.

(a) four-groove   (b) six-groove
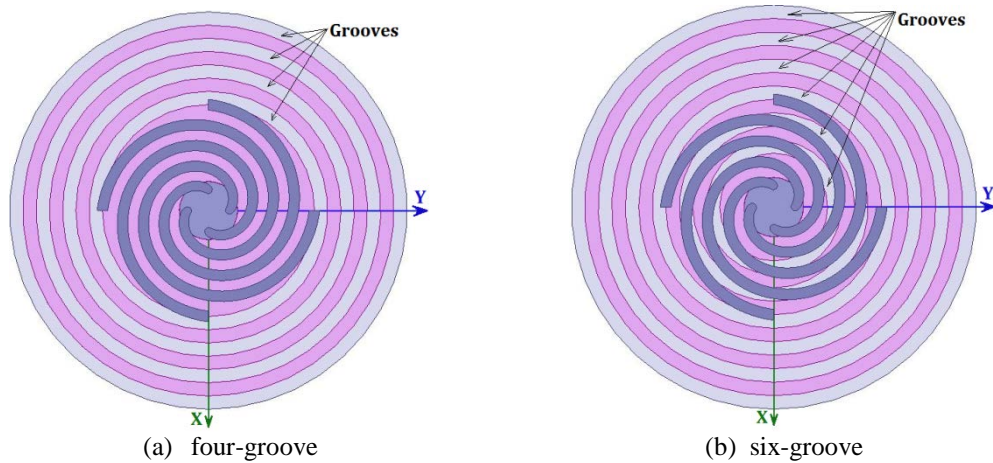
Fig. 6.15. Geometry of grooved dielectric loaded four-arm Archimedean spiral antenna with polarization diversity; spiral constant of a=2.55 mm/rad, w=2mm, h=11.5, and r_{GND}=37.5mm, similar to the proposed feed of case II in section 4.4.2; (a) four grooves and (b) six grooves.

Frequency responses of peak CP gain and maximum cross polarization levels of the antenna loaded with grooved substrate with ε_r=2.5 and number of spiral turn of 1.0 are shown in Fig. 6.16. The fully loaded antenna of same material is also plotted in the figure for comparison. As can be seen, the low-end frequency slightly changes with grooves, whereas the high-end frequency remarkably increases with more grooves inserted into the substrate. With regard to the -15dB cross polarization criterion, the antenna frequency bandwidths shared by both senses of polarization are summarized in Table 6.3, in which the six-groove case nearly mimics the behavior of a fully loaded antenna with ε_r close to 1.6. It is also worth mentioning that the dielectric loss is lesser in grooved structures than in solid materials and of course lighter in weight as well.

(a)

(b)

(c)

(d)
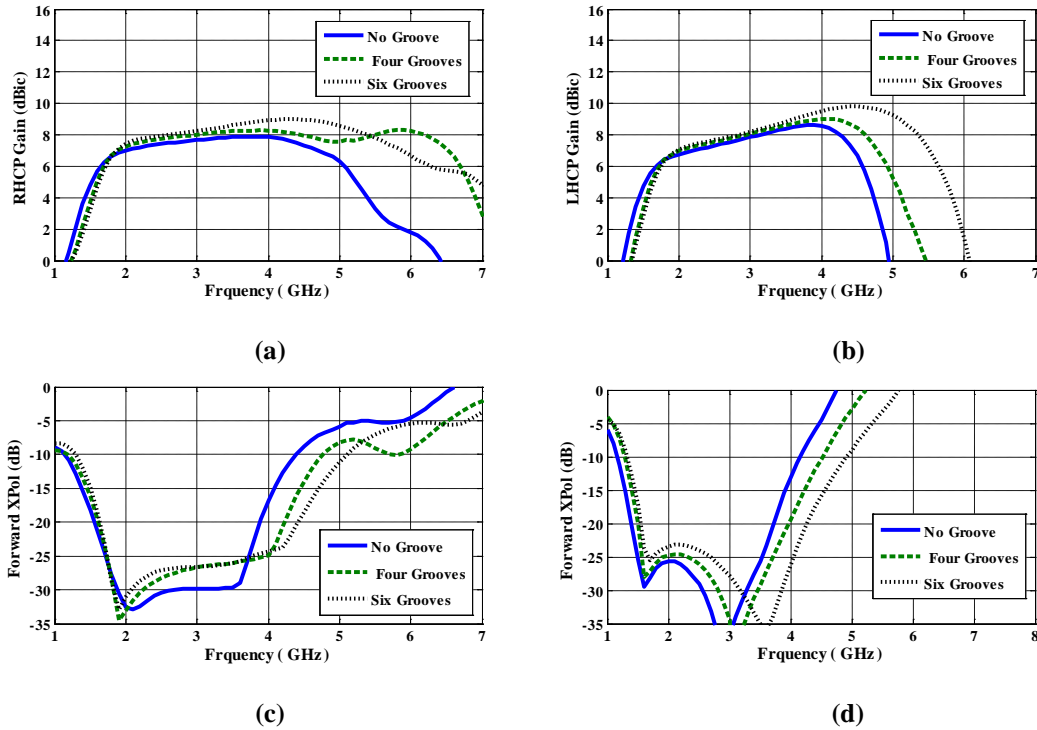
Fig. 6.16. (a) RHCP peak gain, (b) LHCP peak gain, (c) RHCP peak cross polarization, and (d) LHCP peak cross polarization of the antenna shown in Fig. 6.15 loaded with grooved substrate of ε_r=2.5, when n=1. The peak cross polarization is given at the ϕ=45° plane in the forward region over -90°<θ <+90°.

Table 6.3. Shared frequency bandwidths by both senses of polarization of the antenna shown in Fig. 6.15 loaded with grooved substrate of ε_r=2.5, when n=1.

# of grooves	Shared Frequency Bandwidths by both RHCP and LHCP
0 (full loading)	1.35–3.9GHz
4	1.45–4.2GHz
6	1.5–4.55GHz

The 3, 6, and 10dB beamwidths of the antenna in Fig. 6.15 with grooved dielectric of ε_r=2.5 are plotted in Fig. 6.17 for both RHCP and LHCP waves, when n=1. Over the respective shared frequency bandwidths of four- and six-groove cases, the RHCP and LHCP half-power and 6 dB beamwidths are nearly equal to each other, however the 10-dB beamwidths noticeably differs as the sense of polarization alters. This

134

is due to the different frequency responses of RHCP and LHCP gains as shown in Figs. 6.16a and 6.16b, respectively, wherein LHCP gain increases more rapidly with frequency than the RHCP gain. Thus, the corresponding RHCP and LHCP 10-dB beamwidth frequency responses are different.

(a)   (b)
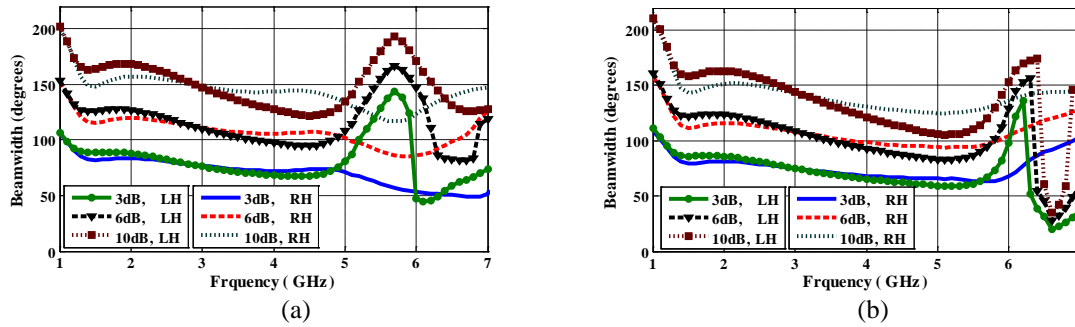
Fig. 6.17. 3-dB, 6-dB, and 10-dB RHCP-LHCP beamwidths of the antenna shown in (a) Fig. 6.15a and (b) Fig. 6.15b loaded with grooved substrate of ε_r=2.5, when n=1.

The boresight axial ratios of the antenna under study with four- and six-groove cases are shown in Fig. 6.18 for both senses of polarization. They are well below 3dB over 1-5.5GHz range. To illustrate the CP performance in whole space, the antenna radiation patterns with n=1 are plotted in Fig. 6.19 for both senses of polarization, when six groves are inserted into the substrate with ε_r=2.5 at the selected frequencies of 1.5GHz, near the low-end, 2.5GHz, 3.5GHz, and high-end 4.5GHz, exhibiting excellent CP patterns for both RHCP and LHCP cases.

(a)   (b)
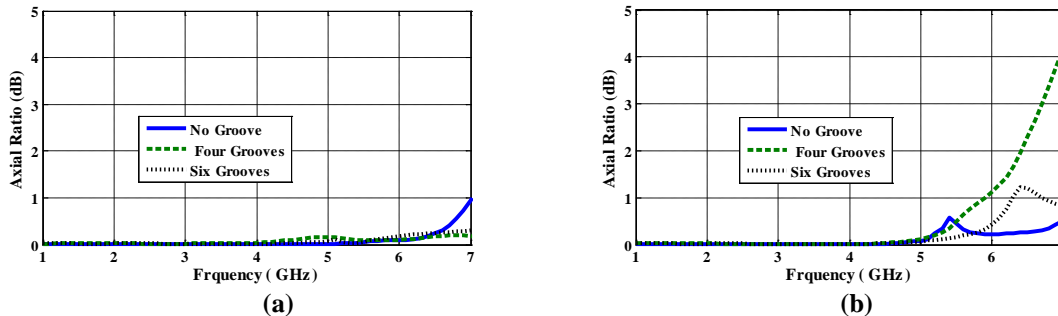
Fig. 6.18. (a) RHCP and (b) LHCP axial ratio at the θ=0° direction of the antenna shown in Fig. 6.15 loaded with grooved substrate of ε_r=2.5, when n=1.

135

f=1.5GHz	f=2.5GHz	f=3.5GHz	f=4.5GHz
RHCP	RHCP	RHCP	RHCP
LHCP	LHCP	LHCP	LHCP
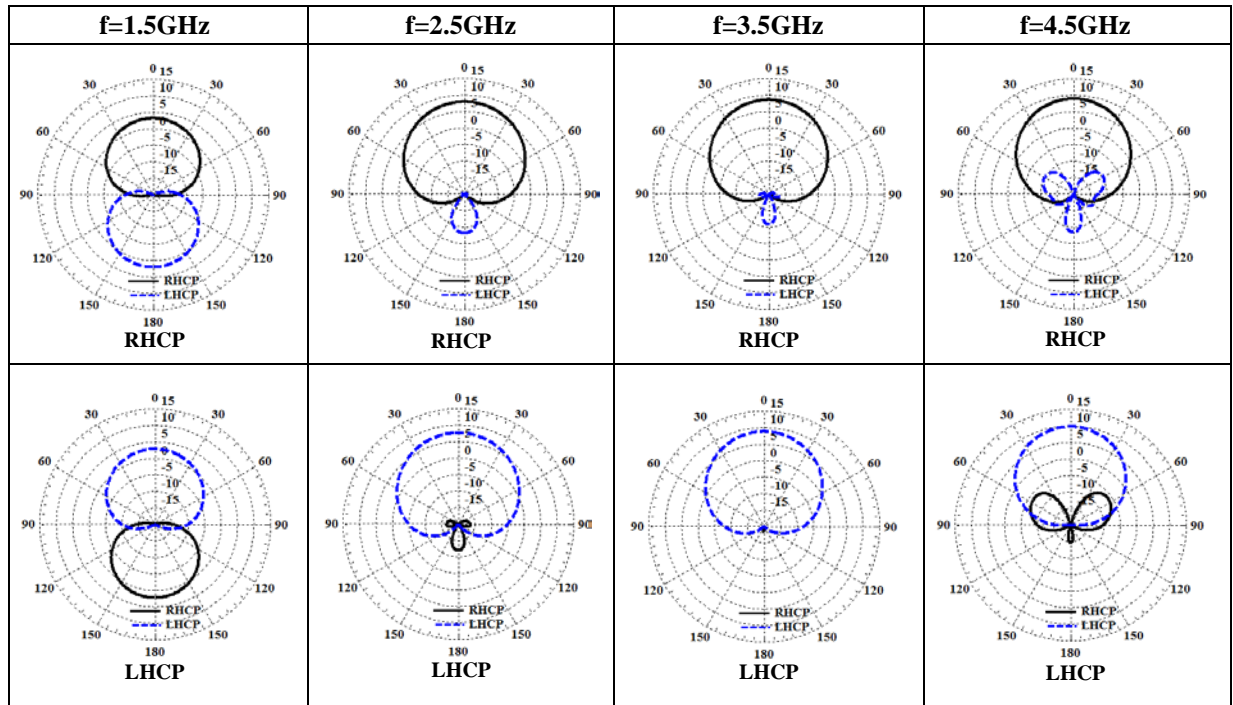
Fig. 6.19. RHCP and LHCP radiation patterns of the antenna shown in Fig. 6.15b loaded with six-groove substrate of ε_r=2.5, when *n*=1 at the frequencies of 1.5GHz, 2.5GHz, 3.5GHz, and 4.5GHz. Co- and cross-polarized components are given at the principal and diagonal planes, respectively.

6.5 Summary

In this chapter, dielectric loading impacts on the dual-polarized four-arm Archimedean spiral antenna with a ground plane radius of 37.5mm were numerically investigated, with a special interest to adjust the frequency bandwidths of the antennas for diverse polarization applications. Three loaded dielectric structures were studied including full, partial, and grooved substrates. For the fully loaded dielectric antennas, low contrast materials were used and shown how one can decrease the low-end frequency of the antenna without enlarging the antenna structure. Larger dielectric constants resulted in much reduced operating frequency at the price of a narrower bandwidth. Then, partially dielectric loaded antennas were also studied. This was inspired by confining the

creation of low-phase-velocity waves within the spiral arm region. The numerical results showed as dielectric radius decreased, the frequency bands widened with increased high frequency ends. As the frequency tuning capability of dielectric loaded antenna under study may require specific value of dielectric permittivity, grooved substrates were also investigated to address how such materials can be electrically realized using a conventional substrate with ε_r=2.5. Antenna parameters such as CP gain, cross polarization, beamwidths, radiation patterns, and corresponding frequency bandwidths of each cases were fully addressed for both senses of polarization.

It is concluded that frequency responses shared by both RHCP and LHCP waves can be adjusted using different dielectric loading structures without enlarging the physical size of the antenna aperture.

Chapter 7

Conclusions

7.1 Summary

In this thesis, directional radiation and polarization properties of compact four-arm Archimedean spiral antennas were investigated. First, spiral antennas were studied based on their Fourier modes, operating at the dominant and higher order modes in free space, exhibiting broadside and conical radiation properties, respectively. These beam scanning properties are highly beneficial in adaptive beam shaping and nulling applications in GPS and satellite communication systems. Low profile structures were realized using partially-filled absorber materials to make the antenna unidirectional in space. A small conducting disk was embedded inside the antenna's supporting structure to produce balanced spiral modes, without the need for expensive wideband baluns. The proposed low profile spiral antenna structure successfully supported the excitation of the higher order modes, which were experimentally validated in practice through three prototype antennas.

The next stage of the study involved investigating the polarization diversity capability of spiral antennas. The corresponding radiation mechanism and the required feeding excitation networks were mathematically described for a general case of an N-arm spiral antenna, using incident and reflected travelling waves. Broadside radiation patterns with dual-polarized operations in RHCP and LHCP were specifically addressed for a center-fed and low-profile four-arm Archimedean spiral antenna. It was found that

polarization diversity was realized when the spiral circumference was less than three wavelengths. Low-profile antenna structures backed by conducting ground planes were designed and investigated, to study different antenna parameters, such as CP gain, cross polarization, pattern symmetry, and axial ratios. Two ground plane sizes were studied. It was shown that both senses of circular polarization were produced, sharing a respectable frequency bandwidth, controlled by the supporting ground plane sizes. Prototype antennas were fabricated and tested. Excellent agreement between measured and computed results was observed. Furthermore, a simple equation to estimate the antenna peak gain was asymptotically specified in terms of the half-power beamwidths at the principal planes based on Kraus's equation [8].

Performance of the proposed spiral antennas, generating both senses of circular polarization with excellent radiation pattern symmetry, was also investigated as forward primary feeds to illuminate symmetrical-cut parabolic reflector antennas. Efficiencies as high as 77.8% were realized for circular-rim paraboloids, illuminated with these dual-polarized CP feeds. The resultant antennas contained excellent cross polarization discriminations that are well-suited for frequency reuse wireless applications in order to improve the channel capacity. In addition, rear radiation properties of low profile four-arm Archimedean spiral antennas were explored and their potential as backward feeds in reflector antennas was numerically investigated. The backward radiation was realized when the spiral circumference was in the order of 0.75λ, smaller than the one-wavelength active zone, normally required for the forward radiation of the first mode of the spiral. The reduced spiral aperture area created strong reflected waves in the presence of the ground plane; thus, the induced currents on the ground plane became the source of

radiation. As a result, the spiral antenna generated broadside CP backward radiation patterns, with an opposite sense of polarization to the spiral winding direction. This intriguing rear radiation was realized at the expense of the reduced frequency bandwidth. Nonetheless, an efficiency of about 65% was achieved. In general, backward feeds are attractive candidates in small front-fed reflectors, as they can be easily mounted through a single rod extending from the apex of the reflector. This results in significant blockage suppression without the need for extra mechanical struts, which usually leave considerable shadow on the reflector illumination aperture.

Finally, the compact dual-polarized four-arm Archimedean spiral antennas were further investigated, when they were loaded with dielectric materials, a well-known miniaturization technique in antenna engineering. The loaded structures were numerically investigated, with a special interest to adjust the frequency bandwidths of the antennas for diverse polarization applications. Three loaded dielectric structures were selected including full, partial, and grooved substrates. For the fully loaded dielectric antennas, low contrast materials were used and illustrated that the low-end frequency of the antenna decreased without enlarging the structure. Partially dielectric loaded antennas were also studied, which was inspired by confining the creation of low-phase-velocity waves within the spiral arm region. As the frequency tuning capability of the dielectric loaded antenna under study may require specific values of dielectric permittivity, grooved substrates were also investigated to address how such materials can be electrically realized using a conventional substrate with ε_r=2.5. Antenna parameters such as CP gain, cross polarization, beamwidths, radiation patterns, and corresponding frequency bandwidths were analyzed for both senses of polarization. It was concluded that dielectric

140

loading provided a means to tune frequency responses shared by both RHCP and LHCP waves, without enlarging the physical size of the antenna aperture.

7.2 Future Work

While multi-mode and multi-functional antennas with reconfigurable polarization capabilities have been investigated using low profile and compact four-arm Archimedean spiral antennas and their applications in reflector antennas have been studied, there are some important areas, which need further investigation, research, and development. They are listed as follows:

> Investigate impedance bandwidths of the proposed spiral antennas in backward operations.

> Study meandered spiral antennas with polarization diversity capabilities for small antenna applications.

> Develop techniques to further widen the frequency bandwidth of dual-polarized spiral antennas.

> Improve the frequency response of the rear-radiating backward spiral antennas.

> Extend the polarization diversity properties into higher order modes with boresight-null radiation patterns.

> Study multi-arm spiral antennas for adaptive beam shaping and nulling applications.

- ➢ Design integrated wideband matching networks for multi-arm spiral antennas.

- ➢ Investigate laminated spiral arm structures in order to improve the antenna gain, radiation efficiency, and radiation resistance. Typical geometry of a two-layer Archimedean spiral antenna is shown in Fig. 7.1.
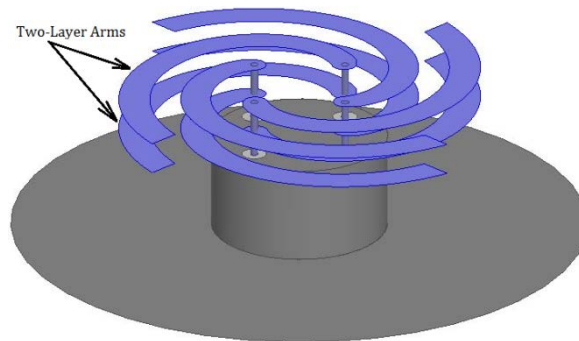
Fig. 7.1. Typical geometry of a laminated four-arm Archimedean spiral antenna; the spiral has four arms.

An initial study of the above structure has shown that the CP gain and impedance matching can be improved by adjusting the spacing between the layers. Antennas with multi-layer structures bring additional degrees of freedom to achieve optimum performance.

Appendix A

Governing Equations in Self-Complementary Four-Arm Archimedean Spirals

Herein, the relationship between the spiral constant and the metallization width is given for a self-complementary four-arm Archimedean spiral antenna to clarify Eq. 4.12 in chapter 4. Geometry of a self-complementary four-arm Archimedean spiral antenna is illustrated in Fig. A1; where w and s are the metallization width and the spacing between the arms, respectively.
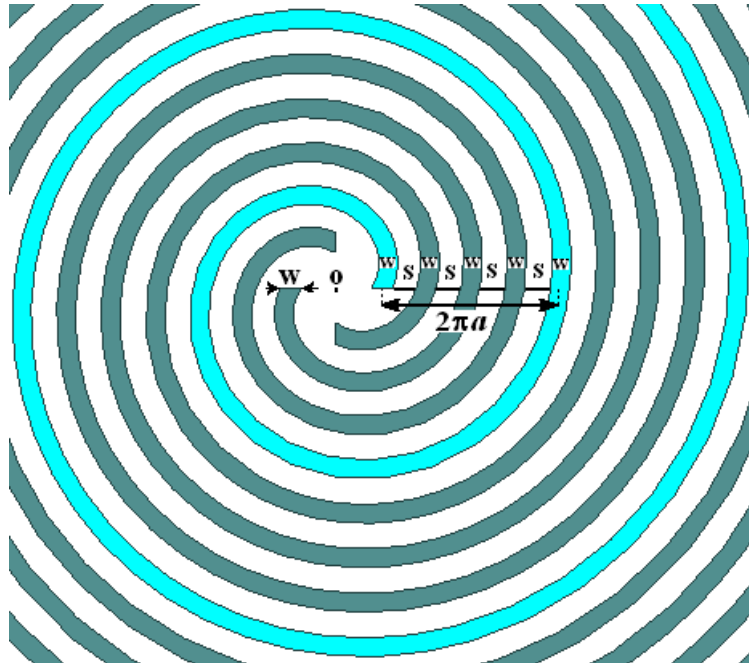
Fig. A1. Geometry of a self-complementary four-arm Archimedean spiral antenna.

Mathematically, the radius of the Archimedean spiral is governed by the following equation,

$$r = a\ \phi + r_o \qquad\qquad (A.1)$$

where a is the spiral constant and r_o is the start radius. From Eq. A1, it is clear that the spiral radius change, after a 2π rotation, is equal to $2\pi a$. As illustrated in Fig. A1, four spiral arms are fit within this radius change. Therefore,

$$4s + 4w = 2\pi a \qquad\qquad (A.2)$$

For a self-complementary structure, s is equal to w. Thus,

$$8w = 2\pi a \quad \Rightarrow \quad a = \frac{4w}{\pi} \qquad\qquad (A.3)$$

Therefore, the spiral constant is dictated by the metallization width for the self-complementary four-arm spiral antenna shown in Fig. A1.

References

[1]   U. R. Kraft, "Polarization properties of spiral antennas: A tutorial," *Electromagnetics*, vol. 14, pp. 259-284, 1994.

[2]   R. G. Corzine and J. A. Mosko, *Four-Arm Spiral Antennas*, Artech House: Norwood, MA, 1990.

[3]   W. Curtis, "Spiral antennas," *IRE Trans. Antennas Propag.,* vol. AP-8, pp. 293–306, May 1960.

[4]   L. Kaiser," The Archimedean two-wire spiral antenna," *IRE Trans. Antennas Propag.,* vol. 8, no. 3, pp. 312–323, May 1960.

[5]   V. Rumsey, "Frequency independent antennas," *IRE International Convention Record*, vol. 5, Part 1, pp. 114–118, Mar. 1957.

[6]   C. Balanis, *Antenna Theory: Analysis and Design*, 3rd ed., Wiley, New York, 2005.

[7]   Y. Mushiake, "The input impedances of slit antennas," *IEE of Japan*, vol. 69-3, pp. 87–88, 1949.

[8]   J. D. Kraus, *Antennas,* New York, McGraw-Hill Book Company, 1988.

[9]   W. L. Stutzman, G. A. Thiele, *Antenna Theory and Design*, Wiley, Hoboken, NJ, 1998.

[10]   A. C. Ludwig, "Near-field far-field transformation using spherical-wave expansion," *IEEE Trans. Antennas Propag.,* vol. 19, pp. 214–220, 1971.

[11]   H. Nakano, *Helical and Spiral Antennas: A Numerical Approach*, Research Studies Press, Wiley, Letch worth, England, 1987.

[12]   G. A. Deschamps and J. D. Dyson, "The logarithmic spiral in a single aperture multimode antenna system," *IEEE Trans. Antennas Propag.*, vol. 19, no. 1, pp. 90–96, Nov. 1971.

[13]   L. Shafai, "Design of multi-arm multi-mode spiral antennas for directional beams using equivalent array concept," *Electromagnetics*, vol. 14, pp. 285–304, 1994.

[14]   A. M. Mehrabani and L. Shafai, "Tri-band/Wideband Antenna as Radiating Element for GPS Receivers," Defence Research and Development Canada [DRDC] Rep., Ottawa, Canada, pp. 1–107, November 2010.

[15]   R. T. Gloutak and N. G. Alexopoulos, "Two-arm eccentric spiral antenna," *IEEE Trans. Antennas Propag*., vol. 45, pp. 723–730, 1997.

[16]   H. Nakano, Y. Shinma, and J. Yamauchi, "A monofilar spiral antenna and its array above a ground plane-formation of a circularly polarized tilted fan beam," *IEEE Trans. Antennas Propag*., vol. 45, pp. 1506–1511, 1997.

[17]   S. K. Khamas and G. G. Cook, "Moment-method analysis of printed wire spirals using curved piecewise sinusoidal subdomain basis and testing functions," *IEEE Trans. Antennas Propag*., vol. 45, pp. 1016–1022, 1997.

[18]   A. Shlivinski, E. Heyman, and R. Kastner, "Antenna characterization in the time domain," *IEEE Trans. Antennas Propag.* vol. 45, pp. 1140–1149, 1997.

[19]   H. Nakano, J. Eto, Y. Okabe, and J. Yamauchi, "Tilted-and axial-beam formation by a singlearm rectangular spiral antenna with compact dielectric substrate and conducting plane," *IEEE Trans. Antennas Propag.* vol.50, pp. 17–23, 2002.

[20]   H. Nakano, H. Y. Yasui, and J. Yamauchi, "Numerical analysis of two-arm spiral antennas printed on a finite-size dielectric," *IEEE Trans. Antennas Propag*., vol. 50, pp. 362–370, 2002.

[21]   A. Jovanović and S. Jovićević," Field analysis of the Archimedean spiral antenna," *Electromagnetics*, vol. 31, pp. 147–158, 2011.

[22]   R. F. Harrington, *Time-Harmonic Electromagnetic Fields.* New York: McGraw-Hill, 1961.

[23]   G. J. Burke and A. J. Poggio, Numerical Electromagnetics Code, NEC2.

[24]   EM Software & Systems (USA) Inc, FEKO, Hampton, VA.

[25]   High Frequency Structure Simulator (HFSS 15.0). Canonsburg, PA Boston, MA: ANSYS.

[26]   C.A. Balanis, *Advanced Engineering Electromagnetics*. John Wiley & Sons, 1989.

[27]   H. Nakano, K. Nogami, S. Arai, H. Mimaki, J. Yamauchi, "A spiral antenna backed by a conducting plane reflector," *IEEE Trans. Antennas Propag*., vol. 34, pp. 791–796, Jun. 1986.

[28]   J.J.H Wang and V.K. Tripp, "Design of multioctave spiral-mode microstrip antennas,"*IEEE Trans. Antennas Propag.,* vol. AP-39, pp.332–335, Mar.1991.

[29] H. Nakano, K. Hitosugi, N. Tatsuzawa, D. Togashi, H. Mimaki, and J. Yamauchi, "Effects on the radiation characteristics of using a corrugated reflector with a helical antenna and an electromagnetic band-gap reflector with a spiral antenna," *IEEE Trans. Antennas Propag.*, vol. 53, Part1, pp.191–199, Jan. 2005.

[30] J. L. Volakis, C. Chen, and K. Fujimoto, *Small Antennas Miniaturization Techniques and Applications*. New York: McGraw-Hill, 2010.

[31] S. A. Schelkunoff, "Theory of antennas of arbitrary size and shape," *Proc. of the IRE*, vol. 29, no. 9, pp. 493–521, 1941.

[32] W. F. Patterson and E. T. Roland, "Spiral Antenna with Zigzag Arms to Reduce Size," U.S. Patent 3 454 951, July 1969.

[33] A. M. Mehrabani, and L. Shafai, "A physical interpretation of effective dielectric properties of slow-wave transmission lines in small antenna applications," *IEEE APS/URSI*, Orlando, FL, USA, July 7–13, 2013.

[34] D. M. Pozar, *Microwave Engineering. 3rd Edition.* New Jersey: John Wiley & Sons, 2005.

[35] B. A. Kramer, C. Chen, and J. L. Volakis, "Size reduction of a low-profile spiral antenna using inductive and dielectric loading," *IEEE Antennas Wireless Propag. Lett.*, vol. 7, pp. 22–25, 2008.

[36] I. Tzanidis, C. Chen, and J. Volakis, "Low profile spiral on a thin ferrite ground plane for 220-500 MHz operation," *IEEE Trans. Antennas Propag.,* vol. 58, no. 11, pp. 3715–3720, Nov. 2010.

[37] H. Nakano, S. Sasaki, H. Oyanagi, and J. Yamauchi, "Cavity-backed Archimedean spiral antenna with strip absorber," *IET Microw. Antennas Propag.*, vol. 2, no. 7, pp. 725–730, 2008.

[38] H. Nakano,R. Satake, and J. Yamauchi," Extremely low-profile, single-arm, wideband spiral antenna radiating a circularly polarized wave," *IEEE Trans.Antennas Propag.*, vol. 58, no. 5, pp. 1511–1520, May 2010.

[39] H. Nakano, H. Soga, T. Honma, and J. Yamauchi, "Effects of adding a small disk to a spiral antenna backed by a conducting plane reflector," *IEE Proceedings-H*, vol. 138, no. 4, pp. 375–377, August 1991.

[40] L. Shafai, "Directional Switched Beam Antenna," U.S. Patent, Patent Number: 5 220 340, June 15, 1993.

[41] A. M. Mehrabani, and L. Shafai, "A compact curl antenna with a cavity-backed absorber," *IEEE APS/URSI*, Chicago, IL, USA, July 8–14, 2012.

[42] A. M. Mehrabani, and L. Shafai, "Cavity backed circularly polarized spiral antennas," *ANTEM*, Victoria, BC, Canada, July 13–17, 2014.

[43] A. M. Mehrabani, and L. Shafai, "Parametric study of cavity backed spiral antennas," *ANTEM*, Victoria, BC, Canada, July 13–17, 2014.

[44] S. G. Komlos, P. Foldes, and K. Jasinski, "Feed system for clockwise and counterclockwise circular polarization," *IRE Trans. Antennas Propag.*, vol. 9, no.6, pp. 577–578, Nov. 1961.

[45] H. P. Coleman and B. D. Wright, "An orthogonal mode (dual-sense) helical antenna," *IEEE Trans. Antennas Propag.*, vol. 32, no. 4, pp.414–415, Apr. 1984.

[46] K. Hirose, K. Kawai, and H. Nakano, "An array antenna composed of outer-fed curl elements," *IEEE APS/URSI*, vol. 2, pp. 1162 -1165, Jun. 1998.

[47] C. W. Jung, A. B. A. Cetiner, and F. D. Flaviis, "A single-arm circular spiral antenna with inner/outer feed circuitry for changing polarization and beam characteristics," *IEEE APS/URSI*, vol. 4, pp. 474-477, 2003.

[48] P. L. Ransom, "An Experimental Investigation of the Four-Arm Planar Logarithmic Spiral Antenna," Univ. Illinois, Tech. Rep. May 1965.

[49] O. K. Kim, "An Experimental Investigation of the Conical Four-Arm Logarithmic Spiral Antenna with Large Cone Angle," Univ. Illinois, Tech. Rep. Sept. 1966.

[50] O. Kim and J. Dyson, "A log-spiral antenna with selectable polarization," *IEEE Trans. Antennas Propag.,* vol. 19, no. 5, pp. 675–677, Sept. 1971.

[51] S. Chung and S. Kuo, "Multiple Polarization Spiral Antenna," U.S. Patent 3 562 756, Feb. 9, 1971.

[52] A. M. Mehrabani, and L. Shafai, "Planar, self-complementary, and wideband antennas with polarization diversity," *IEEE APS/URSI*, Memphis, TN, USA, July 6–11, 2014.

[53] A. M. Mehrabani, and L. Shafai, "Performance of center-fed compact Archimedean spiral antennas generating orthogonal circular polarizations with unidirectional patterns," submitted to *IEEE Trans. Antennas Propag.*, May 2014.

[54] S. Silver, *Microwave Antenna Theory and Design*. Peter Perrgrinus, London, UK, 1984, Institution of Electrical Engineers Electromagnetic Waves Series 19.

[55] A. Calvin, "A New Antenna Having equal E- and H-plane patterns," *IRE Trans. Antennas Propag.*, vol. 2, 1954, pp. 113-119.

[56] G. L. James, and D. P. S. Malik, "Towards the theoretical design of splash-plate feeds," *Electronics Lett.*, vol. 11, no. 24, 1975, pp. 593–594.

[57] P. Newham, "A high efficiency splash plate feed for small reflector antennas," *4th Int. Conference on Antennas and Propagation*, Coventry, UK, Apr. 16-19, 1985, pp. 420–423.

[58] G. T. Poulton and T. S. Bird, "Improved rear-radiating waveguide cup feeds," *IEEE APS/URSI*, vol. 1, 1986, pp.79–82.

[59] T. S. Bird, "TE_{11} mode excitation of flanged circular coaxial waveguides with an extended center conductor," *IEEE Trans. Antennas Propag.*, vol. 35, no. 12, 1987, pp. 1358–1366.

[60] P.-S. Kildal, "The Hat Feed: A dual-mode rear-radiating waveguide antenna having low cross polarization," *IEEE Trans. Antennas and Propag.*, vol. 35, no.9, 1987, pp. 1010–1016.

[61] P.-S. Kildal and S. A. Skyttemyr, "Dipole-disk antenna with beam-forming ring," *IEEE Trans. Antennas Propag.*, vol. 30, no. 4, pp. 529–534, 1982.

[62] M. Qudrat-E-Maula and L. Shafai, "Low-cost, microstrip-fed printed dipole for prime focus reflector feed," *IEEE Trans. Antennas Propag.,* vol. 60, no. 11, pp. 5428–5433, Nov. 2012.

[63] M. Qudrat-E-Maula, L. Shafai, and Z. A. Pour, "A corrugated printed dipole antenna with equal beamwidths," *IEEE Trans. Antennas Propag.,* vol. 62, no. 3, pp. 1469–1474, March 2014.

[64] L. Shafai and P. Bhartia, "High Performance Dipole Feed for Reflector Antennas," United States Patent, Patent number: 4 982 198, January 1, 1991.

[65] W. T. Patton, *The Backfire Bifiiar Helical Antenna*. Ph.D. dissertation, Univ. Illinois, 1963.

[66] C. C. Kilgus, "Shaped-conical radiation pattern performance of the backfire quadrifilar helix," *IEEE Trans. Antennas Propag.,* vol. 23, no. 3, pp. 392-394, May 1975.

[67] R. C. Johnson and R. B. Cotton, "A backfire helical feed," *IEEE Trans. Antennas Propag.,* vol. 32, no. 10, pp. 1126-1128, Oct. 1984.

[68] H. Nakano, J. Yamauchi, and H. Mimaki, "Backfire radiation from a monofilar helix with a small ground plane," *IEEE Trans. Antennas Propag.,* vol. 36, no. 10, pp. 1359-1364, Oct. 1988.

[69]   H. Nakano, S. Iio, and J. Yamauchi, "Improvement in front-to-back ratio of a bifilar backfire helix by a flared open end," *IEEE Trans. Antennas Propag.,* vol. 41, no. 11, pp. 1591-1595, Nov. 1993.

[70]   A. M. Mehrabani and L. Shafai, and M. Clénet, "Investigation of higher order mode radiation performance of four-arm spiral antennas," *IEEE APS/URSI*, Spokane, WA, USA, July 3–8, 2011.

[71]   Rogers' RT/duroid® 5880LZ High Frequency Laminates, Advanced Circuit Materials Division, High Frequency Products, Rogers, CT, USA.

[72]   L. Shafai, S. K. Sharma, and S. Rao, *Handbook of Reflector Antennas and Feed Systems*. Ch. 1, vol. II, Artech House: MA, 2013.

[73]   P. S. Kildal, "Factorization of the feed efficiency of paraboloids and Cassegrain antennas," *IEEE Trans. Antennas Propag.*, vol. 33, no. 8, pp. 903–908, 1985.

[74]   T. A. Milligan, *Modern Antenna Design*. 2nd Edition, John Wiley & Sons: Hoboken: NJ, 2005.

[75]   J. R. James, P. S. Hall, and C. Wood, *Microstrip Antenna Theory and Design*. Peter Peregrinus, London, UK, 1981.

[76]   N. Gupta, R. Chaitanya Babu, and L. Shafai, "Characteristics of microstrip transmission line on grooved dielectric substrate," *Microwave and Optical Technology Lett.*, vol. 17, no. 1, pp. 55–57, January 1998.